universität
innsbruck

MASTER THESIS

Towards the Creation of Vortices in a Dipolar Bose-Einstein Condensate

Sandra Brandstetter, BSc

supervised by
Prof. Dr. Francesca Ferlaino
Dr. Manfred Mark

*Thesis submitted in fulfillment of the requirements
for the degree of Master of Science in Physics*

at the

University of Innsbruck,
Faculty of Mathematics, Computer Science and Physics,
Institute for Experimental Physics

Innsbruck, January 2020

'What're quantum mechanics?'
'I don't know. People who repair quantums, I suppose.'

- Sir Terry Pratchett, *Eric*

Abstract

In this thesis, I describe and characterize a setup for the production of vortices in a Bose-Einstein Condensate with dipolar interactions. The formation of vortices as a response to rotation is one of the key features of a superfluid, which has been observed in contact interacting Bose-Einstein condensates and Fermi gases. The long-range, anisotropic dipole-dipole interaction present in Bose-Einstein condensates of dipolar atoms is expected to alter the properties of the vortices as well as the interaction between them. Although many theoretical predictions on vortices in dipolar quantum gases exist, they have not yet been observed experimentally. The aim of this thesis is to built and design a setup for the creation of vortices in a dipolar condensate of Erbium and/ or Dysprosium atoms.

The first part of the setup consists of a one-dimensional lattice with variable spacing and confinement, a so-called accordion lattice. It is formed by the interference of two laser beams in the focal point of an aspherical lens. The confinement in this lattice can be altered by changing the angle of interference, allowing us to trap the atoms in a configuration with weak confinement and high lattice spacing. As the initial lattice spacing is larger than the spatial extent of the condensate, we can trap all atoms within a single node of the lattice. By increasing the separation of the beams, the vertical confinement can be increased, while the confinement in the horizontal plane remains weak, leading to the desired trap geometry for the creation of vortices. To find the appropriate parameters, we programmed a numerical simulation of the accordion lattice. Based on the results of these computations, the experimental setup for the accordion lattice was planned and set up. We characterize the stability as well as the compression of the accordion lattice.

The second part of the experimental setup consists of a blue detuned variable trap, which is achieved by modulating the intensity distribution of a laser beam with a wavelength of $\lambda = 370\,\mathrm{nm}$ using a Digital micromirror device (DMD). This wavelength is blue detuned for both Erbium and Dysprosium. We design an optical setup to image the pattern displayed on the DMD onto the atomic plane.

Zusammenfassung

Diese Arbeit beschreibt einen Aufbau zur Erzeugung von Wirbeln in einem Bose-Einstein-Kondensat mit dipolaren Wechselwirkungen. Die Bildung von Wirbeln als Reaktion auf Rotation ist eines der Schlüsselmerkmale einer Supraflüssigkeit, welches sowohl in Bose-Einstein-Kondensaten als auch in Fermigasen mit Kontaktwechselwirkung beobachtet wurde. Es wird erwartet, dass die anisotrope, langreichweitige Dipol-Dipol-Wechselwirkung die Eigenschaften der Wirbel sowie die Wechselwirkung zwischen ihnen verändert. Obwohl viele theoretische Vorhersagen über Wirbel in dipolaren Quantengasen existieren, wurden sie noch nicht experimentell beobachtet. Ziel dieser Arbeit ist es, einen Aufbau für die Erzeugung von Wirbeln in einem dipolaren Kondensat aus Erbium- und/ oder Dysprosium Atomen zu entwickeln.

Der erste Teil des Aufbaus besteht aus einem eindimensionalen Gitteraufbau mit variablem Gitterabstand und -einschluss, dem sogenannten Akkordeongitter. Dies wird durch die Interferenz zweier parallel verlaufender Strahlen im Fokuspunkt einer asphärischen Linse erreicht. Die Fallenfrequenzen sind abhängig vom Winkel und können daher durch eine Veränderung des Abstands der beiden Strahlen variiert werden. Zu Beginn werden die Atome in einem Gitter mit niedrigen Fallenfrequenzen und hohem Gitterabstand gefangen, so dass sie nur eine einzige Gitterebene einnehmen. Durch Erhöhen des Strahlabstands in vertikaler Richtung können wir die Fallenfrequenzen in dieser Richtung erhöhen, während sie in der horizontalen Ebene schwach bleiben. Um die gewünschten Parameter festzulegen programmieren wir eine numerische Simulation des Interferenzmusters. Basierend auf den Ergebnissen der Berechnungen haben wir den Versuchsaufbau für das Akkordeongitter erstellt. Wir charakterisieren die Stabilität sowie die Kompression des Akkordeongitters.

Der zweite Teil des Versuchsaufbaus besteht aus einer blau verstimmten variablen Falle. Das variable Potential wird erreicht durch die Projektion des Musters auf einem Mikrospiegelaktor auf die atomare Ebene erreicht. Der Mikrospiegelaktor moduliert die Intensitätsverteilung eines Laserstrahls mit $\lambda = 370\,\text{nm}$, eine Wellenlänge die sowohl für Erbium als auch für Dysprosium blau verstimmt ist. Wir entwerfen einen optischen Aufbau zur Projektion dieses Intensitätsmuster auf die Atome.

Contents

Eidesstattliche Erklärung

Ich erkläre hiermit an Eides statt durch meine eigenhändige Unterschrift, dass ich die vorliegende Arbeit selbständig verfasst und keine anderen als die angegebenen Quellen und Hilfsmittel verwendet habe. Alle Stellen, die wörtlich oder inhaltlich den angegebenen Quellen entnommen wurden, sind als solche kenntlich gemacht.

Die vorliegende Arbeit wurde bisher in gleicher oder ähnlicher Form noch nicht als Magister-/Master-/Diplomarbeit/Dissertation eingereicht.

Innsbruck, 31. Januar 2020, _____
Sandra Brandstetter, BSc

Acknowledgements

First of all I want to thank Francesca for giving me the opportunity to work in the RARE team. Further, I want to thank her for encouraging me to excel and for supporting me in making the decisions about my scientific future. Moreover I am happy that I could participate in a PhD meeting as a fresh master student, allowing me to gain deeper insights into the field of Dipolar Quantum gases.

I am grateful that Manfred gave me the opportunity to work on his ESQ discovery project. Thanks for letting me work independently but always having my back and nudging me when I needed it. I enjoyed our discussions about science, optics, electronics and programming. Moreover I want to thank you for initially sparking my interest in the field of ultracold quantum gases during the work on my bachelor's thesis.

Thanks to all of the members of the ERBIUM, the RARE as well as the T-REQS team, for helping me whenever I had questions, and for the physics and non-physics related discussions during lunch time and coffee breaks. I really enjoyed being a part of the team. Special thanks goes to Philipp for teaching me many of the experimental techniques (e.g. coupling a fiber efficiently), helping me to get the Msquared laser working again and answering all of my questions concerning SolidWorks! I also want to thank the people in the other ultracold groups for creating such a pleasant working environment and the exchange of knowledge!

None of our work would be possible without the people working in administration as well as in the mechanical workshop. Special thanks goes to our administrative assistant Silvia for taking care of all of my orders and to Bernhard from the mechanical workshop of the IQOQI. Thank you for your fast, precise work, for your help with my designs and for the introduction to turning and milling.

I also want to thank the people who survived the Bachelor together with me. Thanks to Sebi, Flo, Kathi, Medi, Steve, Raphi, Josh et al. for study sessions in the Victor Franz Hess house, coffee breaks, legendary lectures (sometimes even including a Frisbee), wonderful trips to CERN and Kasan, an occasional beer (or two) in the 9b, the Wohnzimmer or elsewhere, skiing sessions, game nights, Glühwein, watching the Tagebuchslam in Treibhaus, ... You really helped to make these years in Innsbruck to some of the most amazing years so far.

Thanks to my friends outside of University, especially those in scouting, for distracting me from physics whenever I needed it. Thanks especially to Oliver, Katha, Elli, Ingrid and Hanna among many others. Thanks also to the guys from the 'Physikalische Übungen' for discovering physics and nerding out together back in High school.

I also want to thank my high school teachers Mag. Jutta Wirth and Prof. Helmut

1. Introduction

1.1. Motivation

In 1924 Satyendra Nath Bose developed a derivation of Plancks quantum radiation law that was, contrary to earlier derivations, not based on classical electrodynamics but instead on statistical quantum mechanics [1]. Einstein extended this theory to matter, leading him to the prediction of a novel state of matter, the so called Bose-Einstein Condensate (BEC). This state manifests itself in a macroscopic occupation of one state, which can be described by a single wave function. Thus the BEC behaves as a macroscopic quantum object, which facilitates the exploration of quantum phenomena.

The first experimental observation of a BEC followed in 1995, more than 70 years after the initial theoretical prediction. This delay can be explained by the fact that the experimental realization of BECs is directly linked to the development of the laser, a key ingredient for cooling and trapping of neutral atoms. The first BEC was produced by the group of Carl Wieman and Eric Cornell at the NIST-JILA lab in a vapour of ^{87}Rb atoms [2], followed shortly after by the group of Wolfgang Ketterle with a BEC in a vapour of Na atoms [3].

Different atomic species followed after the initial discovery. Bose-Einstein condensation has been achieved with 13 different atomic species, molecules [4] and photons [5].

- **Alkali metals:** Li [6], Na [3], K [7], Rb [2] and Cs [8]

- **Alkaline Earth metals:** Ca [9] and Sr [10]

- **Lanthanides:** Dy [11], Er [12] and Yb [13]

- **Transition metals:** Cr [14]

- **Nobel gases:** Metastable He [15]

- **Others:** H [16]

Owing to their different properties, the various atomic species can be used to explore different physical phenomena. A special property of Chromium as well as the two condensed lanthanide atoms, Erbium and Dysprosium, is their large intrinsic magnetic dipole moment. While the interaction of atoms is normally governed by the contact interaction, these atoms exhibit an additional interaction - the dipole-dipole

interaction (DDI). The DDI is long range and anisotropic, thus enabling the study of a whole new class of physical phenomena. Other systems exhibiting large dipole moments are hetero-nuclear molecules [17] and Rydberg atoms [18].

The phenomenon of Bose-Einstein condensation is closely linked to superfluidity, a phenomenon first observed in liquid helium in January 1938 by Pyotr Kapitza [19], and John F. Allen and Don Misener [20]. They studied the flow of liquid Helium II through long capillaries. These measurements gave an upper limit to the viscosity of liquid Helium II that is 4 orders of magnitude smaller than the viscosity of Hydrogen gas. This observation let Pyotr Kapitza to the intuition that '(...), by analogy with superconductors, that the helium below the λ-point enters a special state which might be called a *superfluid*' [19]. As interacting BECs are superfluid, they provide an ideal test bed for the phenomenon of superfluidity due to the tunability of key parameters such as the density and the interaction of particles. This tunability is hardly possible with superfluid He.

One of the distinguishing features of a superfluid is its response to rotation. As the velocity of a superfluid is proportional to the gradient of the phase, the fluid is irrotational, signifying that it can not rotate as a normal fluid. Instead the superfluid forms vortices as a response to rotation. These vortices differ from vortices appearing in classical systems such as drained bathtubs and at the wing-tips of aeroplanes, due to the irrotationality of the superfluid and the fact that it does not rotate as a rigid body. In addition to this, the angular momentum of vortices in a superfluid is quantized. The occurrence of vortices in a quantum system is thus a hallmark for superfluidity. Vortices have been observed in both BECs [21] and strongly interacting Fermi gases [22] as well as superfluid He. The study of vortices can lead to a deeper understanding of the properties of novel states of matter and phase transitions between them (e.g. the Berezinskii–Kosterlitz–Thouless transition [23])

Up to now, the study of vortices has been limited to contact-interacting BECs. The dipole-dipole interaction is expected to add new effects to both the formation and properties of single vortices as well as the interaction of multiple vortices. The RARE experiment is the first mixture experiment combining two highly magnetic atomic species, Erbium and Dysprosium [24]. It allows both single and dual species operation with multiple isotopes. The aim of this thesis is to design and test the components necessary for the creation of vortices in a dipolar quantum gas of Er and/or Dy atoms.

1.2. Thesis Overview

This thesis describes an experimental setup designed for the production of vortices in a Bose-Einstein Condensate of Erbium and Dysprosium atoms. It is structured as follows:

Chapter 2 introduces the physics of quantum gases with contact and dipole-dipole interactions and the concept of optical dipole traps. First, it gives an overview of the interactions in quantum gases, discussing both the contact and the dipole-dipole

interaction. Moreover we discuss the Gross-Pitaevskii equation for both cases, which can be used to calculate the wave function describing the Bose-Einstein condensate. The Section on optical dipole traps describes the general concept of such traps as well as the polarizability of both Erbium and Dysprosium.

Chapter 3 discusses the physics of vortices in Bose-Einstein condensates with both contact and dipole-dipole interactions. It starts with the superfluid properties of Bose-Einstein condensates and then goes on to discuss the properties of quantized vortices as well as their interactions.

Chapter 4 describes the accordion lattice setup. It is divided into different Sections describing the prerequisites, the calculations performed for design considerations, as well as the experimental implementation and its characteristics.

Chapter 5 describes the variable blue detuned potential which will be used to create vortices in the Bose-Einstein condensate. We discuss the digital micromirror device used in our experimental scheme and the optical set-up which we designed to project the pattern displayed on the DMD onto the atoms.

Finally I conclude this thesis with an outlook in Chapter 6.

2. Dipolar Quantum Gases

2.1. Interactions in quantum gases

2.1.1. Contact interactions

Usually, atoms interact via the van der Waals (vdW) force, resulting in a potential

$$U_{\mathrm{vdW}} = -\frac{C_6}{r^6},$$

(2.1)

where C_6 is the vdW coefficient and r is the inter-particle distance. For low temperatures (i.e. low collision energies) the scattering of two particles is dominated by s-wave scattering. In this limit, the scattering problem can be fully described by the scattering length a, which is determined by the phase shift δ_0 between the incoming and the scattered wave

$$\delta_0 = ka,$$

(2.2)

where k is the wave number of the incoming wave. The scattering length can be dependent on the magnetic field, in cases when the scattering potentials can be tuned via the Zeeman effect. This is due to the different magnetic moments of bound molecular states and the scattering atomic state, allowing a tunability of the resulting scattering length via an external magnetic field. Feshbach resonances occur when the atomic scattering state couples to a bound molecular state. The dependence of the scattering length a on the external magnetic field B can typically be written as

$$a(B) = a_{\mathrm{Bg}} \left(1 - \frac{\Delta}{B - B_0} \right),$$

(2.3)

where a_{Bg} is the background scattering length, B_0 is the position of the Feshbach resonance and Δ is the width of the resonance [25].

In the case of low energy scattering, the contact interaction potential can be written as

$$U_{\mathrm{mf}}(\mathbf{r}) = \frac{4\pi\hbar^2 a}{m}\delta(\mathbf{r}) = g\delta(\mathbf{r}),$$

(2.4)

where m is the mass of the atoms and g is the coupling constant characterizing the interaction. The short-range nature of this interaction becomes apparent considering the dependence of the interaction potential on the Dirac delta function. This interaction is thus referred to as contact interaction.

2.1.2. Dipole-Dipole interactions

Atoms also have a permanent magnetic dipole moment, the strength of which is dependent on their internal structure and quantum numbers. The projection of the magnetic moment of an atom along the quantization axis is given by

$$\mu = m_J g_J \mu_B, \tag{2.5}$$

where m_J is the magnetic quantum number for the total angular momentum of the electron, giving the projection of the total angular momentum J on the quantization axis (i.e. the magnetic field direction) and g_J is the Landé g-factor for the total electronic angular momentum. In the case of LS coupling, it can be written as

$$g_J = 1 + (g_S - 1)\frac{J(J+1) + S(S+1) - L(L+1)}{2J(J+1)}, \tag{2.6}$$

where $g_S \approx 2.002$ is the Landé g-factor of the electron and $S = 1$ and L denote spin and angular momentum quantum number, respectively. For lanthanide atoms, several corrections of this term have to be taken into account, which stem from the deviation from perfect LS-coupling as well as relativistic effects [26]. In addition to these corrections, jj-coupling has to be included. To estimate the magnetic moment of Er and Dy, we consider only LS-coupling without any additional corrections. For the ground state of Erbium $J = 6$ and for Dysprosium $J = 8$, giving $g_J \approx 1.167$ for Er and $g_J \approx 1.223$ for Dy. Experiments give a Landé factor of $g_J = 1.163\,801(1)$ for Er and $g_J = 1.241\,66(7)$ for Dy [27]. The energetically lowest magnetic states are $m_J = -6$ (Er) and $m_J = -8$ (Dy). The resulting magnetic moments (using the experimentally obtained Landé g- factors from [27]) are equal to $\mu = -6.983\,\mu_B$ for Erbium and $\mu = -9.933\,\mu_B$ for Dysprosium.

The above derivation is only valid for the bosonic isotopes, which do not feature a hyperfine splitting (i.e. $I = 0$, I being the nuclear spin quantum number). For the fermionic isotopes $I \neq 0$, thus one has to account for the magnetic moment of the different hyperfine levels. The magnetic moment is then given by

$$\mu = m_F g_F \mu_B, \tag{2.7}$$

where m_F is the magnetic quantum number for the total angular momentum of the atom F. The Landé g-factor of the atoms total angular momentum g_F is given by

$$g_F = g_J \frac{F(F+1) - I(I+1) + J(J+1)}{2F(F+1)}. \tag{2.8}$$

For the energetically lowest hyperfine state of ^{167}Er with an nuclear spin of $I = \frac{7}{2}$, $F = \frac{19}{2}$, with the lowest magnetic state being $m_F = -\frac{19}{2}$. For ^{161}Dy with an nuclear spin $I = \frac{5}{2}$, the energetically lowest state has a total angular momentum quantum number $F = \frac{21}{2}$, with the lowest magnetic state being $m_F = -\frac{21}{2}$. This results in a magnetic moment $\mu = -6.98\,\mu_B$ for ^{167}Er and $\mu = -9.93\,\mu_B$ for ^{161}Dy, which are

both equal to the magnetic moments of the bosonic isotopes [28]. In comparison, the magnetic dipole moment of Alkali atoms such as Rb is significantly smaller ($\mu_{Rb} = 1\,\mu_{\mathrm{B}}$).

Atoms with a permanent magnetic dipole moment feature an additional interaction – the dipole-dipole interaction (DDI). This interaction between two dipoles with a dipole moment μ, which are orientated along $\mathbf{e_1}$ and $\mathbf{e_2}$ can be written as [29]

$$U_{\mathrm{dd}}(\mathbf{r}) = \frac{\mu_0 \mu^2}{4\pi} \frac{(\mathbf{e_1} \cdot \mathbf{e_2})r^2 - 3(\mathbf{e_1} \cdot \mathbf{r})(\mathbf{e_1} \cdot \mathbf{r})}{r^5}, \tag{2.9}$$

where $\mathbf{r}$ is their relative position. In the presence of a magnetic field these atoms orientate along the field, leading to a polarized sample where all dipoles point in the same direction. The above expression then simplifies to [28]

$$U_{\mathrm{dd}}(\mathbf{r}) = \frac{C_{\mathrm{dd}}}{4\pi} \frac{1 - 3\cos^2\theta}{r^3}, \tag{2.10}$$

where $C_{\mathrm{dd}} = \mu_0 \mu^2$ denotes the dipolar interaction strength and θ gives the angle between the quantization axis and the interatomic axis of the two dipoles (see Fig. 2.1). The potential is long range ($\propto r^{-3}$) and anisotropic ($\propto (1 - 3\cos^2\theta)$).
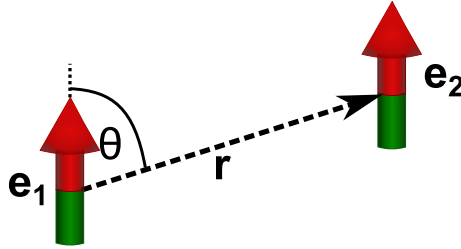
Figure 2.1.: Illustration of the parameters governing the interaction between two particles interacting via the dipole-dipole interaction.

The angular dependence of the DDI can be used to tune the interaction by altering the direction of the magnetic field. The factor $(1 - 3\cos^2\theta)$ changes from -2 to 1 when altering θ from 0° to 90°. Thus, the DDI can be attractive or repulsive, depending on θ. Two atoms that are arranged in an angle $\theta = 0°$ ('side-by-side' configuration) will repel each other, while atoms arranged in an angle $\theta = 90°$ ('head-to-tail' configuration) attract each other. This is illustrated in Fig. 2.2. Additionally, $U_{\mathrm{dd}} = 0$ for $\theta = 54.74°$.

Figure 2.2.: Illustration of the DDI between two particles. The dipoles are illustrated by red and green arrows, the direction of the force is represented by black arrows. The side-by-side configuration is illustrated in a), the head-to-tail configuration is shown in b).

The total interaction potential for dipolar atoms, accounting for both contact and DDI is given by

$$U(\mathbf{r}) = \frac{4\pi\hbar^2 a}{m}\delta(\mathbf{r}) + \frac{C_{\mathrm{dd}}}{4\pi}\frac{1 - 3\cos^2\theta}{r^3}. \tag{2.11}$$
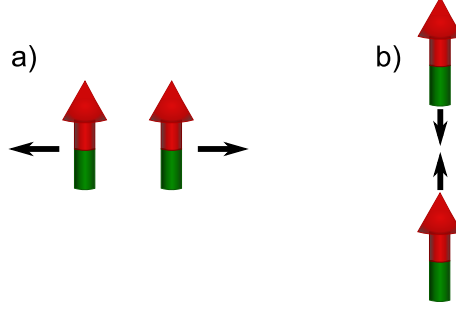
To compare the strength of the DDI to that of the contact interaction, we introduce the dipolar length [29]

$$a_{\mathrm{dd}} := \frac{\mu_0 \mu^2 m}{12\pi\hbar^2}, \tag{2.12}$$

which is equal to $a_{\mathrm{dd}} = 66\, a_0$ for ^{168}Er and $a_{\mathrm{dd}} = 130\, a_0$ for ^{164}Dy. In comparison, for ^{85}Rb the dipolar scattering length is equal to $a_{dd} = 0.69\, a_0$. The dipolar length gives the absolute strength of the DDI. The relative strength of the DDI compared to the contact interaction is given by [29]

$$\epsilon_{\mathrm{dd}} = \frac{a_{\mathrm{dd}}}{a_{\mathrm{s}}} = \frac{C_{\mathrm{dd}}}{3g} \tag{2.13}$$

where a_s is the contact interaction scattering length. The relative weight of the interaction can thus be tuned by changing a_{s} via the strength of the magnetic field. The DDI dominates over the contact interaction for $\epsilon_{\mathrm{dd}} > 1$.

2.1.3. Gross Pitaevskii equation

To derive an equation for the wave function describing a BEC of N bosons, we utilize the mean field approximation. In this approximation, the wave function describing the system Ψ can be written as a product of the individual particle wave functions ψ,

$$\Psi(\mathbf{r}_1, \mathbf{r}_2, ..., \mathbf{r}_N) = \prod_{i=1}^{N} \psi(\mathbf{r}_i), \tag{2.14}$$

where r_i is the coordinate of the i-th boson. This approximation is only valid for $a \ll n^{-1/3}$ (dilute quantum gas) or $a \geq n^{-1/3}$ (strongly interacting regime), where n

is the particle density. In this approximation the effective interaction potential can be replaced with a pseudo potential

$$U_{\mathrm{mf}} = gn(\mathbf{r}). \tag{2.15}$$

The Hamiltonian for this system can be written as

$$H = \sum_{i=1}^{N} \left[\frac{\mathbf{p}_i^2}{2m} + V(\mathbf{r}_i) \right] + g \sum_{i<j} \delta(\mathbf{r}_i - \mathbf{r}_j), \tag{2.16}$$

where $V(\mathbf{r}_i)$ is the external (trapping) potential.

The many body wavefunction $\Psi_0(\mathbf{r})$ describing a system with the aforementioned Hamiltonian can be derived using the Gross Pitaevskii equation (GPE), that was independently derived by Gross [30] and Pitaevskii [31] in 1961. For a contact interacting BEC the time-independent GPE reads

$$\left(-\frac{\hbar^2 \nabla^2}{2m} + V_{\mathrm{ext}}(\mathbf{r}) + g \left| \Psi_0(\mathbf{r}) \right|^2 \right) \Psi_0(\mathbf{r}) = \mu' \Psi_0(\mathbf{r}), \tag{2.17}$$

where $V_{\mathrm{ext}}(\mathbf{r})$ is the external potential and μ' is the chemical potential. The GPE has the form of a non-linear Schrödinger equation, where the potential is the sum of the external trapping potential and the mean field produced by the other bosons. The non-linearity stems from the interaction of the particles.

The DDI can be accounted for by adding another term Φ_{dd} to the mean field potential so that

$$\left(-\frac{\hbar^2 \nabla^2}{2m} + V_{\mathrm{ext}}(\mathbf{r}) + g \left| \Psi_0(\mathbf{r}) \right|^2 + \Phi_{\mathrm{dd}} \right) \Psi_0(\mathbf{r}) = \mu' \Psi_0(\mathbf{r}), \tag{2.18}$$

leading to the GPE describing BECs of atoms with strong magnetic dipole moment (dBEC). The term Φ_{dd} reads

$$\Phi_{\mathrm{dd}}(\mathbf{r}, t) = \int \left| \Psi(\mathbf{r}, t) \right|^2 U_{\mathrm{dd}}(\mathbf{r} - \mathbf{r}') d^3 r', \tag{2.19}$$

and is non-local due to the long range character of the interaction. It depends on the interaction of the majority of the dipoles and is therefore dependent on the dipole orientation and the shape of the BEC. In oblate traps, where the majority of the dipoles are aligned side-by-side (see Fig. 2.3b), the repulsive interaction dominates, leading to $\Phi_{\mathrm{dd}}(0) > 0$. In prolate traps (see Fig. 2.3a) the opposite is true, leading to $\Phi_{\mathrm{dd}}(0) < 0$.
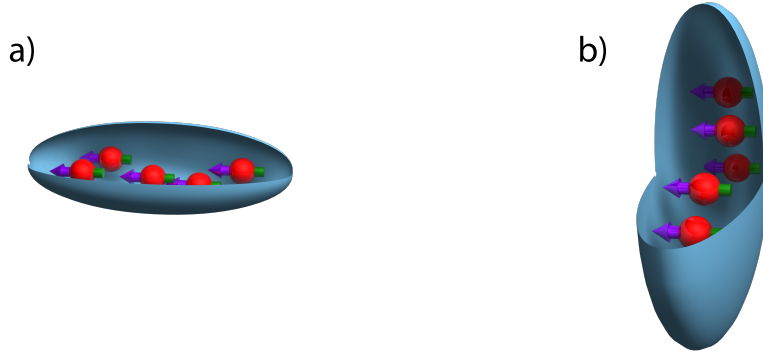
Figure 2.3.: Illustration of different trap geometries. Subfigure a shows the prolate trap where the majority of dipoles are aligned head-to-tail, b shows the oblate trap, where the dipoles are aligned side-by-side. Figure adapted from [32]

2.2. Optical dipole traps

Optical dipole trapping is the very basis for many modern cold atom experiments. While radiation pressure traps are used for the initial cooling of the atoms, optical dipole traps are used to cool the atoms to degeneracy and to manipulate the condensate. Compared to magnetic traps, dipole traps offer a greater geometric flexibility as they are not restricted by the arrangement of coils. This flexibility is important to achieve the ideal confinement (described in Chapter 4) of the BEC for the production of vortices, as well as the introduction of rotation into the system.

2.2.1. Oscillator model

The aforementioned external potential V_{ext} can be either created by laser light or magnetic fields. This thesis will focus on optical dipole traps, which are used in our experiment. Optical dipole traps are based on the interaction of the electric field **E** of the laser with the induced atomic dipole moment **p**. The negatively charged electrons are separated from the positively charged core due to the electric field, leading to an induced dipole moment. [33] In an isotropic medium the amplitude of the dipole moment p is directly proportional to the amplitude of the electric field E

$$p = \alpha E, \tag{2.20}$$

where α is the complex polarizability, governing the strength of the interaction between the medium and the electric field. It can be derived by modelling the motion of the electron with an harmonic oscillator with eigenfrequency ω_0. The damping of this motion stems from the spontaneous decay of the excited state population. In an ideal two-level system with ground state $|g\rangle$ and excited state $|e\rangle$ the damping rate of the motion can therefore be written as

$$\Gamma = \frac{\omega_0}{3\pi\epsilon_0\hbar c^3} |\langle e|\hat{d}|g\rangle|^2, \tag{2.21}$$

where $\hat{d} = -e\hat{r}$ is the electric dipole moment operator. The polarizability can be calculated using the equation of motion $\ddot{x} + \Gamma\dot{x} + \omega_0 x = -eE(\mathbf{r}, t)/m_e$, where

$$E(\mathbf{r}, t) = \mathbf{e}E(\mathbf{r})\exp(-i\omega t) + c.c \tag{2.22}$$

denotes the oscillating electric field. The polarizability α equates to

$$\alpha = \frac{e^2}{m_\text{e}} \frac{1}{\omega_0^2 - \omega^2 - i\omega\Gamma}. \tag{2.23}$$

This leads to two effects: First the potential energy of an atom in an oscillating electric field $E(\mathbf{r}, t)$ is given by

$$U_\text{dip} = -\frac{1}{2\epsilon_0 c}\text{Re}(\alpha)I, \tag{2.24}$$

where $\text{Re}(\alpha)$ is the real part of the polarizability describing the in-phase component of the dipole oscillation and I is the intensity of the field. This potential leads to a conservative force

$$F_\text{dip}(\mathbf{r}) = -\nabla U_\text{dip}(\mathbf{r}) = \frac{1}{2\epsilon_0 c}\text{Re}(\alpha)\nabla I(\mathbf{r}). \tag{2.25}$$

Secondly, the scattering rate is given by

$$\Gamma_\text{sc}(\mathbf{r}) = \frac{P_\text{abs}}{\hbar\omega} = \frac{1}{\hbar\epsilon_0 c}\text{Im}(\alpha)I(\mathbf{r}) \tag{2.26}$$

where P_abs is the power absorbed by the atom and $\text{Im}(\alpha)$ is the imaginary polarizability describing the out of phase component of the dipole oscillation.

In an ideal two level system, given that the detuning is $\Delta := \omega - \omega_0 \ll \omega_0$, the potential energy and scattering rate can be rewritten to

$$U_\text{dip}(\mathbf{r}) = \frac{3\pi c^2}{2\omega_0^3}\frac{\Gamma}{\Delta}I(\mathbf{r}) \tag{2.27}$$

and

$$\Gamma_\text{sc}(\mathbf{r}) = \frac{3\pi c^2}{2\hbar\omega_0^3}\left(\frac{\Gamma}{\Delta}\right)^2 I(\mathbf{r}) \tag{2.28}$$

using Eq. (2.23). This clearly shows that the sign of the detuning governs the interaction between the atom and the light field. For negative detuning (red detuned) the potential is negative and thus attracts atoms to the intensity maximum. For positive detuning (blue detuned) the atoms are repelled by high intensities. [33]

2.2.2. Multilevel atoms

We use a different picture to derive the effect of laser light on multilevel atoms. While the same results can be obtained when using a state dependent polarizability in the harmonic oscillator model, it is more intuitive to treat the effect of the far detuned laser light as a second order perturbation. As this perturbation of the energy levels is proportional to $|E(\mathbf{r}, t)|^2$, it is linear in the intensity $I(\mathbf{r}, t)$.

The second order perturbation of the state $|i\rangle$ by the Hamiltonian $\hat{H}_1$ is given by

$$\Delta E_i = \sum_{i \neq j} \frac{\left| \langle j | \hat{H}_1 | i \rangle \right|^2}{\mathcal{E}_i - \mathcal{E}_j}, \tag{2.29}$$

where $\mathcal{E}_i$ is the unperturbed energy of the i-th state. The Hamiltonian $\hat{H}_1$ is given by

$$\hat{H}_1 = \hat{d} E. \tag{2.30}$$

To derive the energy of $|i\rangle$ and $|j\rangle$, we utilize the dressed state picture. Setting the internal energy of the ground state to zero, the energy of the ground state $|i\rangle$ is solely given by the energy of the photons in the light field

$$\mathcal{E}_i = n\hbar\omega, \tag{2.31}$$

where n gives the number of photons. The energy of the state $|j\rangle$ is given by

$$\mathcal{E}_j = \hbar\omega_0 + (n-1)\hbar\omega \tag{2.32}$$

where $\hbar\omega_0$ is the energy difference between $|i\rangle$ and $|j\rangle$. For a two level atom this results in a light shift of the ground state $|g\rangle$ of

$$\Delta E = \pm \frac{\left| \langle e | \hat{d} | g \rangle \right|^2}{\Delta} |E|^2. \tag{2.33}$$

This simply equates to the AC-Stark shift. The dipole matrix element $\left| \langle e | \hat{d} | g \rangle \right|$ relates to the spontaneous decay rate as

$$\Gamma = \frac{\omega_0^3}{3\pi\epsilon_0\hbar c^3} \left| \langle e | \hat{d} | g \rangle \right|. \tag{2.34}$$

Consequently the light shift is dependent only on the detuning Δ, the spontaneous decay rate Γ and the intensity of the light field $I(\mathbf{r}, t) \propto |E|^2$.

In the case of multilevel atoms, we have to consider all of the allowed transitions from a ground state $|g_i\rangle$ to an excited state $|e_i\rangle$. In a first order approximation, only dipole allowed transitions are taken into account. The dipole allowed transitions are dependent on the angular momentum difference ΔJ of the ground and excited states ($\Delta J = 0, \pm 1$), as well as the parity of the wave function. In addition to this, the

polarization of the light field has to be considered, as different transitions can be addressed with different polarizations.

The specific transition element d_{ij} can be written as

$$d_{ij} = c_{ij}||\hat{d}||, \tag{2.35}$$

where $||\hat{d}||$ is the reduced matrix element and c_{ij} is the real transition coefficient. The reduced matrix element relates to the spontaneous decay rate according to Eq. (2.34). The coefficients c_{ij} depend, as mentioned above on the angular momentum difference ΔJ as well as the polarization of the laser light.

We can now write the energy shift of the ground state as

$$\Delta E_i = \frac{3\pi c^2 \Gamma}{2\omega_0^3} I \sum_j \frac{c_{ij}^2}{\Delta_{ij}}, \tag{2.36}$$

where Δ_{ij} is the detuning of the laser beam to the transition frequency of $|i\rangle \to |j\rangle$. Consequently the contribution of all coupled excited levels has to be considered to calculate the shift of the ground state [33]. This makes it exceedingly difficult to calculate the light shift for an increasing number of levels.

2.2.3. Anisotropic polarizability

The discussion above is based on the assumption that the medium is isotropic, i.e. that the polarizability of the atoms is independent of the direction of the electric field. Due to the non-zero orbital momentum quantum number L of Erbium and Dysprosium, both have to be considered as an anisotropic medium. Thus the atomic polarizability has to be written as a 3x3 tensor and the potential energy is modified to [34]

$$U(\omega) = -\frac{1}{2\epsilon_0} I(\mathbf{r}) \left[\alpha_{\mathrm{s}}(\omega) + |\mathbf{u}^* \times \mathbf{u}| \cos\theta_{\mathrm{k}} \frac{m_{\mathrm{J}}}{2J} \alpha_{\mathrm{v}}(\omega) + \right.$$
$$\left. \frac{3m_{\mathrm{J}}^2 - J(J+1)}{J(2J-1)} \frac{3\cos^2\theta_{\mathrm{p}} - 1}{2} \alpha_{\mathrm{t}}(\omega) \right] \tag{2.37}$$

where α_{s} is the scalar polarizability coefficient (diagonal elements of the polarizability tensor), α_v is the vectorial polarizability coefficient (antisymmetric parts of the off-diagonal elements) and α_{t} is the tensorial polarizability coefficient (symmetric parts of the off-diagonal elements). The polarization vector is denoted by $\mathbf{u}$, and θ_{k} and θ_{p} denote the angle between the propagation/polarization axis and the quantization axis which is set by the external magnetic field. For linear polarization the middle term of Eq. (2.37) vanishes as $|\mathbf{u}^* \times \mathbf{u}| = 0$. [35]

2.2.4. Polarizability of Erbium and Dysprosium

Figure 2.4 shows the calculated atomic polarizability for Erbium and Dysprosium under the assumption that $\theta_k = \theta_p = \pi/2$. This plot allows us to identify the wavelength regions which we can use to trap the atoms. [36, 37]

The wavelength used for the accordion lattice should be red detuned for both Er and Dy. Figure 2.4 clearly shows a red detuned region for wavelengths greater than 700 nm, as well as around 500 nm. Thus, both the fundamental (1064 nm) and the second harmonic (532 nm) of a high power Nd:YAG laser can be used for red detuned traps.

Blue detuned traps for both Er and Dy are more difficult to realize, as both species have many transition lines in the ultraviolet and blue region. Nonetheless, there is a blue detuned region for both species with not to many lines close by, at around 370 nm. This allows us to realize a blue detuned trap, giving us the possibility to create flat bottom potentials.
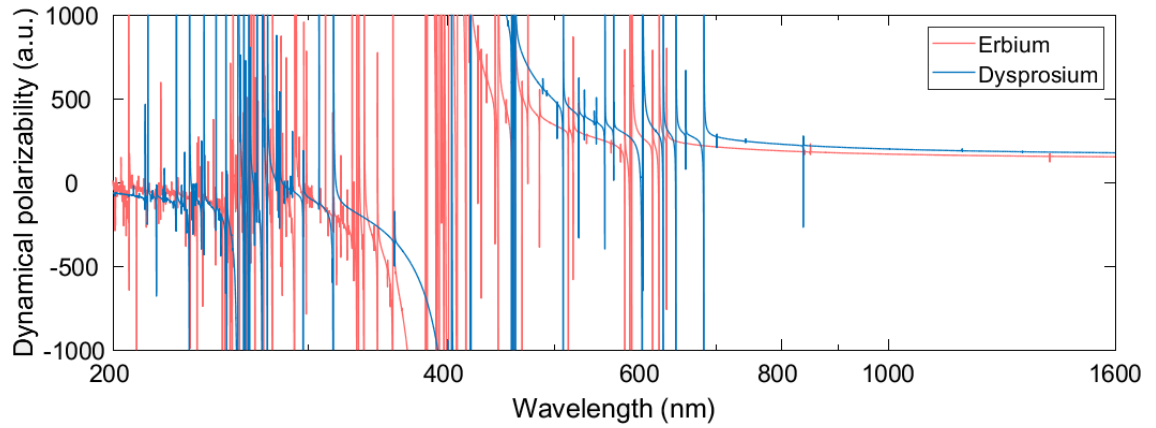

Figure 2.4.: Dynamic polarizability of Erbium and Dysprosium. The polarizability of Erbium is displayed in red, that of Dysprosium is displayed in blue. The finite height of the narrower lines comes from the finite step size of the calculation. [36, 37]

3. Vortices in Bose-Einstein Condensates

3.1. Superfluid Properties of a Bose-Einstein Condensate

Superfluidity has first been demonstrated independently by Pyotr Kapitza [19] and John F. Allen and Don Misener [20] in 1938. They observed the frictionless flow of Helium II through narrow capillaries. The theory behind this phenomenon has later been developed by L. Landau in 1941 [38]. He formulated a general argument to show when a fluid can transport mass without friction, based on the idea that an elementary excitation of the system can only occur when such an excitation is energetically favourable.

A single excitation with momentum $\mathbf{p}$ can change the energy of the fluid by $\epsilon(\mathbf{p}) + \mathbf{p} \cdot \mathbf{v}$, where $\epsilon(\mathbf{p})$ denotes the dispersion relation. This process is only energetically favourable for $\epsilon(\mathbf{p}) + \mathbf{p} \cdot \mathbf{v} < 0$. This is the case for $v > \frac{\epsilon(\mathbf{p})}{\mathbf{p}}$. Thus the critical velocity v_c is given by

$$v_{\mathrm{c}} = \min_{\mathbf{p}} \frac{\epsilon(\mathbf{p})}{\mathbf{p}}, \tag{3.1}$$

where the minimum is calculated over all values of $\mathbf{p}$. Hence, excitations with $v < v_{\mathrm{c}}$ cannot couple to the fluid [39].

In a interacting BEC, the dispersion relation is given by the Bogoliubov dispersion law [40]

$$\epsilon(p) = \left[c^2 p^2 + \left(\frac{p^2}{2m} \right)^2 \right]^{1/2}, \tag{3.2}$$

where c is the speed of sound in the BEC and p is the momentum. The Bogoliubov excitation spectrum for a weakly contact interacting Bose-Einstein condensate is illustrated in Fig. 3.1a). For small momenta $p \ll mc$, the excitation spectrum is linear and follows a phonon like dispersion relation ($\epsilon(p) = cp$). In the high momentum limit $p \gg mc$ the dispersion relation becomes $\epsilon(p) = \frac{p^2}{2m} + mc^2$, thus resembling that of a free particle with an additional interaction energy $c^2 m$. The critical velocity of the weakly contact interacting BEC is given by the speed of sound c, as illustrated in Fig. 3.1a). Consequently, the BEC can be considered superfluid for $c \neq 0$.
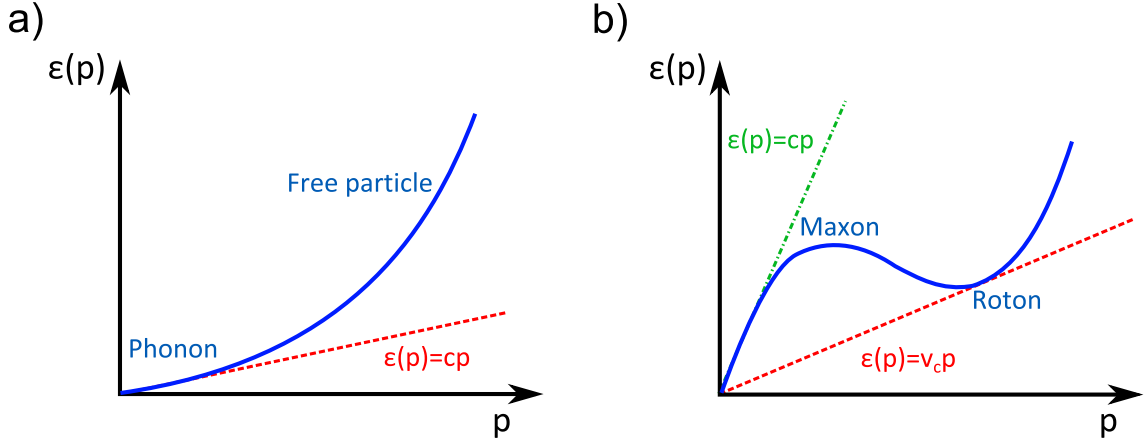
a)

b)

Figure 3.1.: Schematic graph of the excitation spectrum of a Bose-Einstein condensate a) without and b) with a roton minimum. The blue line shows the excitation spectrum, the dashed red line illustrates the critical velocity of the BEC. The green dotted line in subfigure b) marks the speed of sound.

For a strongly interacting quantum fluid, such as superfluid He, the excitation spectrum features a local minimum at finite momentum, which is referred to as the roton minimum. It has been observed in superfluid He in 1961 [41]. Here, the roton momentum is inversely proportional to the interatomic distance. In a trapped dipolar BEC (dBEC) the roton occurs despite the absence of strong interactions, due to the anisotropic long range character of the DDI, for $\epsilon_{dd} \gtrsim 1$. Here, the roton occurs at a momentum which is inversely proportional to the harmonic oscillator length in z-direction. The occurrence of the roton in dBECs has recently been experimentally observed by Chomaz et al. in 2018 [42]. The roton minimum changes the critical velocity, as illustrated in Fig. 3.1b). Thus the critical velocity of a dBEC is not necessarily equal to the speed of sound. [43]

3.2. Quantized vortices

An ordinary fluid is described by a many-body wavefunction depending on the coordinates of all particles, a superfluid on the other hand, can be described by a wavefunction that requires only a single position coordinate $\mathbf{r}$. In the hydrodynamic description, the wavefunction $\Psi(\mathbf{r}, t)$ depends on two real fields - the superfluid density field $n(\mathbf{r}, t)$ and the phase field $S(\mathbf{r}, t)$, such that [44]

$$\Psi(\mathbf{r}, t) = \sqrt{n(\mathbf{r}, t)} e^{iS(\mathbf{r}, t)}. \tag{3.3}$$

The velocity field of this wave function can be written as

$$\mathbf{v}(\mathbf{r}, t) = \frac{\hbar}{m} \nabla S(\mathbf{r}, t). \tag{3.4}$$

As the velocity field is equal to the gradient of the phase field it is irrotational i.e. $\nabla \times \mathbf{v}(\mathbf{r}, t) = 0$. Hence the superfluid cannot react to rotational excitations in the

same way as a normal fluid. When the superfluid is placed in a rotating container it will remain at rest for rotation frequencies below a critical rotation frequency. Nonetheless at some point this will become energetically unfavourable. The energy of the superfluid E_r with angular momentum $\mathbf{L}$ and energy E in a container rotating with angular frequency $\mathbf{\Omega}$ is given by

$$E_\mathrm{r} = E - \mathbf{\Omega} \cdot \mathbf{L}, \tag{3.5}$$

in the rotating frame. At high angular frequencies a state with $\mathbf{\Omega} \cdot \mathbf{L} > 0$ becomes energetically favourable to the $L = 0$ state. The system then starts to develop vortices, i.e. regions around which the fluid rotates.

The circulation κ of a vortex is given by

$$\kappa = \oint_C d\mathbf{r} \cdot \mathbf{v}(\mathbf{r}, t) \tag{3.6}$$

where C denotes a closed contour around the vortex core. Using the definition of the velocity field (3.4), the circulation is

$$\kappa = \frac{\hbar}{m} \oint_C d\mathbf{r} \cdot \nabla S(\mathbf{r}, t) = \frac{\hbar}{m} \Delta S, \tag{3.7}$$

where ΔS is the change in phase when going from the starting to the end point of the closed contour. As the wave function has to be single-valued, $\Delta S = 2\pi q_\nu$ with $q_\nu \in \mathbb{Z}$. This gives

$$\kappa = \frac{h}{m} q_\nu, \tag{3.8}$$

where q_ν denotes the vortex charge. The circulation is therefore quantized in multiples of h/m. [39, 44] The sign of the vortex charge gives the direction of rotation. For $\mathrm{sgn}\, q_\nu = +1$, we refer to the object as a vortex, for $\mathrm{sgn}\, q_\nu = -1$ it is called anti-vortex. The only point where the phase is not well defined is the centre of circulation ($\mathbf{r} = 0$). To have a defined wave function $\Psi(\mathbf{r}, t)$ at $\mathbf{r} = 0$, the density $n(\mathbf{r} = 0, t) = 0$, meaning that there is a density hole in the superfluid at the centre of rotation. The phase profile of a vortex as well as the velocity field is illustrated in Fig. 3.2.

The angular momentum per particle is given by

$$l_\mathrm{z} = \frac{m}{N} \int d\mathbf{r} (\mathbf{r} \times \mathbf{v})_\mathrm{z} n(\mathbf{r}) = \hbar, \tag{3.9}$$

where N is the total number of particles in the condensate. The creation of a vortex with energy E_ν and vortex charge q_ν becomes energetically favourable for

$$E_\nu < \mathbf{\Omega} \cdot \mathbf{L} \rightarrow \Omega > \frac{E_\nu}{N h q_\nu}, \tag{3.10}$$

with $\mathbf{L}_\mathrm{z} = L_\mathrm{z} = l_\mathrm{z} N$ and $\mathbf{\Omega} = \Omega_\mathrm{z}$. For a trapped BEC in the Thomas-Fermi regime the critical angular velocity Ω_cr can be calculated to be [45]

$$\Omega_\mathrm{cr} = \frac{5}{2} \frac{\hbar}{m R_\perp^2} \ln \left(\frac{0.67 R_\perp}{\xi} \right), \tag{3.11}$$
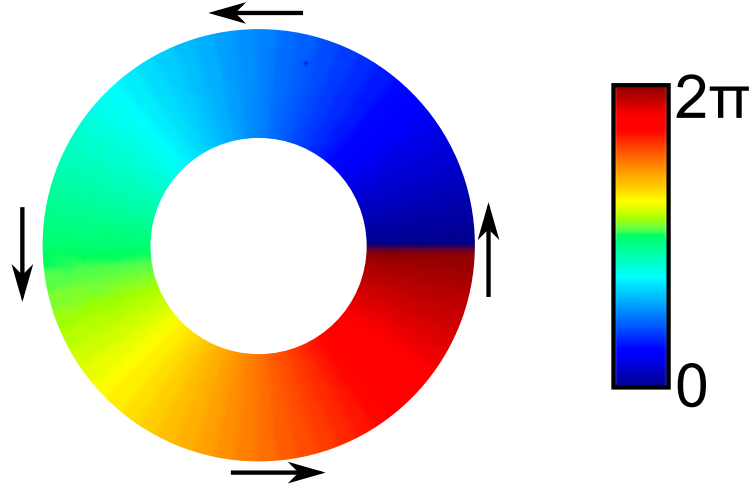
Figure 3.2.: Schematic sketch of the phase profile and velocity field of a quantized vortex with $q_\nu = 1$. The colour scale gives the phase of the wave function, the black arrows represent the velocity field. The hole in the centre illustrates the vortex core.

where $R_\perp$ is the condensate size in the radial plane and ξ is the healing length (the derivation of ξ can be found in Subsection 3.3). This formula is, with some modifications, also valid for the dBEC. Even though the healing length is altered by the DDI, this should not alter Ω_{cr} profoundly as $\Omega_{cr} \propto \ln(\xi^{-1})$. The dominant alteration of Ω_{cr} is expected to be due to the rescaling of the radial size $R_\perp$ due to the DDI [46]. According to theory [46] the main change of Ω_C in a dBEC is due to the alteration of the radius of the BEC by the DDI. The critical rotation frequency thus decreases in an oblate trap and increases in a prolate trap.

3.3. Density profile of a quantized vortex

The reaction of a BEC to the hole in the centre of the vortex can be described using the GPE (see Subsection 2.1.3). For a contact interacting BEC, the GPE (see also equation (2.17)) reads

$$\left(-\frac{\hbar^2 \nabla^2}{2m} + V_{\mathrm{ext}}(\mathbf{r}) + g \left| \Psi_0(\mathbf{r}) \right|^2 \right) \Psi_0(\mathbf{r}) = \mu \Psi_0(\mathbf{r}). \qquad (3.12)$$

To obtain the density profile of a vortex, we consider the example of a 1D BEC confined by a potential $V_{\mathrm{ext}} = 0$ from $0 < x < \infty$ with a hard wall potential ($V_{\mathrm{ext}} = \infty$) at $0 > x > -\infty$. This leads to the boundary condition $\Psi_0(x = 0) = 0$. As $x \to \infty$ the homogeneity (particle density n) of the BEC is restored, leading to $\mu = gn$. The characteristic length scale at which changes in the density and phase of the condensate are removed by the interactions, is given by $\xi = \hbar/p'$. Here p' is the momentum at which the transition from the phonon to the free particle regime takes

place (see Subsection 3.1). It is given by

$$\frac{p'^2}{2m} = mc^2, \tag{3.13}$$

thus

$$p' = \sqrt{2}mc. \tag{3.14}$$

We refer to ξ as the healing length which can be written as [39, 47]

$$\xi = \frac{1}{\sqrt{2}}\frac{\hbar}{mc}. \tag{3.15}$$

Using $\tilde{\Psi}_0 = \Psi_0/\sqrt{n}$ and introducing $\tilde{z} = z/\xi$ gives a dimensionless form of the GPE equation:

$$-\frac{d^2}{d\tilde{z}^2}\tilde{\Psi}_0(\tilde{z}) + \tilde{\Psi}_0(\tilde{z})^3 = \tilde{\Psi}_0(\tilde{z}) \tag{3.16}$$

which can be solved by $\tilde{\Psi}_0(\tilde{z}) = \tanh\frac{x}{\sqrt{2}\xi}$. The healing length thus gives the lengthscale over which the BEC recovers from a disturbance of the density. [39, 44] This is illustrated in Fig. 3.3. As a vortex creates a hole in the density profile of the BEC, the healing length governs the size of the vortex core.
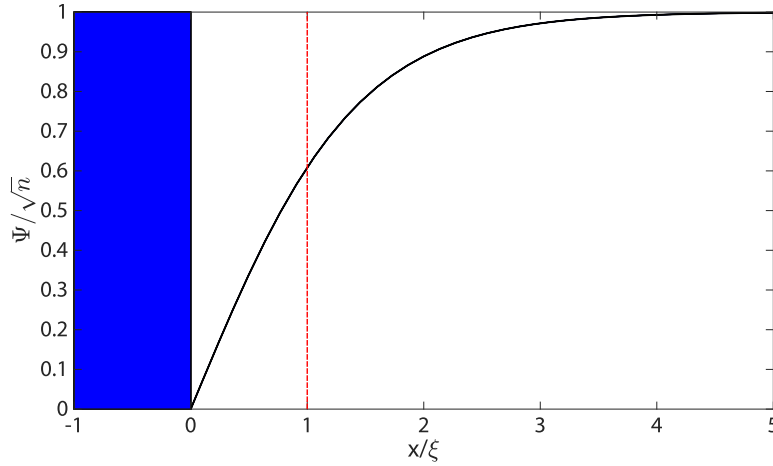
Figure 3.3.: Reaction of the wave function of a weakly interacting BEC to a hard wall blue detuned potential. The hard-walled potential is illustrated in blue, the wave function is displayed in black. The wave function returns to its original value on the order of the healing length ξ

The parameter governing the healing length of a BEC is the speed of sound c, which is strongly dependent on the interactions present in the system. For a weakly interacting BEC with only contact interactions, the speed of sound is given by

$$c = \sqrt{\frac{gn}{m}}. \tag{3.17}$$

Equation (3.15) can thus be rewritten as

$$\xi = \frac{1}{\sqrt{8\pi na}}.$$

(3.18)

In BECs with DDI, the speed of sound is anisotropic. For a 3D uniform dipolar condensate, the speed of sound is given by [48]

$$c(\theta) = \sqrt{\frac{gn}{m}\left[1 + \epsilon_{dd}(3\cos^2\theta - 1)\right]},$$

(3.19)

with θ denoting the angle between the direction of the excitation momentum and the dipole axis in momentum space. This formula is valid for the phonon modes of the 3D uniform dipolar condensate. Thus the healing length of the dBEC is anisotropic, leading to an asymmetric density profile of the vortex. The numerically calculated vortex profiles for different ϵ_{dd} and α are illustrated in Fig. 3.4. The numerical simulation [49] assumes a two-dimensional dBEC, where α gives the angle between the z-axis and the dipole orientation. The first picture shows a vortex in the purely contact interacting case ($\epsilon_{dd} = 0$). The second part displays the density profile of a vortex in a BEC with DDI, where the dipoles are tilted.
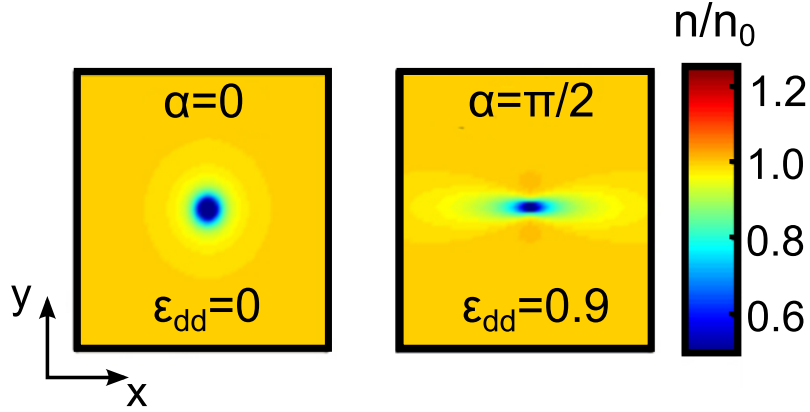

Figure 3.4.: Numerically calculated density profiles of vortices with different dipole orientations and dipolar interaction strengths. The calculation assumes a BEC with a single plane of dipoles. Here α is the angle between the z-axis and the orientation of the dipoles and ϵ_{dd} gives the relative strength of the DDI compared to the contact interaction. Figure adapted from [49]

In the case of trapped dBECs, the roton minimum can alter the density profile of the vortex core. When the energy of the roton is close to zero, the roton mode is populated due to the perturbation of the potential by the vortex. This leads to the emergence of density ripples around the vortex core with a wavelength related to the wavelength of the roton. These ripples align in the direction of the attractive dipolar interactions and decay with increasing distance from the vortex core. [48, 49, 50]

When the roton minimum approaches zero (i.e. roton softening) a new state of matter, the supersolid, emerges [51, 52, 53]. The formation and properties of vortices

in a supersolid go beyond the scope of this thesis, but will be the topic of further investigations.

3.4. Multiple vortices

As discussed in Section 3.2, the formation of a single vortex is energetically favourable for BECs rotating with a frequency $\Omega \geq \Omega_{cr}$. As can be seen in Eq. (3.10) Ω_{cr} is directly proportional to the circulation. For angular momenta $\Omega \geq 2 \cdot \Omega_{cr}$ it is energetically favourable for the system to have a total circulation of $\kappa = 2 \cdot h/m$, which can, in principle, either be supported by one vortex with $q_\nu = 2$ or two vortices with $q_\nu = 1$ each. To see which of these options is energetically favourable, one has to consider the kinetic energy of a vortex. Assuming a cylindrical condensate with height L and radius R, where $\xi \ll R$, the kinetic energy associated with the velocity field of a vortex with vortex charge q_ν can be written as [48]

$$E_{\text{kin}} = \frac{L\pi n\hbar^2}{m} q_\nu^2 \ln \frac{R}{\xi}. \tag{3.20}$$

Due to the quadratic dependence on the vortex charge q_ν, two vortices with $q_\nu = 1$ are energetically favourable to a doubly charged vortex, when neglecting the interactions between two vortices.

The interaction of two vortices with vortex charges q_1 and q_2 can be understood when looking at the interaction of their velocity fields. For two vortices rotating in the same direction ($\text{sgn}\, q_1 = \text{sgn}\, q_2$) the velocity fields have opposite directions in the region between the vortices. This leads to a slower flow of the fluid in between the vortices than outside. Following Bernoulli's principle, the pressure is lower in the outside region, leading to a repulsive interaction between the vortices. The opposite is true for a vortex anti vortex pair ($\text{sgn}\, q_1 = -\text{sgn}\, q_2$).

The same conclusion can be drawn from looking at the total kinetic energy of the vortices across the system. For a cylindrical condensate with the same geometry as assumed for (3.20) and two vortices in a distance d with vortex charges q_1 and q_2 the total kinetic energy is equal to [48]

$$E_{\text{kin}} = \frac{L\pi n\hbar^2}{m} \left[q_1^2 \ln \frac{R}{\xi} + q_2^2 \ln \frac{R}{\xi} + 2q_1 q_2 \ln \frac{R}{d} \right], \tag{3.21}$$

where the first two terms are the energy of the single vortices and the last term is their interaction energy. For vortex-vortex pairs this term is positive, thus the total energy is minimized for large separations d. The opposite is true for vortex - anti-vortex pairs.
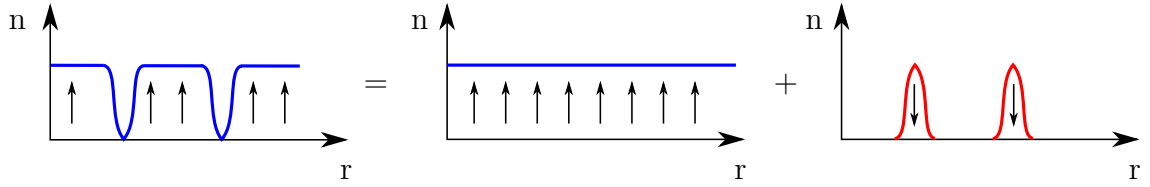
Figure 3.5.: Illustration of the interaction of two vortices in a dBEC. The orientation of the dipoles is symbolized by the direction of the arrows. Figure adapted from [48].

In dipolar condensates the interaction of vortices cannot be described by the interaction of their velocity fields alone. They exhibit an additional interaction, as the vortices can be considered as anti-dipoles in empty space. This is illustrated in Fig. 3.5. Consequently the interaction becomes dependent on the orientation of the dipoles relative to the plane of rotation [48]. For large separations d, the logarithmic hydrodynamic interaction dominates the DDI. The interaction of a vortex pair is thus most significantly modified for short to mid range separations ($d < 10\xi$) [54].

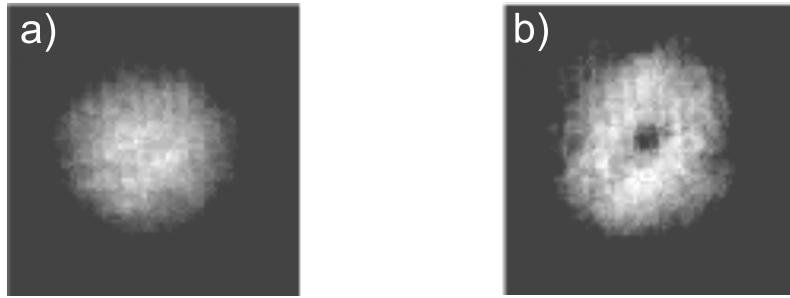## 3.5. Creation of Vortices in Bose-Einstein Condensates

Figure 3.6.: Transverse absorption image of a BEC stirred with a laser beam, a) below and b) above the critical rotation frequency. Figure adapted from [55].

Numerous experimental methods have been used to create vortices in BECs. The first successful creation of vortices in a BEC has been performed by Matthews et al. in 1999 [21], where they formed the desired vortex wave function directly via coherent transitions in a two component BEC. Here one component (i.e. one spin state of ^{87}Rb) forms a vortex while the other component fills the vortex core.

An alternative approach is the direct rotation of the BEC using stirring potentials. This approach is more flexible as it does not require resonant interactions with the BEC. It has first been demonstrated by Madison et al. in 1999 [55]. They utilize a red-detuned laser beam, superimposed with the potential of a Ioffe-Pritchard trap to create a cigar shaped harmonic trap with an anisotropic transverse potential. By rotating the laser beam, they can shift this anisotropy, similar to rotating a bucket of

fluid to create a vortex. Here the anisotropy of the potential replaces the roughness of the bucket walls. The transverse absorption image of the BEC at different rotation frequencies is shown in Fig. 3.6.

Recent developments in spatial light modulation technology have lead to new, more flexible possibilities to induce rotation in a BEC. A DMD (Digital Micromirror Device) (see Section 5.1) can be used to alter the profile of a laser beam in a (nearly) arbitrary way. This can be used to create vortices either via the rotating bucket approach, where an anisotropic trap is rotated or by moving obstacles through the Bose-Einstein condensate. This approach has been demonstrated by Gauthier et al. [56] in 2019. They create giant vortex clusters by stirring the BEC with two pedal potentials.

4. Accordion lattice set-up

The aim of this master thesis is to built an optical setup to create vortex excitations in a dBEC of Erbium and Dysprosium. To this end, we developed two setups, one to trap the atoms in an appropriate geometry and the other to create the vortex excitations. In this chapter we will review the setup designed for creating an appropriate trapping potential. The desired properties of this potential are discussed in Section 4.1. We planned the necessary optical setup (see Sections 4.3 and 4.2), constructed a test setup (see Section 4.4) and characterized the resulting trap (see Section 4.5).

4.1. Desired properties of the trapping potential

We aim to trap the BEC in an optical dipole trap with an appropriate geometry for the creation of vortices. We assume a harmonic trap with

$$V_{\text{ext}}(\mathbf{r}) = \frac{m}{2} \left[\omega_x^2 x^2 + \omega_y^2 y^2 + \omega_z^2 z^2 \right] , \tag{4.1}$$

where ω_i denotes the trap frequency in $i-$direction. The vortex line is orientated along the axial (z)-direction. The trap as well as the orientation of the vortex is illustrated in Fig. 4.1. The fluid rotates around the vortex core in the x-y-plane.
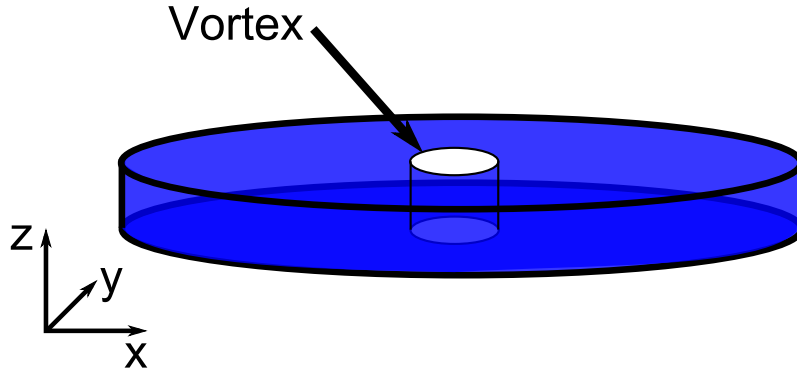

Figure 4.1.: Illustration of the trap geometry used for the creation of vortices as well as the orientation of the vortex line.

4.1.1. Axial confinement

Vortices are topologically stable excitations of a superfluid BEC. Nonetheless, for finite temperature systems, vortices can decay due to the presence of the thermal

cloud, which provides a source of dissipation. In finite temperature systems, long wavelength transverse helicoidal deformations of the vortex line known as Kelvin waves can be thermally excited. These deformations cause the vortex to quiver and emit acoustic radiation, enabling the vortex to dissipate energy. [57]

In a dBEC the three dimensional character of the vortex is expected to be even more significant due to the long range character of the DDI. Different parts of the vortex line can interact due to the non-local DDI, leading to an alteration of the stability [58]. As these excitations are three-dimensional, they can be suppressed by reducing the size of the condensate in direction of the vortex line [57]. This can be achieved by tightening the confinement along the vortex line (z-direction) such that

$$l_{\mathrm{z}} = \sqrt{\frac{\hbar}{m\omega_{\mathrm{z}}}} \approx \xi, \tag{4.2}$$

where l_{z} is the harmonic oscillator length in z-direction. As the vortex line cannot support deformations in the transversal direction, the Kelvin mode contribution is essentially frozen out. When the above criterion is fulfilled, the vortex is considered to be two-dimensional. It is important to note while the vortex dynamics are 2D, the condition

$$\hbar\omega_z \gg k_{\mathrm{B}}T \tag{4.3}$$

for a two dimensional BEC is not necessarily fulfilled.

We estimate the healing length of Er and Dy considering only the influence of the contact interaction as there is no analytic formula for the anisotropic healing length of a dBEC. This estimate gives us a healing length (according to Eq. (3.15)) on the order of $1\,\mu\mathrm{m}$ for both Er and Dy, based on parameters typically found in our experiments. The healing length corresponds to a trapping frequency of $\omega_{\mathrm{z}} \approx 2\pi{\cdot}2\,\mathrm{kHz}$. As this is only a crude estimate, we will design the system such that it is possible to reach $\omega_{\mathrm{z}} \approx 2\pi{\cdot}\ 4\,\mathrm{kHz}$ to be able to compensate for influences of the dipole-dipole interaction on the healing length.

4.1.2. Radial confinement

The trapping potential in the radial (x-y-) plane governs the motion of the vortex core. Similar to objects in a classical fluid, the vortex core moves due to a density gradient force and the Magnus effect. As the density in the vortex core vanishes, the core experiences a force towards regions with low densities. This resembles the classical buoyant force, which causes a bubble within a fluid to experience a force which is anti-parallel to the pressure gradient. The Magnus effect causes a rotating cylinder to drift perpendicular to an applied force. Thus the vortex core moves perpendicular to both its quantization axis and the density gradient force. Consequently the vortex core precesses around the trap centre in an inhomogeneous, axisymmetric ($\omega_{\mathrm{x}} = \omega_{\mathrm{y}} := \omega_{\mathrm{r}}$) BEC [59]. The precession frequency ϕ_0 is given by [60]

$$\phi_0 = \frac{2\hbar\omega_{\mathrm{r}}^2}{8\mu(1 - r_0^2/R_\perp^2)} \left(3 + \frac{\omega_{\mathrm{r}}^2}{5\omega_{\mathrm{z}}^2}\right) \ln\left(\frac{2\mu'}{\hbar\omega_{\mathrm{r}}}\right) \tag{4.4}$$

where ω_r and ω_z are the radial and axial trapping frequencies respectively. The radial coordinate of the vortex is given by r_0, μ' gives the chemical potential and $R_\perp$ is the radial Thomas-Fermi radius of the BEC. We introduce the aspect ratio AR, defined as

$$\mathrm{AR} = \frac{\omega_\mathrm{z}}{\sqrt{\omega_\mathrm{x}\omega_\mathrm{y}}}. \tag{4.5}$$

As the precession frequency is inversely proportional to AR, the motion of the vortices can be minimized by either maximizing AR for a given ω_z or reducing the distance r_0 from the trap centre. We minimize ϕ_0, to rule out complications caused by the unknown influence of the DDI on the precession of the vortex.

We aim to ensure a low precession frequency by maximizing the aspect ratio. While it would also be possible to minimize r_0, we want to be able to produce multiple vortices to study their interaction without additional influences of the trap. As the trapping frequencies in the radial plane are too low to hold the BEC, the confinement in the radial plane has to be provided by an additional potential. This will be achieved using a blue detuned beam modulated by a DMD, which is also used to introduce rotation in the system (see Chapter 5). Additionally the DMD could be used to compensate the remaining radial confinement, so that the Bose-Einstein condensate is uniform. This can be done by choosing the pattern on the DMD such that the resulting intensity distribution has the opposite curvature as the trap, creating an effective flat-bottom potential.

The discussion above assumes the case of a axisymmetric trap ($\omega_\mathrm{x} = \omega_\mathrm{y}$). In non-axisymmetric traps ($\omega_\mathrm{x} \neq \omega_\mathrm{y}$) the rotating walls induce an irrotational flow in the system, which is also present in the absence of vortices. This additional velocity field influences the critical rotation frequency of the condensate. Moreover the vortex precesses around the centre of a non-axisymmetric trap in an elliptical trajectory [61]. We aim to avoid these additional effects by choosing the trap parameters such that the confinement in the x-y-plane is symmetrical.

Summing up, the three requirements for the trap are a strong axial confinement, making the vortices two dimensional, ensured by $\omega_\mathrm{z} \approx 2\pi \cdot 4\,\mathrm{kHz}$, a high aspect ratio to minimize the precession of the vortices $\omega_\mathrm{z} \gg \sqrt{\omega_\mathrm{x}\omega_\mathrm{y}}$ and an axi-symmetric radial confinement $\omega_\mathrm{x} \approx \omega_\mathrm{y}$. This trap geometry is commonly referred to as a pancake trap.

4.2. Accordion lattice

According to the discussion above, a pancake like trapping potential with tight axial confinement is ideal for the creation of vortices. Such a confinement cannot be achieved with a crossed beam optical trap, where ω_z is on the order of a few hundred Hertz for typical laser powers. Alternative approaches include a gravito-optical surface trap [62], based on an repulsive evanescent wave against which the atoms are pushed by gravity. This concept however requires placing a prism inside the vacuum chamber, which limits the optical access for future experiments. Another possibility would be to focus a red-detuned beam using a cylindrical lens, leading to a tight
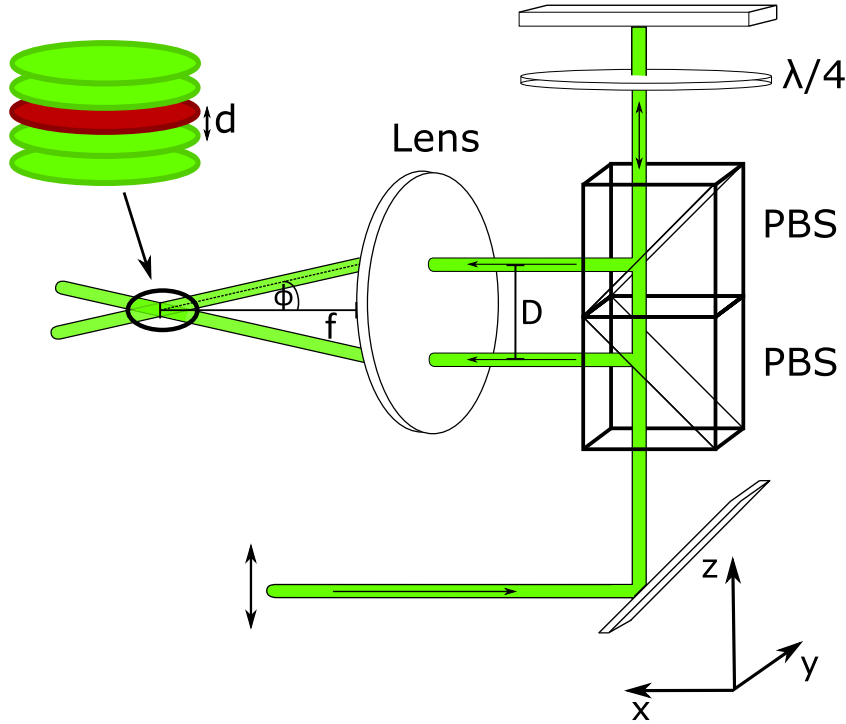
Figure 4.2.: Schematic illustration of the accordion lattice setup. A change in the height of the incoming beam results in a change of the distance D of the beams reflected by the polarizing beam splitter (PBS) cubes. This leads to a change in their angle of interference ϕ, which alters the spacing d of the interference pattern. The interference pattern is sketched in the inset, with the red plane marking the central fringe of the lattice.

focus in one direction, which results in a high trap frequency in this direction [63]. Considering the limitations set by the minimal focal lengths, which is constrained by the size of our vacuum chamber, this approach is not feasible as it leads to a non-axisymmetric trapping potential.

The desired geometry can also be achieved using a one-dimensional lattice, created by the interference of two counter-propagating laser beams. The 1D lattice consists of a linear array of pancake shaped traps with a lattice spacing of $\lambda/2$. For a typical trapping wavelength of $\lambda = 1064\,\mathrm{nm}$, a BEC with a Thomas Fermi radius of $R_{\mathrm{TF}} \approx 10\,\mu\mathrm{m}$ (commonly found in our experiments) occupies around 20 lattice sides. This is problematic as the linear array is orientated along the imaging axis. As the individual lattice sites in an array cannot be resolved with a standard imaging technique, we would need a lattice with a spacing of $\approx 10\,\mu\mathrm{m}$ to trap the condensate in a single lattice site. This would require a wavelength of $20\,\mu\mathrm{m}$. Thus an alternative approach is needed.

A one-dimensional optical lattice with tunable lattice spacing and confinement, (commonly known as accordion lattice) allows us to achieve the desired trapping parameters, while enabling us to trap the atoms in a single lattice side. Instead of two counter propagating beams, the accordion lattice is formed by two beams

interfering at a shallow angle. This is illustrated in Fig. 4.2. The lattice spacing d can be altered by changing the angle of interference ϕ. Thus we can reach $d = 10\,\mu\text{m}$ allowing us to trap the entire condensate in a single lattice site. The axial trapping frequency in a lattice with a $d \approx 10\,\mu\text{m}$ is on the order of a few hundred Hertz for typical laser powers. As the axial trapping frequency is indirectly proportional to the d, we decrease the lattice spacing after trapping the condensate, until ω_z is at $\approx 2\pi \cdot 4\,\text{kHz}$. Owing to the fact that the tunnelling rates for the final lattice configuration are small ($\approx 1 \cdot 10^{-11}\,\text{s}^{-1}$ for our setup), we can ignore the influence of the lattice structure on the system. This setup was first proposed by Li et al. [64] in 2008. The first experimental implementation of this optical accordion lattice setup with ^{87}Rb was achieved by Ville et al. [65] in 2017.

The two beams used to form the accordion lattice are created by splitting a single laser beam using the setup shown in Fig. 4.2. The polarization of the incoming beam is chosen such that half of the intensity is reflected at the first PBS cube. The transmitted beam passes a second PBS cube and a quarter-wave plate ($\lambda/4$). It is then reflected by a mirror, passing the $\lambda/4$ plate a second time. After passing the $\lambda/4$ plate twice, the polarization of the beam has been rotated by 90° such that it is reflected by the second PBS cube. The two beams interfere in the focal point of a lens with focal length f. The half-angle ϕ between the two beams is equal to

$$\phi = \arctan \frac{D}{2f}, \tag{4.6}$$

where D is the distance between the two beams. This distance can be altered by changing the height of the incoming beam on the first mirror.

The lattice spacing can be derived using Fourier optics. The field in the focal point of the lens $U_0(x, y, f)$ is the Fourier transform of the incoming field on the lens $U(x, y, 0)$. Consequently, for two beams with a distance of $\pm D/2$ from the centre of the lens, the fields can be written as

$$U_0^{\pm D/2}(x, y, f) = \exp\left(\pm i \frac{\pi D}{\lambda f} x\right) U(x, y, 0) \tag{4.7}$$

resulting in an intensity

$$I(x, y, f) = 2\left(\cos \frac{2\pi D}{\lambda f} x + 1\right) I(x, y, 0). \tag{4.8}$$

The spacing of the resulting interference pattern d is thus

$$d = \frac{\lambda f}{D}. \tag{4.9}$$

Hence, real time control of the height of the incoming beam leads to real time control of D, allowing the tuning of d during the experimental sequence. This enables us to load the entire condensate into a single lattice side and then decrease the lattice spacing adiabatically.

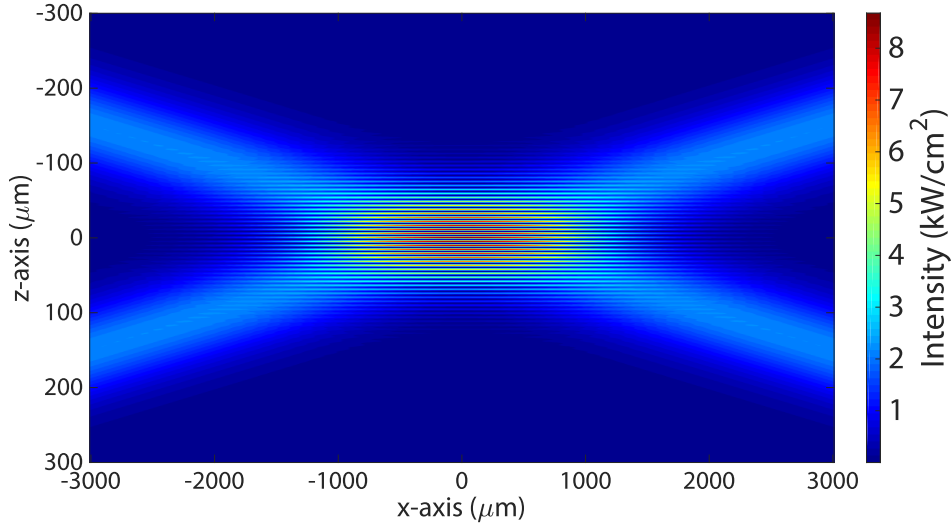## 4.3. Numerical calculation of trap parameters

Figure 4.3.: Numerically calculated interference of two Gaussian Beams in the x-z-plane. The beams propagate along the x-direction.

The trapping frequencies $(\omega_x, \omega_y, \omega_z)$ of the accordion lattice depend on the wavelength λ of the laser beam, the power P, the beam waists in the focal point (w_y, w_z) as well as the half-angle ϕ at which the beams interfere. To find the right parameters so that the lattice fulfils the desired properties discussed in Section 4.1, we calculate the trap frequencies numerically. The Matlab script can be found in Appendix A.1. We calculate the values of the electric fields $E_{1,2}(\mathbf{r})$ for discrete positions on a grid. This is then used to derive the intensity pattern $I(\mathbf{r})$ around the point at which the beams interfere (i.e. the focal point of the lens), as well as the resulting trap frequencies. The trap frequencies in x-direction are given by

$$\omega_x = 2\pi \cdot \sqrt{\frac{k_x}{m}} \quad \text{with} \quad k_x = \frac{\partial^2 U(x,0,0)}{\partial x^2}\bigg|_{x=0}, \qquad (4.10)$$

where $U(x,y,z)$ is the trapping potential, derived using Eq. (2.24). To find the optimum parameters, we vary w_y from $100\,\mu m$ to $3000\,\mu m$ in steps of $100\,\mu m$ and w_z from $20\,\mu m$ to $500\,\mu m$ in steps of $10\,\mu m$. The half-angle ϕ is kept constant at the maximum achievable angle $\phi = 5.711°$, which is limited by the optical access of the viewport of the vacuum chamber. We use the maximum achievable ϕ to get the the maximal AR and ω_z. The obtained intensity in the x-z plane is shown in Fig. 4.3.

There are two main wavelengths which we consider for the accordion lattice: 532 nm and 1064 nm. Both wavelengths are red detuned for Erbium and Dysprosium (see Section 2.2) with similar polarizabilities for both species. At 532 nm, the polarizabilities of Er and Dy are equal to 317 a.u. and 350 a.u. respectively, at 1064 nm, they equate to 176 a.u. (Er) and 184 a.u. (Dy) [35, 66]. High power commercial
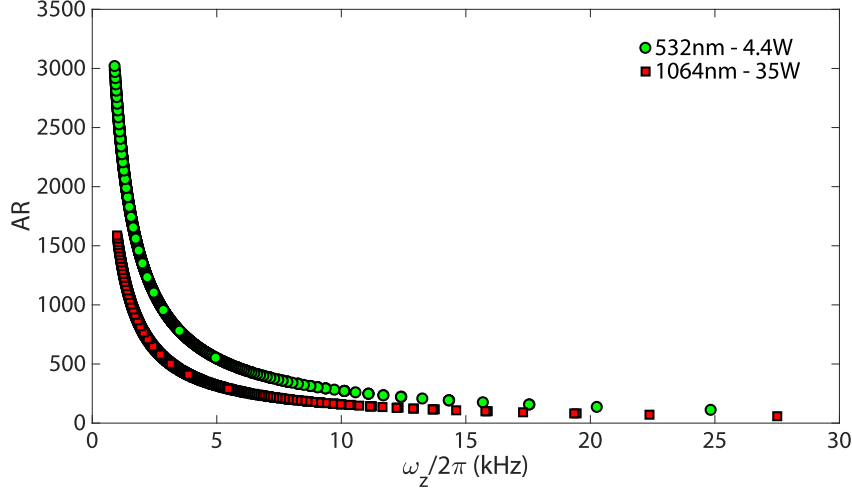
Figure 4.4.: Comparison of the aspect ratio in dependence of the axial trapping frequency for wavelengths 532 nm and 1064 nm. The data points for 532 nm are marked in green, the ones for 1064 nm are marked in red. The data was obtained using a numerical calculation of the trap parameters, for fixed power and angle of interference.

laser sources at both wavelengths are readily available. In order to find out which wavelength is more suitable for our experimental setup, we calculate the trapping potential for both and compare the parameters of the trap. We do this at a fixed power of $P = 4.4$ W for 532 nm and $P = 35$ W for 1064 nm. These powers are limited by the maximum available laser powers as well as the losses and limits arising from additional optical elements such as an acousto-optical modulator (AOM) used for the intensity stabilization and an optical fiber used for mode cleaning.

The trapping potentials for 532 nm and 1064 nm differ mainly in the achievable aspect ratio AR for a given ω_z. We calculate AR and ω_z for each pair w_y, w_z. All combinations give a functional form between AR and ω_z, displayed in Fig. 4.4. The aspect ratio grows for decreasing ω_z. At a given ω_z the AR is significantly higher for 532 nm than for 1064 nm. As a high AR is favourable for the production of vortices (see Section 4.1.2), we choose $\lambda = 532$ nm for the accordion lattice setup.

Another key parameter is the symmetry of the lattice in the axial plane. This symmetry can be altered by changing the ratio of the beam waists w_y and w_z. To find the optimum parameters, we introduce the symmetry factor

$$S = \left| \frac{\omega_x}{\omega_y} - 1 \right| \tag{4.11}$$

which can take values between 0 and 1. The trap is symmetric in the radial plane when $S = 0$. The graph in Fig. 4.5a depicts both the AR and the symmetry factor as a function of the beam waists (w_y, w_z). A symmetry factor of $S = 0$ is possible for nearly all aspect ratios.

As seen in Fig. 4.5a, the symmetry condition is fulfilled for a fixed ratio w_y/w_z. To determine the desired ratio of the beam waists, we only consider the beam waists
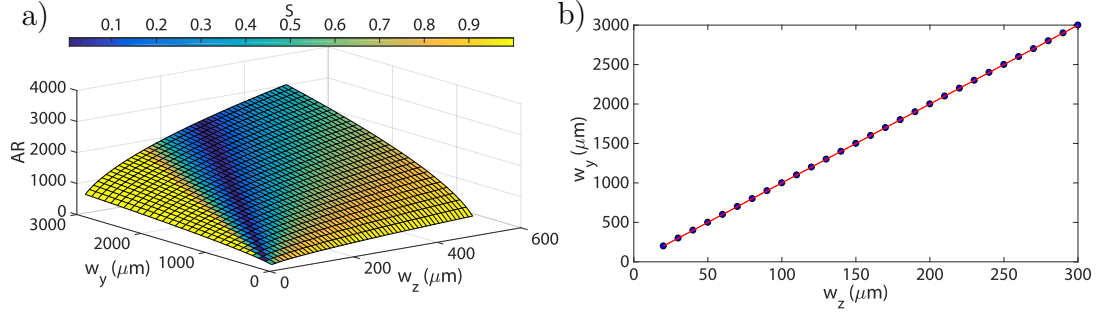
Figure 4.5.: Graphs to determine the conditions for $S = 0$. A three-dimensional plot of the aspect ratio AR in dependence of the beam waists is shown in a). The colour scale marks the symmetry factor S. The beam waists for which $S < 0.01$ are plotted in b). The data points are displayed in blue, a linear fit of the curve is displayed in red.

for which $S < 0.01$. Due to the discreteness of the step size of the calculation, we do not obtain $S = 0$. Figure 4.5b) shows the beam waists w_y, w_z for which $S < 0.01$. We approximate the dataset using a linear equation to determine the ratio of the waists. The slope k of the resulting line is equal to 10. Consequently we design the system such that $w_y = 10 \cdot w_z$.
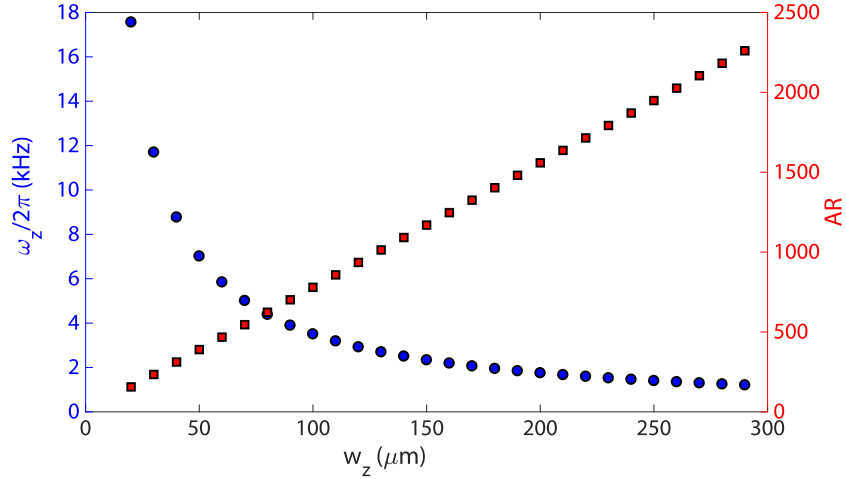

Figure 4.6.: Aspect ratio AR and vertical trapping frequency ω_z in dependence of the vertical beam waist. The beam size in the horizontal direction is fixed to $w_y = 10 \cdot w_z$ to fulfil the requirement $S < 0.01$. The vertical trapping frequency ω_z is marked with blue dots, the AR is marked with red squares.

To choose w_z we have to find a compromise between the axial trapping frequency ω_z and the aspect ratio AR. Increasing the beam size at a given power decreases the intensity, causing a decrease of the trapping frequencies ω_y and ω_z. At the same time, the aspect ratio increases. This is shown in Fig. 4.6, where the aspect ratio AR and the trapping frequency ω_z is plotted in relation to w_z, for pairs of beam waists (w_y, w_z) fulfilling the symmetry condition $w_y = 10 \cdot w_z$. As discussed in Section 4.1.1, we want

to achieve $\omega_z \approx 2\pi \cdot 4\,\text{kHz}$. Hence we choose the beam waists at the focal point to be $(w_y, w_z) = (900, 90)$ µm, resulting in trap frequencies of $(\omega_x, \omega_y, \omega_z) = 2\pi \cdot (5.56, 5.56, 3898)$ Hz (AR ≈ 701.1), for the maximum achievable half-angle $\phi = 5.71°$.

4.4. Experimental implementation

As discussed in Section 4.2, the key feature of the accordion lattice is the ability to change the trapping frequencies and lattice spacing by altering the angle of interference of two beams. This is accomplished using the setup depicted in Fig. 4.2. The distance of two parallel beams can be changed by varying the height of the incoming beam. The beams interfere in the focal point of a lens with $f = 200\,\text{mm}$. The focal length was chosen so that the lens can be placed outside the vacuum chamber. The optical setup includes a part to produce two parallel beams (see 4.4.1), a setup to alter the height of the incoming beam (see 4.4.2), as well as the focusing optics used to interfere the two beams (Subsection 4.4.3) and additional optical elements (Subsection 4.4.4).

4.4.1. Beam separation

We designed a housing for the optical components (excluding the lens), shown in Fig. 4.2, to minimize disturbances caused by air turbulences and to achieve a good passive mechanical stability of the optical components relative to each other. The housing is shown in Fig. 4.7. It consists of 6 anodized aluminium plates with a mean thickness of 6.5 mm and was machined in-house. A 2 inch mirror is mounted under a 45° angle to direct the light upwards. Two 1 inch PBS cubes are placed in a milling pocket to ensure the correct orientation. They are glued to the side of the tower using two-components-epoxide resin glue. The parallelism of the two cubes is vital for the setup. We ensured it by checking that the two outgoing beams are parallel before fixing the cubes. This was done by verifying that the separation of the two beams remains constant for different distances from the tower. This test was repeated after fixing the cubes. A $\lambda/4$-plate in a rotational mount and a 1 inch mirror are mounted above the PBS cubes. The tower is designed so that all optical elements are centred on the PBS cubes. The adjustment screws of the mirror mount are accessible outside the tower, so that the alignment can be done without opening the tower. There are openings in the aluminium plates on

Figure 4.7.: Rendered image of the self designed tower used to create two parallel beams with tunable spacing.

both sides of the PBS cubes, allowing the light used for the experiment as well as the stray light, which is transmitted by the first PBS cube and then reflected by the
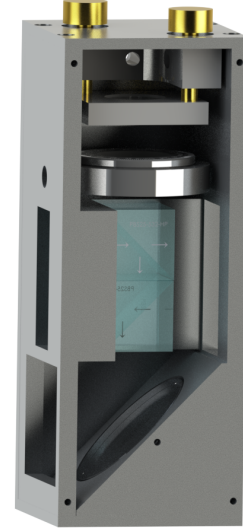
second cube, to leave the tower. This should reduce heating of the tower caused by stray light.
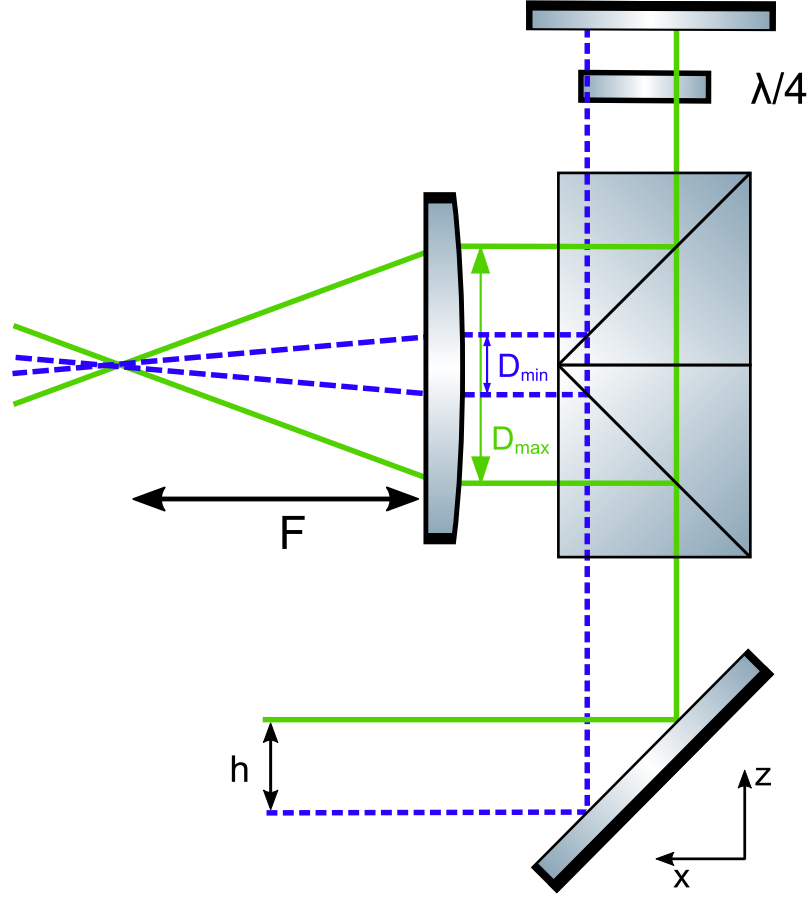

Figure 4.8.: Illustration of the accordion lattice setup for minimum and maximum beam separations D. The beams with minimum (maximum) separation are displayed in blue (green).

The maximum half-angle of interference is equal to $\phi_{max} = 5.711°$, as discussed in Section 4.2. For a lens with $f = 200\,\text{mm}$, this equates to a beam distance $D_{max} = 40\,\text{mm}$. The limiting factor for the minimum angle is the free aperture of the $\lambda/4$-plate, which is smaller than the free aperture of the other optical elements. We use a 1 inch zero-order quarter-wave plate from Thorlabs (WPQ10M-532), which is specified to have a clear aperture of 22.6 mm. As the wave plate is centred on the cubes, the smallest possible beam separation is equal to $D_{min} = 4.8\,\text{mm}$, which is equal to an angle of $\phi_{min} = 0.57°$. The beams with maximum and minimum separation are illustrated in Fig. 4.8. The lattice spacing d can be varied from 2.66 µm to 22.2 µm and the trapping frequencies $(\omega_x, \omega_y, \omega_z)$ can be altered from $2\pi\cdot(0.55, 5.56, 422)$ Hz $(\phi = 0.57°)$ to $2\pi\cdot(5.56, 5.56, 3898)$ $(\phi = 5.71°)$ at a laser power of 4.4 W. The numerically calculated trap frequencies ω_x and ω_z for different ϕ are shown in Fig. 4.9.
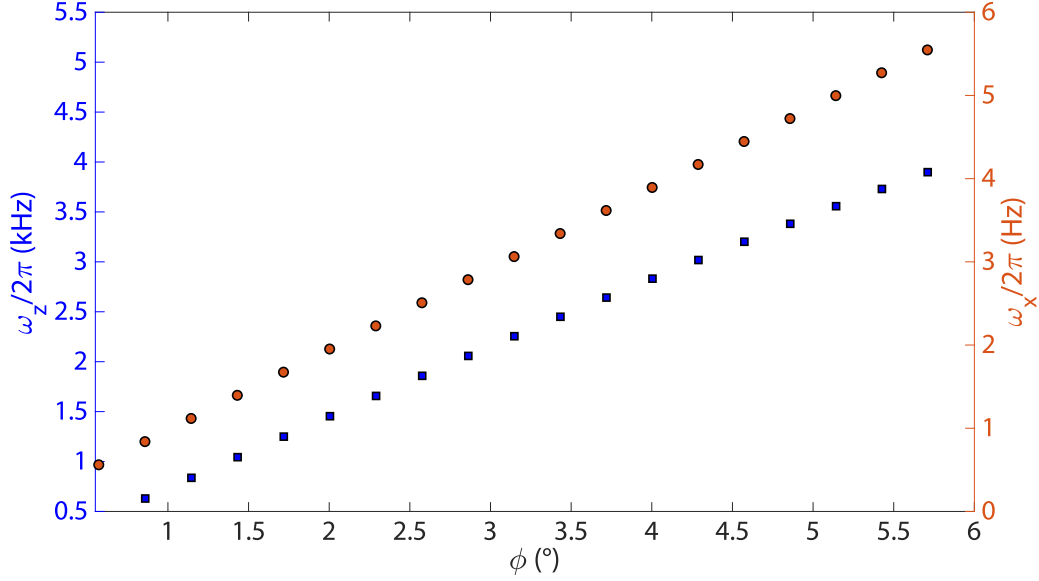
Figure 4.9.: Numerically obtained trap frequencies ω_x and ω_z for different angles ϕ at $P = 4.4\,\text{W}$. The trap frequencies in z(x)-direction are marked by the blue(orange) squares(circles). The beam size was fixed at $(w_y, w_z) = (900\,\mu\text{m}, 90\,\mu\text{m})$

The minimum beam separation could be decreased by changing the position of the wave plate. As the distance of the beams at maximum separation to the edge of the wave plate is larger than the distance at the minimum separation, the wave plate could be shifted from being centred on the cubes towards the beam position at the minimum beam separation by $\approx 2\,\text{mm}$. This modification would allow for a smaller minimum angle of interference, leading to a higher maximum lattice spacing, while the minimum lattice spacing remains the same.

4.4.2. Beam displacement

To go from the maximum (D_max) to the minimum (D_min) beam separation, the incoming beam has to be shifted by a distance h in z-direction (see Fig. 4.8). The distance h can be determined geometrically to be

$$h = \frac{D_\text{max} - D_\text{min}}{2} = 17.6\,\text{mm}. \tag{4.12}$$

There are multiple possibilities to do this. We looked more closely into the following methods:

- Moving the beam in the optical plane using a mirror mounted on a linear translation stage

- Altering the angular position of the beam with an acousto-optical deflector (AOD)

49

- Changing the height of the beam by rotating two parallel mirrors

Moving the beam using a mirror mounted on a linear translation stage requires a slight alteration of the experimental setup (see Fig. 4.2 and 4.7). Instead of mounting the 45° mirror parallel to the reflecting planes of the PBS cubes, it has to be turned by 90° around the z-axis. Then a translation of the beam in the optical plane will result in the desired shift in the distance of the two output beams. Commercially available linear translation stages with a travel range of 20 mm are specified to have a velocity of 200 mm/s. Consequently we can shift from the maximum to the minimum beam separation in ≈ 0.1 s. This provides only a lower bound for the time-scale, as it does not account for the time needed to accelerate and decelerate the stage. While this time scale is appropriate for an adiabatic compression of the condensate, it could be a limiting factor for possible future experiments (e.g. quench experiments). Thus, we consider other, faster options.

Another possibility is to alter the angle using an AOD, which utilizes the acousto-optic effect to spatially control the beam. The diffraction angle of the AOD is dependent on the frequency of the sound-wave propagating inside the crystal. Thus, by altering the frequency, the beam can be deflected to different angular positions. A lens is needed to be able to convert the angular shift of the beam into a positional shift. Typical commercial AODs offer a scan angle of $\approx 2°$. A lens with a focal length $f = 350$ mm is required to convert this angular shift into a positional shift of 2 cm. This results in a strongly focused beam inside the AOD, which further limits the maximum power that can be used, owing to the damage threshold of the AOD as well as thermal effects [67].
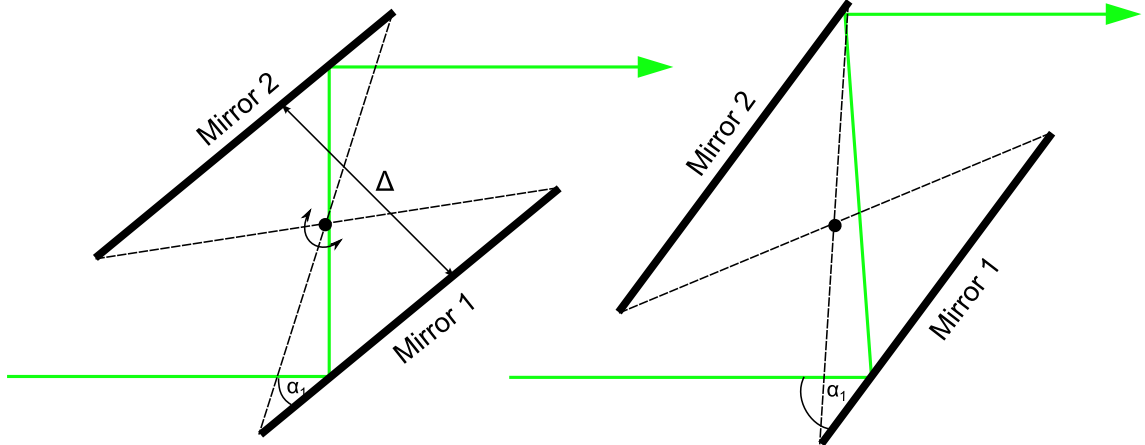
Figure 4.10.: Schematic sketch of the beam displacement using parallel mirrors. Two mirrors are placed in a distance Δ parallel to each other. The angle between the mirrors and the beam is given by α. After the two reflections the outgoing beam is parallel to the incoming beam. The height of the outgoing beam is dependent on the angle α. Thus by altering α, the beam can be displaced parallely.

The third options is to change the height of the beam by altering the angle of two parallel mirrors relative to the beam. This concept is illustrated in Fig. 4.10. The

beam is reflected by the first mirror (M1) and by the second mirror (M2), which is placed parallel to M1 in a distance Δ. This double reflection leads to a shift in the height of the beam. By changing the angle α between the mirrors and the incoming beam, the resulting beam height can be changed.

To find the distance Δ, the length of the mirrors and the angular shift resulting in the desired height displacement, we wrote a Matlab code (see Appendix A.2) to calculate the displacement of the beams analytically. The beam and the mirrors are both expressed as vectors. We calculate the intersection points and angles and use this to propagate the beam using geometric optics. The calculation was performed with different centres of rotation, which does not have an influence on the beam displacement. Thus, we chose the centre of rotation to be in the centre of the two mirrors. According to our calculation, a change in angle of 20° results in a vertical displacement of 18.6 mm. We use a DRTM 40-SM rotary stage from OWIS with a maximum angular velocity of 2500 °/s. This angular velocity corresponds (according to our simulations) to a velocity of approximately 2300 mm/s, which is a factor of 10 larger than the velocity of the linear translation stage.
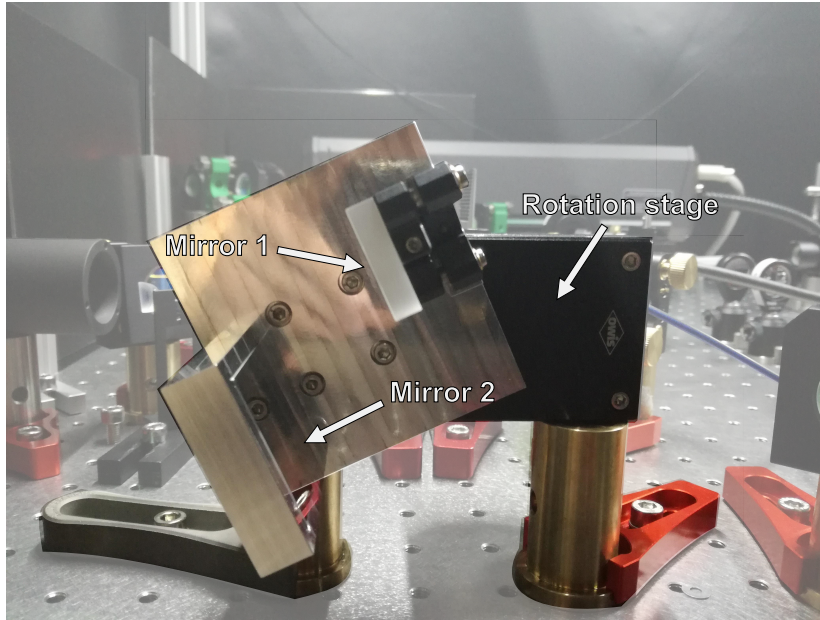
Figure 4.11.: Mounting of the two mirrors on the rotational stage. The first mirror is mounted on a kinematic mirror mount so that it is possible to alter its tilt in both directions. The mount was designed such that the centre of mass is at the centre of rotation.

The geometry of the mount was determined using the code in Appendix A.2. The first mirror is chosen to be smaller than M2, so that it does not cut off the beam after the reflection by the second mirror. The displacement of the beam position on M2 when going from the maximum angle to the minimum angle, is large compared to the displacement on M1. Hence M2 is longer than the first one. The second mirror is horizontally displaced with respect to M1 to be able to utilize its entire size. Both

mirrors are rectangular with lengths 25.4 mm (M1) and 35 mm (M2). As the height of M2 is larger than that of the first, M1 is mounted on a base plate such that the beam hits the centre of both mirrors. They are mounted in a distance $\Delta = 35.4$ mm.

Several points need to be considered to ensure the optimal performance of the system. First, to avoid a rotating unbalance, the mount was designed such that the centre of mass coincides with the centre of rotation. We have also tested a setup where the centre of mass is not equal to the centre of rotation. This decreases the repeatability of the system. Second, the parallelism of the two mirrors is essential for the beam translation. When the two mirrors are not parallel, the beam is not displaced parallely when changing α. This effect cannot be compensated for by mirrors after the rotation stage, leading to a shift of the interference pattern when changing the confinement of the accordion lattice. Hence the first mirror is mounted on a small kinematic mirror mount, enabling fine-tuning of the vertical and horizontal tilt. The final setup is shown in Fig. 4.11. The parallelism of the mirrors can be checked by looking at the vertical and horizontal position of the beam after the two mirrors for different α. The shift of the beam in vertical and horizontal position was minimized by altering the angle of mirror 1 in relation to mirror 2 as well as the angle of the incoming beam on the mirrors.

4.4.3. Focusing Optics

The two parallel beams interfere in the focal point of a lens. It is critical for the accordion lattice that the position of the focus does not change when altering the angle of interference. The shift of the focal point was obtained with Zemax OpticStudio, using a large incoming beam to simulate different beam separations. The spread of the focal position of the large beam is equivalent to the shift of the focal point during the compression of the lattice. When using a standard cylindrical lens, the position of the focal point shifts by 2 mm during the compression (see Fig. 4.12a,b). This shift is caused by spherical aberrations, causing the focal point to be dependent on the distance of the centre of the lens. This can be avoided by using an aspherical lens, which has a form that deviates from the standard spherical form. For an aspherical lens the shift reduces to ≈ 2 μm (see Fig. 4.12c,d)

As discussed in Section 4.3 the optimum beam size is $(w_y, w_z)=(900\,\mu\text{m}, 90\,\mu\text{m})$. Owing to the fact that a beam with a waist of 900 μm has a Rayleigh length of 4800 mm, it is effectively collimated. Thus the incoming beam has to be divergent to obtain the desired beam waist after the lens. This can be achieved by inserting a cylindrical lens in front of the aspherical lens so that the incoming beam is divergent in y-direction. An alternative approach would be to shape the beam such that it is collimated with $w_y = 900$ μm prior to the last lens. The beam can than be focused only in z-direction using an acylindrical lens. As an acylindrical lens with a focal length of $f = 200$ mm is not a standard component, we decided to use a planoconcave cylindrical lens to expand the beam in y-direction in front of the aspherical lens. This setup is illustrated in Fig. 4.12e. The distance between the two lenses is chosen such that the beam is collimated in y-direction after the pair of lenses. We use

a cylindrical lens with a focal length $f = -75\,\mathrm{mm}$ that is placed in a distance of $125\,\mathrm{mm}$ from the aspherical lens. Back propagating the desired waist in the focal point through the optical system yields an input beam waist of $w_\mathrm{y} = w_\mathrm{z} = 337.5\,\mathrm{\mu m}$.
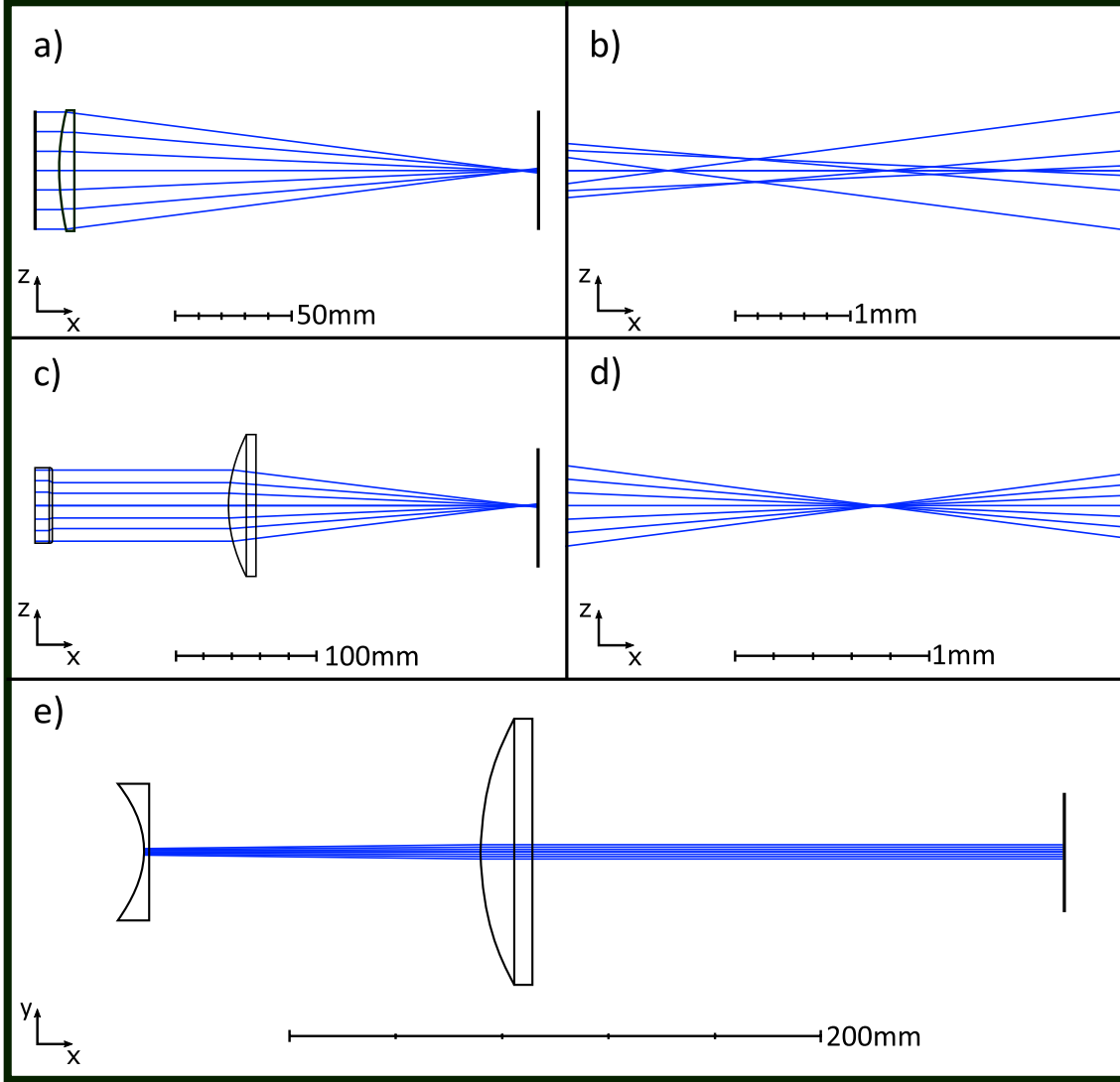
Figure 4.12.: Comparison of the shifts caused by spherical aberrations of different optical setups. The waist of the incoming beams $w = 50\,\mathrm{mm}$. The optical setup with a single cylindrical lens (f=200 mm) is shown in a), a zoom-in on the focal point is shown in b). Subfigure c) shows the optical setup consisting of a cylindrical lens with (f=$-75\,\mathrm{mm}$) in a distance of 125 mm from an aspherical lens (f=200 mm). Subfigure e) depicts the same optical setup as c) tilted by 90° around the x-axis. The graphs were made using Zemax OpticStudio.

The choice of a two-lens setup offers another great advantage. By removing the cylindrical lens, the waist in y-direction is decreased by a factor of 10, while the position of the interference point is not significantly altered. Beam waists $w_\mathrm{y} = w_\mathrm{z} =$

90 µm result in trapping frequencies $(\omega_x, \omega_y, \omega_z)= 2\pi\cdot(20\,\text{Hz},\, 196\,\text{Hz},\, 14\,000\,\text{Hz})$ for a power of 5 W. While this trap does not provide the symmetry in the x-y plane desired for the creation of vortices, ω_z is high enough to fulfil the requirement for the quasi 2D confinement for a gas of distinguishable particles [1]

$$\hbar\omega_z \gg k_B T, \tag{4.13}$$

for typical temperatures of $T = 100\,\text{nK}$. This means that the motion in z-direction is essentially frozen out and the BEC is quasi two-dimensional. Thus, by placing the cylindrical lens on a flip mount, we have the possibility to create quasi-2D dipolar Bose-Einstein condensates.

4.4.4. Additional optical elements

Up to now, all calculations have assumed a perfect interference of the beams, leading to a full contrast of the lattice. This is only true when the beams have the same polarization and the power in both beams is equal. When the two beams do not have the same polarization, the minima of the interference patterns will not be equal to zero. We utilize Thorlabs PBS25-532-HP PBS cubes, which are specified to have the highest extinction ratio $(T_p : T_s > 2000 : 1)$ when used in transmission, but are not specified in reflection. As we use the beams reflected by the two PBS cubes in the tower, we insert two additional cubes after the tower. These cubes are rotated by 90° around the x-axis relative to the cubes in the tower. The s-polarized light reflected by the PBS cube in the tower is thus p-polarized with respect to the PBS cube outside and is transmitted, leading to a clean interference of the two beams. We were able to observe a significant increase in the contrast after inserting the cubes.
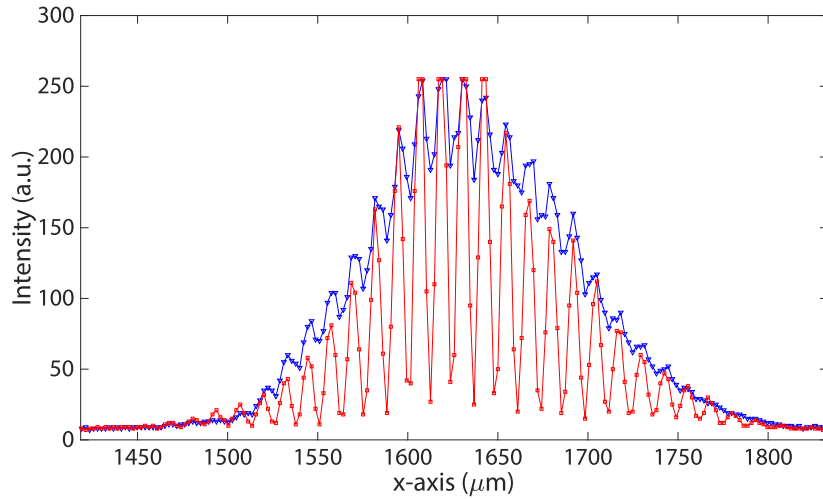

Figure 4.13.: Comparison of lattice before(blue triangles) and after (red squares) inserting the cubes and controlling the power balance. The line serves as a guide to the eye.

---

[1]In a Bose-Einstein Condensate this condition is weakened due to the phenomenon of transverse condensation. However, the discussion of this phenomenon goes beyond the scope of this thesis.

The power ratio of the two beams has a similar influence as the polarization. If the power is unequally distributed between the two beams, the minima of the interference pattern will not be at zero intensity. The ratio can be controlled using a $\lambda/2$ waveplate in front of the tower. The polarization of the incoming beam is chosen such that half of the intensity is reflected at the first PBS cube and half is transmitted. The comparison of the interference pattern before and after inserting the cubes and controlling the power balance is shown in Fig. 4.13. The pictures were taken using an AV U-503B camera with a pixel size of 2.2 µm. It is important to note that this camera has a higher pixel size than the camera used for the characterization of the lattice (see Sec. 4.5). The fact that the minima of the interference pattern are not at zero intensity after inserting the cubes and controlling the power can be explained by the finite size of the pixels.

4.4.5. Experimental setup
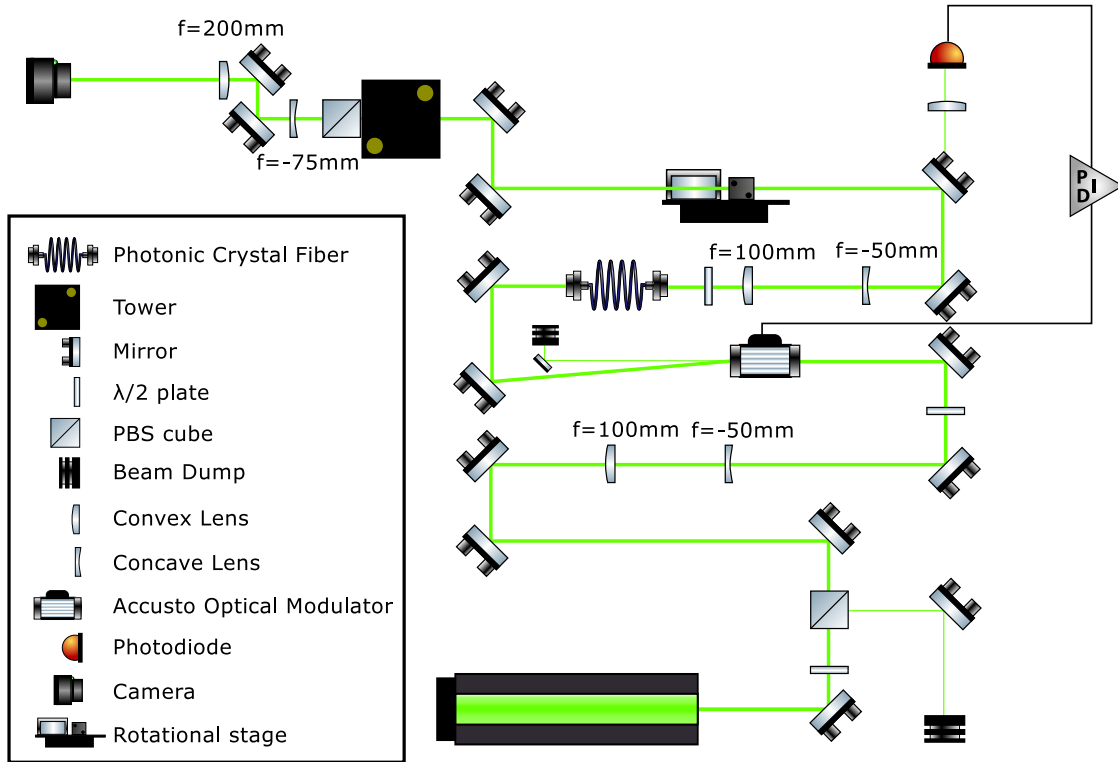
Figure 4.14.: Accordion lattice setup. The laser light is polarization cleaned using a PBS cube and shaped using two telescopes. We use the first order of an AOM which is intensity stabilized using a PID to control the RF signal for the AOM. The beams interfere in the focus point of a lens with $f = 200\,\text{mm}$. The setup used to characterize the lattice did not include the photonic crystal fiber. When implementing the setup in the main experiment, the atoms will be at the position at which the camera was positioned for the characterization. For further information see text.

The final experimental setup used for testing the accordion lattice is shown in Fig. 4.14. We use a Coherent Verdi V18 laser with a maximum output power of 18 W and an output beam waist of 1360 µm. We insert a $\lambda/2$ waveplate and a PBS cube immediately after the laser output port, to be able to reduce the laser power. The intensity of the beam is stabilized using an AOM. Owing to the fact that an aperture has to be $\approx 1.5\times$ larger than the beam diameter to limit the losses to below $1\,\%$, the lasers' output beam waist is slightly too large for the active aperture of the AOM ($3\,\text{mm} \times 6\,\text{mm}$). Consequently, we insert a telescope (consisting of a f=−50 mm and a f=100 mm lens) before the AOM, to decrease the beam waist by a factor of two (1:2 telescope).

A quartz AOM (M115 - FS80L -3), chosen due to its high damage threshold, is used to stabilize the power. We measure the light transmitted by one of the mirrors using a photodiode. This signal is then processed using a sample and hold PID controller, which controls a variable attenuator that alters the amplitude of the RF signal going to the AOM. This allows us to stabilize the power in the first order of the AOM.

The beam is subsequently shaped by another 1:2 telescope to achieve the desired beamshape ($w_\text{y} = w_\text{z} \simeq 337.5\,\mu\text{m}$ (see Section 4.4.3)). The height of the beam is altered using the rotational stage (see Section 4.4.2) before it enters the tower setup. The resulting parallel beams pass through a $f = -75\,\text{mm}$ cylindrical lens and are directed onto the $f = 200\,\text{mm}$ aspherical lens using two mirrors. The final interference pattern is observed using a mvBlueFOX camera,with a microscope objective with tenfold magnification to expand the interference pattern.

4.4.6. Alignment procedure
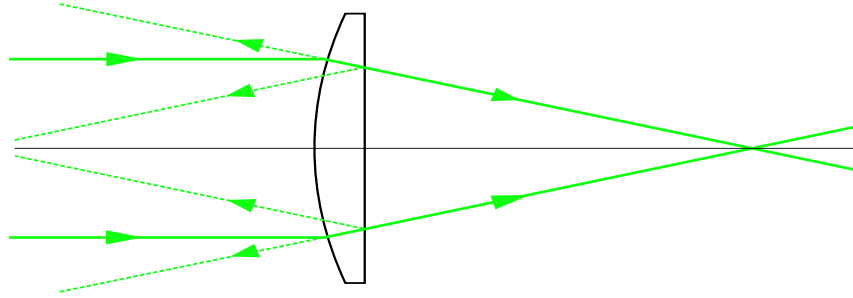
Figure 4.15.: The back reflections of a planoconvex lens. The beams reflected by the plane side of the lens can be used to adjust the tilt of the lens by assuring that they have the same distance to the incoming beams. For further information see text.

The setup shown in Fig. 4.14 was used to optimize and determine the characteristics of the accordion lattice. We aim to minimize the movement of the position of the focal point during the compression, as it can lead to a displacement of the central fringe of the lattice as well as an alteration of the trap depth caused by a change in the overlap of the two beams. The position of the focal point slightly varies when

changing the separation of the two beams. To determine this variation, we measure the vertical position of the individual beams for different separations. The camera is fixed to the focal point (i.e. the point where upper and lower beam have the same vertical position) at a given separation. There are two main effects on the change of the vertical beam position for different beam separations. Firstly, when the mirrors on the rotation stage are not parallel, the outgoing beam is reflected under an angle that is dependent on the angle α between the incoming beam and the mirrors on the rotation stage. Thus the beam direction changes for different α, causing a change of the focal position for different beam separations. Second, the focal position at different separations is influenced by the tilt of the aspherical lens, which changes the vertical position of the upper and lower beam in the focal point. Moreover, the tilt of the lens alters the position of the central fringe when ramping the confinement. We expect this to be due to an alteration in the phase difference of the two beams, caused by a change in the optical path length difference for different beam separations, due to the tilt of the lens. Consequently we have to ensure that the tilt of the aspherical lens is minimized and that the beams exiting the tower are parallel for all beam separations, which is equivalent to ensuring that the direction of the beams remains constant when changing α.

The parallelism of the outgoing beams at different separations was checked without the $f = 200 \, \mathrm{mm}$ lens. First we ensure that the two outgoing beams are parallel for one separation. The mirror on top of the tower was aligned such that the reflected beam coincides with the incoming beam. Second, the last mirror in front of the tower was adjusted such that the outcoming beams are parallel. This was ensured by checking that their separation remains constant at three different positions after the tower. Afterwards we alter the beam separation and verify that the beams are still parallel. If this is not the case, the tilt of mirror M1 on the rotational stage is adjusted. This process is repeated until the beams at the maximum and minimum beam separation are parallel.

A rough adjustment of the tilt of the lens can be made by ensuring that the back reflections of the plain side of the lens (illustrated in Fig. 4.15) are symmetric with respect to the incoming beams. The angle of the reflection by the plain side depends on the angle between the lens and the incoming beam. Thus, by ensuring that the two back reflected beams are in the same distance of the incoming beams for a given distance from the lens, one can roughly adjust the tilt of the lens.

The fine adjustment can be done by looking at the central peak position of the two beams in the focal point. This was done by blocking one of the two beams and recording the position of the other beam on the camera. The camera is fixed at the focal point (i.e. the point where the beams have the same vertical position) for a given beam separation. Due to the fact that the aspherical lens is not perfect, the focal point does not remain constant for different beam separations, leading to a displacement of the beam position relative to the focal point in z-direction for a fixed camera position. When the lens is orthogonal to the incoming beams, the change in the vertical position of the upper and the lower beam for different beam separations is symmetric.

4.5. Characteristics of the accordion lattice

We test the the experimental set-up shown in Fig. 4.14 (without the photonic crystal fiber) offline, observing the lattice using the aforementioned camera. We first characterize the change in beam separation for different angles α (angle between the mirrors on the rotation stage and the incoming beam) and the change in the vertical beam position in the focal point when varying the separation of the beams. Second, we measure the lattice spacing for different beam separations as well as the dynamic stability of the lattice during compression. Furthermore, we measured the temporal stability of the lattice for different laser powers.
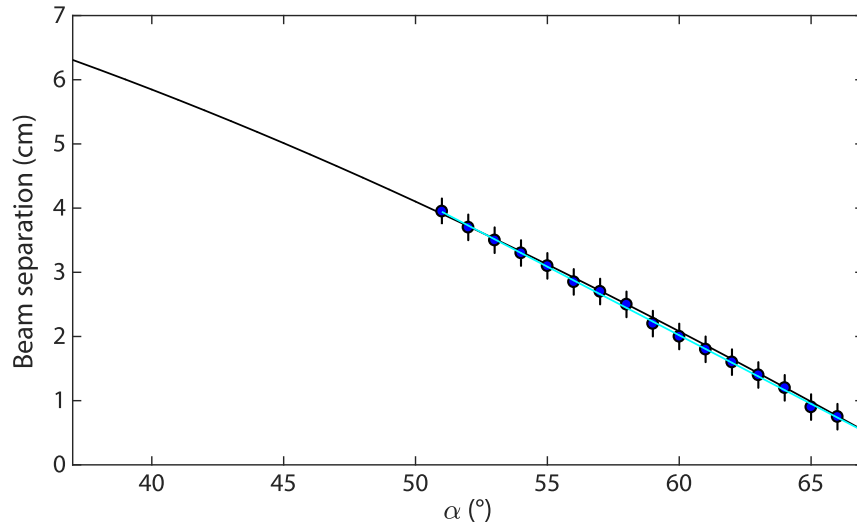
4.5.1. Beam separation

Figure 4.16.: Plot of the beam separations for different angles α. The black line marks the beam separation, for all α where the beam hits both mirrors. The measured data points are marked in blue. A linear fit of the data points is shown in cyan.

We measure the separation of the beams in dependence of the angle α, which is altered in steps of 1°, going from the maximum to the minimum beam separation. The black line shows the beam separation obtained using the analytic calculation (see Appendix A.2), for all α, where the beam is reflected by both mirrors. The experimentally obtained data points are within 1σ of the results of the numerical calculation. The measured data points are approximated using a linear fit function, to obtain a calibration of the beam separation as a function of α. Although the numerically obtained separations do not have a linear dependence on α, a linear fit of the measured points has $\chi_\nu^2 = 0.3211$. As $\chi_\nu^2 < 1$ the model is over fitting the data, meaning that our estimate for the errors is too large. Nonetheless χ_ν^2 is in the 95 % confidence interval, signifying that a linear equation sufficiently describes the dataset

in the region of α used for the experiment. The linear equation used to convert α to the corresponding beam separation is given by

$$D(\alpha) = \alpha \cdot 2.14(2)\,\text{mm}/° + 148(1)\,\text{mm}. \tag{4.14}$$

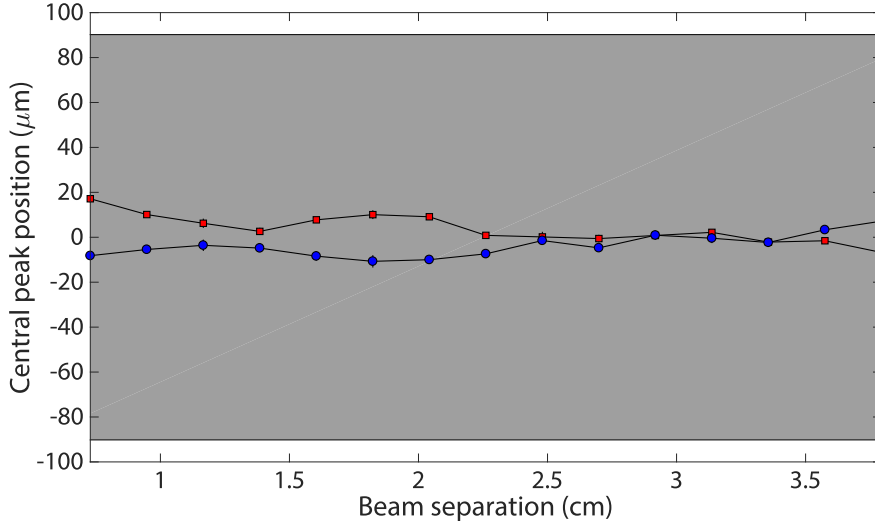## 4.5.2. Vertical beam displacement in focal point

Figure 4.17.: Vertical central peak position of the upper and lower beam (defined according to their relative heights when exiting the tower) in dependence of the beam separation. The red squares (blue dots) show the position of the upper (lower) beam. The displayed points are the mean of three sets of measurements taken successively. The error bars represent the standard error of these three measurements and are smaller than the size of the data points. The lines connecting the data points serve as a guide to the eye. The beam diameter in the vertical direction is indicated by the shaded region.

The setup was aligned as discussed in Subsection 4.4.6. We observe the change of the individual vertical beam positions in the focal point when varying the separation of the beams, to ensure that their overlap does not change significantly when altering the confinement of the lattice. This is important as a variation in the trap depth could induce heating. We block one of the beams and measure the vertical position of the other beam. The position of the camera is fixed at the point where the beams have the same central peak position for a separation of $3\,\text{cm}$. A central cut through the obtained image was fit with a Gaussian function to obtain the central peak position in the vertical direction. Figure 4.17 shows the resulting data. The vertical position of the beams changes by a maximum of $24\,\mu\text{m}$. As this shift is small compared to the individual beam waist of $w_z = 90\,\mu\text{m}$ (indicated by the shaded area in the plot), the overlap of the two beams does not alter significantly during the compression. The central fringe intensity changes by $\approx 2\,\%$ during the compression,

owing to the change in the overlap. Comparing our results to those specified by Ville et al. [65] shows that the displacement of the beams ($\approx 20\,\mu$m) specified in the paper is roughly the same as the displacement that we measured. As we use a larger beam waist, the variation of the trap depth will be smaller than that observed in [65].
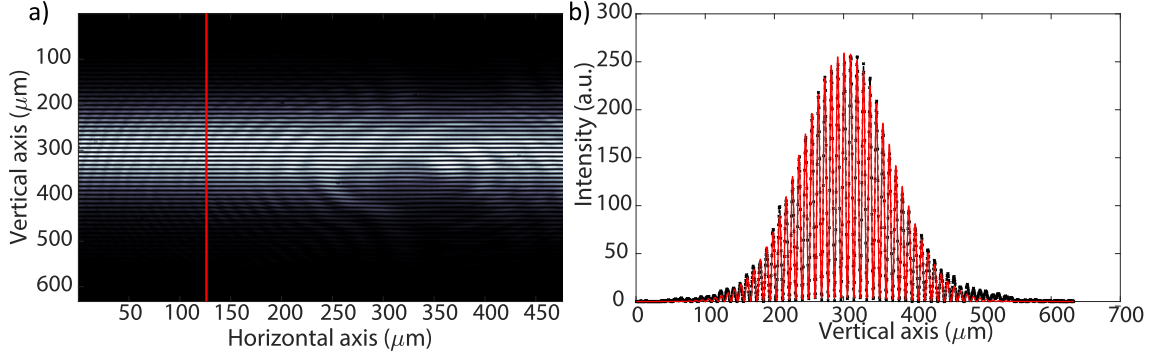
4.5.3. Fitting Routine

Figure 4.18.: Raw picture and cut of the lattice, obtained at a beam separation $D = 11\,$mm. Subfigure a shows the raw picture obtained using a mvBlueFox camera with a microscope objective (tenfold magnification). The red line marks a cut through the picture. The cut was chosen to be off-centre, due to the aberrations (caused by dust on the camera or objective) at the centre. Subfigure b) shows the intensity pattern of this central cut (displayed in black), approximated using function Eq.4.15 (shown in red).

An exemplary picture of the lattice is shown in Fig. 4.18a. The lattice was evaluated by fitting a central cut of the interference pattern with the function

$$ y(x) = A \cdot \sin\left(2\pi\left(\frac{x-o}{p}+d\right)\right) \cdot \exp\left(-\frac{x-c}{e}\right)^2, \tag{4.15} $$

which is the convolution of a sinusoidal and a Gaussian function. The parameter A gives the amplitude, o is a constant offset, p is the period of the lattice and d is the phase of the sinusoidal. The parameter c gives the central position of the Gaussian and e describes the width of the Gaussian. The intensity pattern of such an individual row, including the fit is shown in Fig. 4.18b.

4.5.4. Lattice spacing

The fit parameter p gives the lattice spacing. As the accuracy of the fit function is strongly dependent on the starting value chosen for p, we programmed a peak-finder, that determines the maxima in the signal by comparing the intensity at a given pixel to that of the neighbouring pixels. The mean distance between adjacent maxima is used as a starting value for p. The measured lattice spacing in dependence of the beam separation is shown in Fig. 4.19. We approximate the curve using Eq. (4.9),
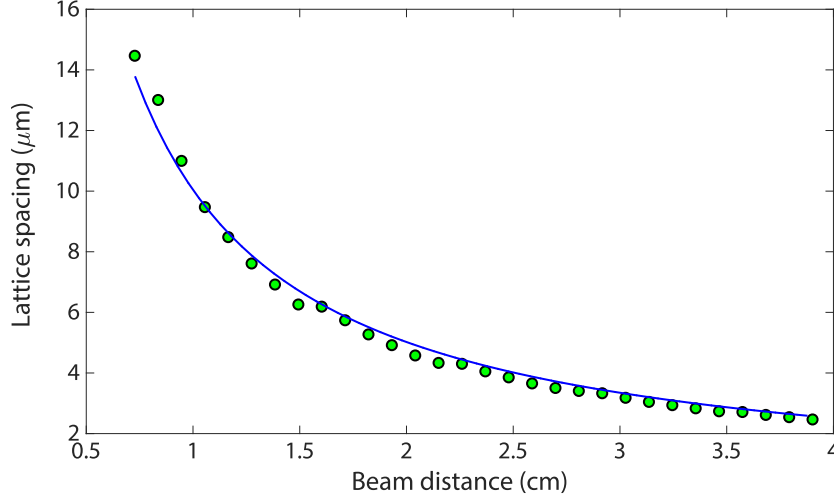
Figure 4.19.: Lattice spacing in dependence of beam separation. The green data points mark the mean of three subsequent measurements. The error bars are smaller than the symbol size. The blue curve marks a fit with Eq. (4.9) to the data points.

giving a focal length $f = 192(4)\,\text{mm}$, which is within 2σ of the focal length specified by the manufacturer ($f = 200\,\text{mm}$).

4.5.5. Dynamic stability

The movement of the central lattice fringe is vital for the performance of the accordion lattice. Changes in the central fringe position during compression could lead to unwanted heating effects. In addition to this, the atoms might move out of the focus of the imaging objective during the compression when the central fringe position changes too much. We measure the displacement of the central beam by taking a picture of the lattice for different beam separations (changing the angle α in steps of 1°). The camera is placed at a fixed distance from the lens. We visualize the movement of the central fringe, by cutting an area with a width of 15 pixels from the centre of each picture and putting them after each other. The resulting picture is shown in Fig. 4.20a. We determine the maximum of the central fringe using a Gaussian fit, limited to a small region around the central peak. The obtained central peak positions are represented by the black dots. Figure 4.20b shows a zoom-in on the central peak positions. The y-axis is shifted such that the central peak position at the highest beam separation is equal to zero. The limits of the y-axis reflect the depth of focus of the vertical imaging objective ($\simeq \pm 3\,\mu\text{m}$), given that its focal point is at the position of the central fringe for the maximum beam separation. The central peak moves by $1.6(1)\,\mu\text{m}$ during the compression (see Fig. 4.20b). This movement stems from residual imperfections in the alignment (e.g. tilt of the lens, parallelism of mirrors on rotation stage). As can be seen in Fig. 4.20b, the position of the central peak stays safely within the depth of focus of the vertical imaging objective.
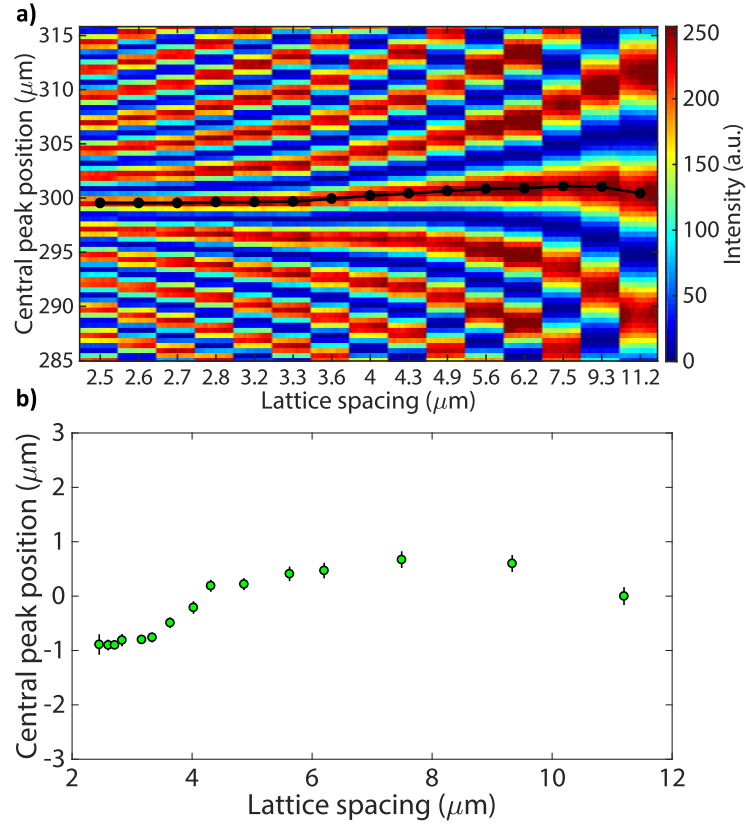
Figure 4.20.: Dynamic stability of the lattice. Subfigure a) shows cuts of the central interference pattern with a width of 15px put after each other. The black data points mark the centre of a Gaussian fit with which the central peak was approximated. The error bars are smaller than the symbol size. The line serves as a guide to the eye. A zoom-in on these positions is shown in b). The y-axis is shifted such that the central peak position at the highest beam separation is at zero. The limits of the y-axis reflect the depth of focus of the imaging objective ($\simeq \pm 3\,\mu$m). The error bars are obtained from the fit of the central fringe with a Gaussian function.

4.5.6. Temporal stability

In addition to the shift of the central peak position during compression, the position of the central fringe is dependent on the stability of the phase of the interference pattern. This phase is characterized by the parameter d in Eq. (4.15). To be able to determine d, we introduce a constant offset o into the equation, which is manually chosen to be at the centre of the lattice. This offset provides a constant reference point for the phase.

The phase of the lattice is determined by the phase difference of the two beams. The beams have a path difference of $L =111\,$mm in the tower, as the upper beam passes through the second cube and wave plate twice. Outside the tower, the beam-paths are symmetric around the optical axis of the lens. While it is important to shield this part from external influences (e.g. air currents), we assume that the

change in the phase of the beams occurs mainly in the tower. The change in phase of the upper laser beam relative to the lower one is given by Φ, where

$$\Phi = \frac{2\pi}{\lambda}L. \tag{4.16}$$

A change in Φ can thus occur when either λ or L changes. A change in Φ, which is difficult to observe with our experimental setup, will cause a change in the phase of the lattice d, which we directly obtain from a fit of the interference pattern using Eg. (4.15).

We evaluate the stability of the lattice by observing the change in d over time. The first measurement was performed at low power ($P < 0.1\,\mathrm{W}$), directly after switching on the laser. A plot of the phase of the lattice is shown in the inset in Fig. 4.21. Multiple phase jumps occurred during the measurement. We speculate that these jumps stem from frequency jumps i.e. mode hops of the laser during the heat-up period, leading to a change in Φ, caused by a slight change in λ. The change in frequency necessary for one of those phase jumps can be calculated using Eq. (4.16). The average change in the lattice phase is equal to $0.43(3) \cdot 2\pi$ corresponding to a frequency difference of $1.16(8)\,\mathrm{GHz}$.
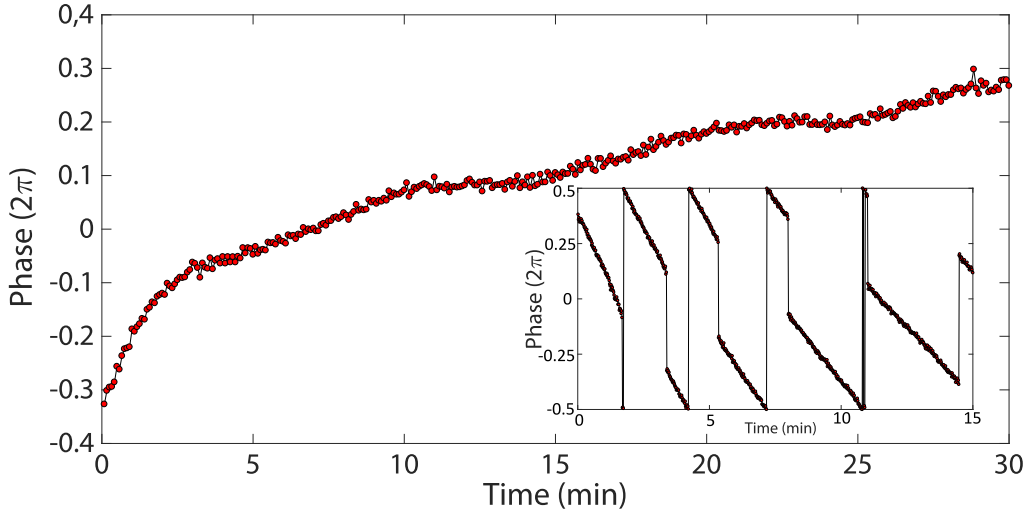
Figure 4.21.: Phase of the lattice measured at low laser power ($P < 0.1\,\mathrm{W}$) after a heat-up period (2.5 h). The inset shows the phase of the lattice measured directly after turning on the laser. The data points are marked in red, the line serves as a guide to the eye.

We repeat the measurement after a heat-up period (2.5 h). During the heat-up period, the laser is blocked immediately after the output port, to ensure that the phase jumps are not caused by another element with a non-linear thermal behaviour. The results are plotted in Fig. 4.21. As no jumps occur after the heat up period, we assume that the phase-jumps are caused by mode-hops occurring while the laser is not at thermal equilibrium. The change in phase is getting smaller over time, consequently we can speculate that it is caused by a thermal expansion of the tower,

leading to a change in L, which decreases as thermal equilibrium is approached. However, the influence of a change in λ on Φ must not be overlooked, especially for experiments requiring a high stability of the lattice. Here it might be advisable to lock the laser to an external reference.

We repeat the measurement at higher laser powers after a heat-up period. During the measurement we rapidly change the power from 0.5 W to 4.5 W, to observe the influence of the laser power on the stability. We change the power by altering the RF power of the AOM signal. This ensures that the laser can remain at a high output power, so that the shifts are not caused by fluctuations in the frequency which we observed when the laser is not at thermal equilibrium. Figure 4.22 shows the stability of the interference pattern over time at high laser powers. We observe a change in phase per time $\Delta p = 2\pi \cdot 0.0016(1)/\text{s}$ at 4.5 W, which is a factor of 2 larger than the change at 0.5 W ($\Delta p = 2\pi \cdot 0.0008(1)/\text{s}$).

Such a behaviour could be explained by an increase in the temperature of the tower caused by stray light. To obtain the change in path length due to an increase in temperature, we calculate the thermal expansion of the aluminium housing. The linear thermal expansion coefficient of Aluminium $c = 24 \cdot 10^{-6} \, 1/\text{K}$. Consequently the path difference ($L = 111\,\text{mm}$) changes by 2.64 µm/K. A change in temperature of 0.2 K will thus alter the path length difference by one wavelength ($\lambda = 532\,\text{nm}$), leading to a phase change of 2π. The energy E needed to change the temperature of Aluminium with mass m by a temperature difference T is given by

$$E = cmT, \tag{4.17}$$

where $c = 0.9\,\text{kJ}/(\text{kg}\,\text{K})$ is the specific heat capacity of aluminium. For our estimate we use $m = 200\,\text{g}$ which corresponds to the mass of a single aluminium plate. This estimate is justified as the tower consists of anodized aluminium plates that are screwed to each other, leading to a relatively weak thermal contact between them. The change in phase per time Δp at 4.5 W ($\Delta p = 2\pi \cdot 0.0016(1)/\text{s}$) can be caused by stray light with a total power of $P \approx 60\,\text{mW}$ which corresponds to 1.33 % of the initial power. While this percentage is higher than expected (the transmission of the top mirror was measured to be 0.3(1) %), we can still assume that the change in phase is at least partially caused by heating due to stray light.

This drift could be minimized by a better thermal contacting of the individual aluminium plates that make up the tower. At the same stray power, the change in phase per unit time would decrease by a factor of 5 for the perfectly thermally contacted tower. Another possibility would be to stabilize the temperature of the tower. Even though the power used during the experimental sequence is 4.5 W, the average power will be below that, due to the fact that the laser is only turned for a short time during the experimental sequence. Therefore, the drift during one experimental cycle should be negligible. Nonetheless we need to be able to control the phase of the lattice.
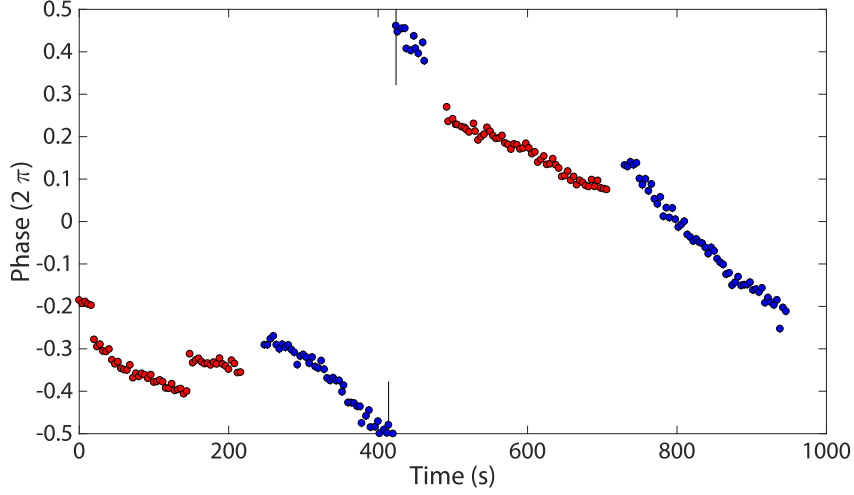
Figure 4.22.: Phase of the lattice over time. The red dots mark the data acquired at a laser power $P = 0.5\,\mathrm{W}$ at the focus position, the blue dots mark the data acquired at $P = 4.5\,\mathrm{W}$. The error bars are obtained from the uncertainty of the fit of the individual interference patterns.

4.6. Experimental control

We need to be able to control the phase of the lattice, in order to repeat the experiment in a controlled manner. This is done by actively changing the path length difference L using a piezo stack placed under the top mirror in the tower. We use a Round PICMA® Chip Actuator from Physical Instruments (PD160.3x), with a travel range of $2.2\,\mu\mathrm{m}$ at $0\,\mathrm{V}$ to $100\,\mathrm{V}$. This allows us to change path difference by a single wavelength ($\lambda = 532\,\mathrm{nm}$), which results in a change of phase of 2π, while operating the piezo in the range of $0\,\mathrm{V}$ to $24\,\mathrm{V}$, which is provided by a standard lab power supply. We measure the interference pattern for different piezo voltages. The resulting plot of the phase as a function of the piezo voltage is shown in Fig. 4.23.

We did not implement the long term phase stabilization during the course of this thesis. The proposed sequence for stabilization the phase is to measure the phase at a given lattice separation before the experimental sequence. This information is used to adjust the piezo voltage so that the phase is set to a fixed value. The piezo voltage is then kept constant during the experimental sequence.

The phase of the lattice can be measured by recording the interference pattern onto a camera and obtaining the phase using the same fitting routine used for the stability measurements. Naturally we cannot place the camera at the position of the atoms. One possibility would be to record the interference pattern of the back reflections of the viewports. This is possible as we enter the viewport under an angle, meaning that the back reflections do not coincide with the incoming beams. Nonetheless this can be challenging due to space constraints in the experimental setup. Another possibility would be to use the beams that are reflected by the two cubes used to
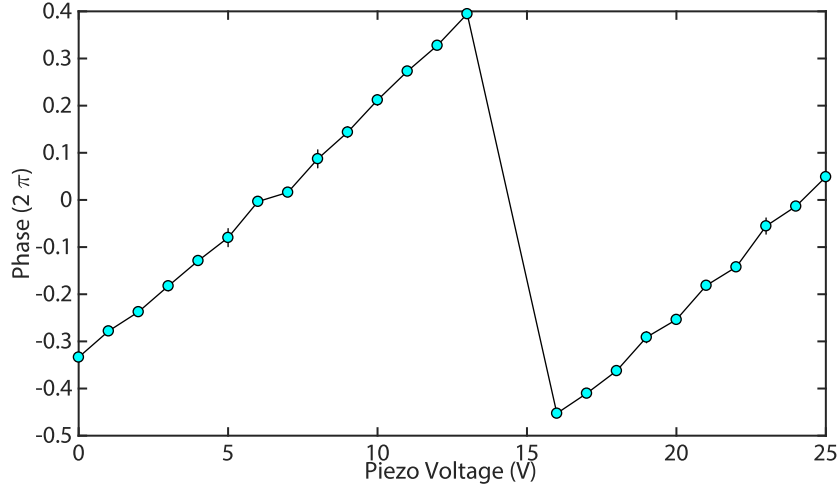
Figure 4.23.: Lattice phase as a function of the piezo voltage. The data points represent the mean of 3 subsequent measurements. The error bars represent the standard error of these measurements. The line serves as a guide to the eye.

clean the polarization of the beams and letting them interfere in the focal point of a lens. This lens must not necessarily be aspheric as only one beam separation is used. Even though the beams reflected by the cubes do not have exactly the same polarization, the contrast should still be high enough to observe the interference pattern. As the cubes are farther away from the vacuum chamber, there is more available space to insert the lens and camera. The drawback of this proposal is that the change in phase difference after the cubes can not be observed. Although the change in phase difference after the tower is expected to be much smaller than that in the tower, this reduces the quality of the stabilization. The third possibility is to directly image the lattice onto a camera by placing a lens on the other side of the vacuum chamber. This method is again constrained by the space we have in the experiment, but should account for all drifts in the phase difference. Nonetheless it is possible that the beams acquire an additional phase difference in between the atoms and the camera. This would lead to a stabilization to an incorrect phase.

5. Variable blue detuned potential

We aim to implement a blue detuned, variable potential, directed onto the atoms along the vertical (z-)axis, to create vortex excitations. We choose the wavelength $\lambda = 370\,\text{nm}$, which is blue detuned for both Erbium and Dysprosium (see Section 2.2). The spatial intensity profile of the laser beam is modulated using a digital micromirror device (DMD) and projected onto the atoms via the vertical imaging objective, creating a variable blue detuned potential. This potential provides both the in-plane confinement and the possibility to introduce rotation as well as moving obstacles into the system. During the course of this thesis we planned the optical setup and optimized it using Zemax OpticStudio.

5.1. Digital Micromirror Device

The digital micromirror device (DMD) consists of an array of individually addressable mirrors. We utilize a Texas Instruments DLP9500 consisting of 1920x1080 mirrors with a size of $10.8\,\mu\text{m}$ and a maximum pattern rate of $23\,148\,\text{Hz}$.

A pattern can be displayed on the DMD by changing the tilt of the individual micromirrors. The mirrors of the DMD have three possible states: ON, IDLE and OFF. When the DMD is turned off, the mirrors are in the IDLE state, meaning that they are parallel to the plane at which they are mounted. In the ON and OFF configuration the mirrors are tilted by $\pm 12°$ relative to the IDLE state. When light is send onto the DMD, it is reflected by the micromirror array, under an angle given by the tilt of the individual mirrors. This is used to selectively 'cut out' parts of the laser beam and thus modulate its spatial intensity profile.

The array of individually tilted micromirrors can be seen as a blazed grating with a spacing d equal to the micromirror spacing. This is illustrated in Fig. 5.1. The relationship between the angle α and the angle β can be expressed by the grating equation

$$m\lambda = d\left(\sin\alpha + \sin\beta\right), \tag{5.1}$$

where $m \in \mathbb{Z}$ is the diffraction order. The grating equation can be fulfilled for any value of m for which

$$-2d < m\lambda < 2d. \tag{5.2}$$

Thus, multiple diffraction orders exist. [68] As only a single order is used for spatial light modulation, the diffraction efficiency (i.e. ratio of the power in the zeroth order to the total power) is an important parameter governing the total efficiency of the DMD.

The diffraction efficiency can be maximized by satisfying the blaze condition

$$m\lambda = 2d\sin\theta_{\mathrm{B}}, \tag{5.3}$$

where θ_{B} is the tilt of the mirrors. When this condition is satisfied, the incident and diffracted ray behave according to the law of reflection, when viewed from the facet of the mirrors [68]. This is to say that

$$\alpha - \theta_{\mathrm{B}} = \beta - \theta_{\mathrm{B}}. \tag{5.4}$$

We use equations (5.1) and (5.3) to calculate the angle of incidence α, for which the outgoing beam exits perpendicular to the DMD ($\beta = 0°$). This condition yields $\alpha = 24.57°$. For mirrors in the OFF state ($\theta_{\mathrm{B}} = -12°$), the beam exits in an angle $\beta_{\mathrm{OFF}} = -56.27°$. The idle DMD behaves as a mirror with $\beta_{\mathrm{IDLE}} = -\alpha = -24.57°$. This allows us to separate the beams, letting only the light reflected by the mirrors in the ON state pass on to the experimental setup, while light reflected by the mirrors in the OFF and IDLE state is blocked.

The efficiency of the DMD is limited by several factors. As discussed above, multiple diffraction orders exist, leading to a decrease in the usable power as only a single order is used. Moreover the efficiency is limited by the array fill factor (the ratio of the area of all individual micromirrors to the total area of the micromirror array), the transmission of the window in front of the micromirror array as well as the reflectivity of the micromirrors. All of these factors lead to a nominal diffraction efficiency of 70 % when all mirrors are in the ON state. The power is decreased further when switching mirrors to the OFF-state.
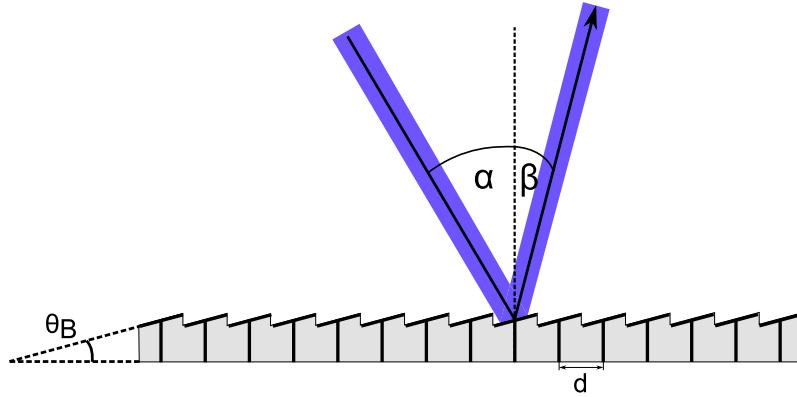

Figure 5.1.: Illustration of the reflection by the mirrors of the DMD. The individually tilted mirrors make up a blazed grating with spacing d and grating angle θ_{B}.

5.2. Optical setup

We aim to implement the DMD such that the pattern displayed on the DMD is directly imaged onto the atoms. We illuminate the DMD with a laser beam operating

at a wavelength of $\lambda = 370\,\text{nm}$, which is blue detuned for both Er and Dy. At $370\,\text{nm}$ the calculated atomic polarizability is $1200\,\text{a.u.}$ for Er, while the polarizability of Dy is unknown. We are planning to use a diode laser with a power of $\approx 30\,\text{mW}$ to generate the light at $370\,\text{nm}$.

The first step in designing the optical setup for imprinting the DMD pattern onto the atoms, was choosing the diameter of the incoming beam and the demagnification. The field of view covered by the DMD should be large allowing us to vary the size of the trap. We aim to have an incoming beam waist of $3.6\,\text{mm}$ and a demagnifaction factor of 28.82, allowing us to cover a field of view with a waist of $125\,\mu\text{m}$.

We aim to achieve the demagnification factor of 28.82 using a combination of two telescopes, similar to the setup described by Gauthier et al. [69]. This allows us to use commercially available lenses instead of a single telescope consisting of a lens with $f = 1875\,\text{mm}$ and the vertical imaging objective with $f = 65\,\text{mm}$. An intermediate image of the pattern on the DMD with a magnification factor of 0.4 is created using a telescope consisting of a $f = 250\,\text{mm}$ and a $f = 100\,\text{mm}$ lens. The pattern is then imaged onto the atomic plane by a telescope consisting of a $f = 750\,\text{mm}$ lens and the vertical imaging objective with $f = 65\,\text{mm}$, resulting in the total desired demagnification factor.

5.2.1. Optimization of optical setup with Zemax OpticStudio

The optical setup needs to fulfil two criteria. On the one hand, a collimated beam that is reflected by the DMD should result in a collimated beam on the atoms (see Fig. 5.2, beams displayed in blue), to obtain the desired demagnification of the beam. This can be achieved by optimizing the distance between the two lenses making up a telescope (Δ_{T1} and Δ_{T2}). On the other hand, a single point on the DMD should be imaged onto a single point on the atomic plane, to achieve the highest possible resolution. A focused beam emerging from the DMD plane should thus result into a focused beam on the atomic plane (see Fig. 5.2, beams displayed in red). We ensure this by optimizing the distance between the DMD and the first telescope (Δ_{DMD}) as well as the distance between the first and the second telescope (Δ_1) using Zemax OpticStudio.

We simulate the optical setup, including the dichroic mirror placed in a $45°$ angle (used to separate the imaging light ($401\,\text{nm}$ and $421\,\text{nm}$) from the dipole trap ($1064\,\text{nm}$)) using Zemax OpticStudio. The afocal image space is used to optimize the demagnification of the beam. We optimize the distances Δ_{T1} and Δ_{T2} such that the diameter of the outgoing beam at three different points around the plane of the atoms is equal to the expected beam diameter after the demagnification. The optimization at three different points ensures the collimation of the beam.

The imaging of a single point on the DMD onto the atomic plane was optimized by minimizing the radial spot size at the desired focal point. Here it is important to note that the microscope objective was not designed for a wavelength of $370\,\text{nm}$. The focal point of the objective at the design wavelengths ($\lambda = 401\,\text{nm}$ and $\lambda = 421\,\text{nm}$) will not be at the same distance from the objective as the focal point at $370\,\text{nm}$. We
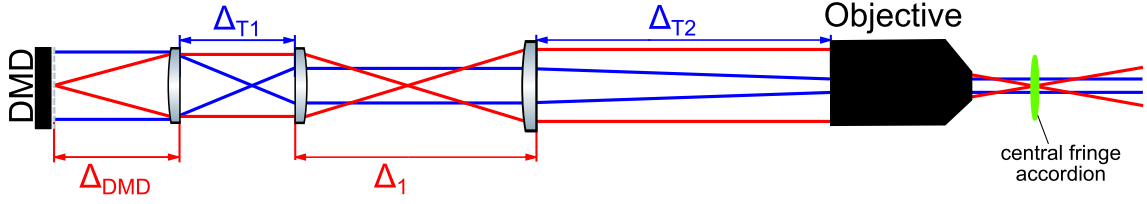
Figure 5.2.: Illustration of the DMD projection system. The beam illustrated in blue shows the demagnification of a collimated beam by the optical setup. The red beam shows the imaging of the DMD plane onto the atomic plane. The distances Δ that have to be optimized for the demagnification of a collimated beam are illustrated in blue, the distances that are optimized for the optimum resolution are displayed in red. The central fringe of the accordion lattice (i.e. the atomic plane) is shown in green. Image not to scale.

can compensate for this by having a slightly focused beam before the objective. Thus Δ_1 is chosen such that the focal point at $370\,\mathrm{nm}$ is at the same position as the one for the design wavelengths. This is important as it allows us to create vortices in the focal point of the imaging light. The dichroic beam splitter results in a different focus position for the x- and y- direction. Consequently we optimized the system such that the total radial size is minimized at the position of the atoms. This optimization yields $\Delta_{\mathrm{DMD}} = 256\,\mathrm{mm}$, $\Delta_{\mathrm{T1}} = 328\,\mathrm{mm}$, $\Delta_1 = 1213\,\mathrm{mm}$ and $\Delta_{\mathrm{T2}} = 806\,\mathrm{mm}$.

According to the demagnification factor of the imaging system, the image of a single mirror of the DMD, which has a width and height of $10.8\,\mathrm{\mu m}$ would have a width/height of $347.8\,\mathrm{nm}$ on the atoms. This exceeds the theoretical resolution limit of the objective ($587.4\,\mathrm{nm}$ Airy disk radius at $370\,\mathrm{nm}$). Consequently the image of a single mirror on the atomic plane approximates the point spread function (PSF) of the optical setup. The theoretical Huygens PSF cross section of the optical setup (2 telescopes + dichroic) along the x- and y-direction is displayed in Fig. 5.3. The calculated airy disk radius is $1.457\,\mathrm{\mu m}$, which is increased greatly by the dichroic beam splitter mounted in an angle of $45°$. Back propagating this value through the optical setup gives a spot size of $41.98\,\mathrm{\mu m}$ at the DMD, resulting in blocks of roughly 4x4 mirrors contributing to one single spot at the atomic plane. Thus the intensity can be altered by turning a certain number of micromirrors contributing to the same point to the OFF state and we can achieve ≈ 16 different intensity levels. Note that the point spread function only provides a lower estimate of the final resolution as it does not take all aberrations present in the real system into account.

The planned optical setup is shown in Fig. 5.4. A half-wave plate and a PBS cube are placed immediately after the output port of the laser, to be able to manually control the power. The beam is intensity stabilized with an AOM and mode cleaned using a polarization maintaining single mode fiber. The intensity stabilization is achieved with a PID (for detailed description see Subsection 4.4.5). Subsequently, the beam is collimated with a FC M40L fiber coupler from Schäfter Kirchhoff, giving us the desired beam waist of $3.6\,\mathrm{mm}$. We insert a half- and a quarter-waveplate in front of the DMD to have full control over the polarization. The beam is directed onto the DMD in an angle of $24.57°$, so that the ON beam exits perpendicular to
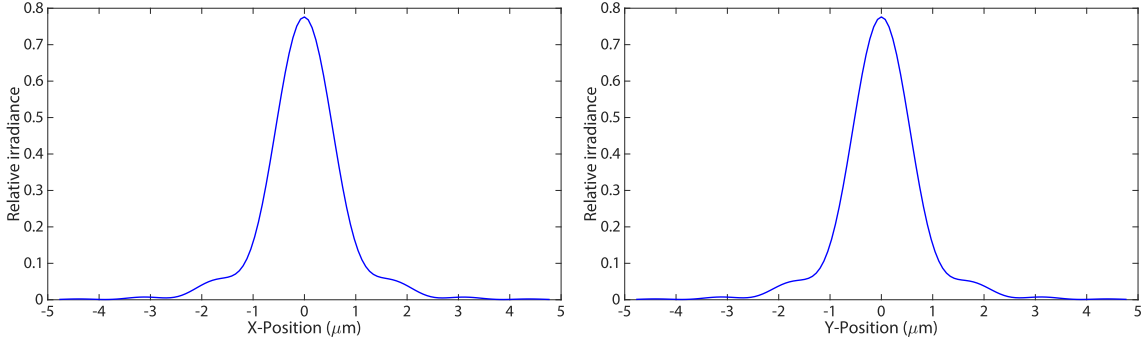
Figure 5.3.: Huygens PSF along the x and y axis of the optical setup calculated with Zemax OpticStudio.

the micromirror array. The ON beam is imaged onto the atomic plane using the described optical setup.

There are several limiting factors in this optical setup. The diode laser has a power of 30 mW. The quartz AOM used for the intensity stabilization has a diffraction efficiency of $\approx 85\,\%$ and the single mode fiber used for mode cleaning has a coupling efficiency of $\approx 90\,\%$. The light is then modulated by the DMD which has a nominal diffraction efficiency of $70\,\%$ (see Section 5.1). To enter the vertical imaging objective, the beam is transmitted through a dichroic mirror, which is used to separate the imaging light (at 401 nm and 412 nm) from the optical dipole trap light (1064 nm). At 370 nm, $88(1)\,\%$ are transmitted through the dichroic mirror. The vertical imaging objective has a transmission of $\approx 78(1)\,\%$ and the viewport of the vacuum chamber has a transmission of $82(1)\,\%$. As these transmissions were not specified by the manufacturer, we determined them experimentally.

5.3. Alignment strategy

The theoretical distances are only a rough guideline for the real optical setup, owing to fabrication tolerances. In addition to this, the correct adjustment according to theoretical distances is difficult to achieve. Consequently we planned a strategy to adjust the individual lenses relative to each other.

The DMD has to be placed in the focal point of the first lens. The optical setup used to adjust this is illustrated in Fig. 5.5 (1). The beam is focused onto the IDLE DMD with the first lens. As the DMD is IDLE, the reflected beam exits perpendicular to the micromirror array and is separated from the incoming light by a beam splitter cube. When Δ_{DMD} equates the focal length of the lens, the reflected beam is collimated.

A focused beam on the DMD is required to align the distance between the two telescopes (Δ_2). Thus another lens is inserted in front of the DMD (see Fig. 5.5 (2)). This lens is mounted on a flip mount, allowing us to direct both a collimated and a focused beam onto the DMD. To place the lens in the correct distance Δ from
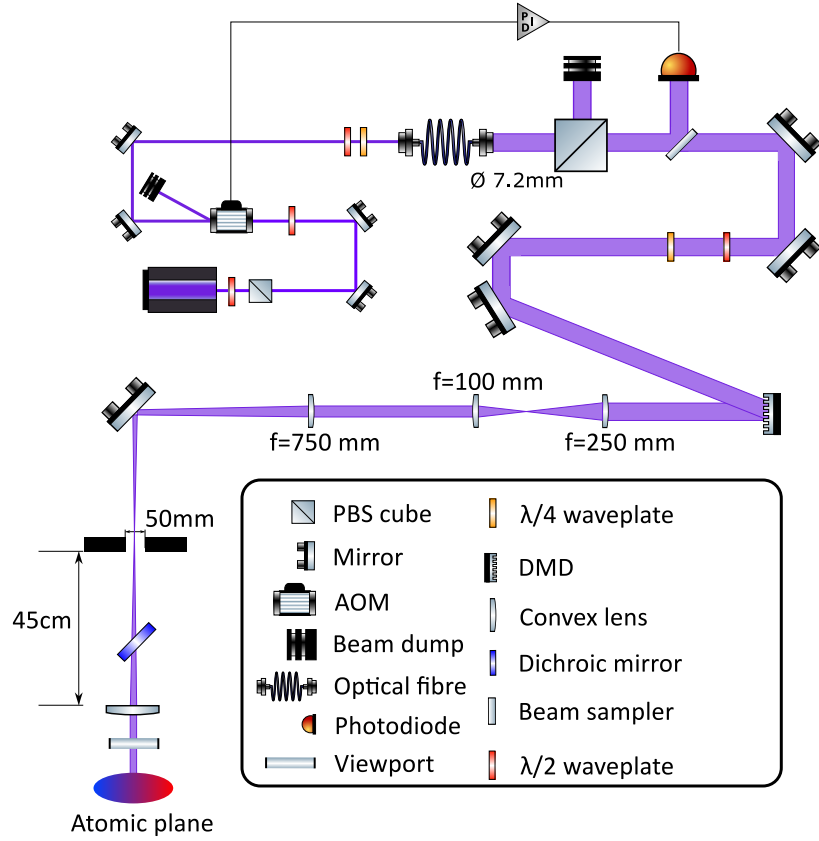
71

Figure 5.4.: Sketch of the experimental setup used to project the pattern displayed on the DMD onto the atomic plane. The polarization of the laser light is cleaned with a PBS cube and intensity stabilized using an AOM. It is then coupled into a single mode polarization maintaining fiber. We use a FC M40L fiber coupler to achieve a waist of 3.6 mm after the fiber. The beam is directed onto the DMD to modulate its spatial intensity pattern and is then imaged onto the atomic plane with two telescopes. For further information see text.

the DMD, all micromirrors are turned to the ON state. The incoming beam enters perpendicular to the DMD and is reflected under 24.57°. The distance Δ is chosen such that the beam is collimated after the lens.

The setup used to align Δ_{T1} is shown in Fig. 5.5 (3). A collimated beam is directed onto the DMD under an angle of 24.57°. The distance Δ_{T1} is altered to achieve a collimated beam after the second lens. To align Δ_1, the lens inserted in step 2) is used to focus the beam onto the DMD. The distance Δ_1 is chosen such that the beam is collimated after the third lens. The third lens should be mounted on a linear translation stage to be able to change Δ_1, so that the beam can be slightly focused afterwards to compensate for the different focal length of the objective at 370 nm.

An optical setup that allows to change Δ_1 and Δ_{T2} independently is vital to ensure that a collimated incoming beam is collimated at the position of the atoms and that the focal point at 370 nm coincides with the focal point at the imaging wavelengths. This could for example be done by inserting a mirror on a linear translation stage

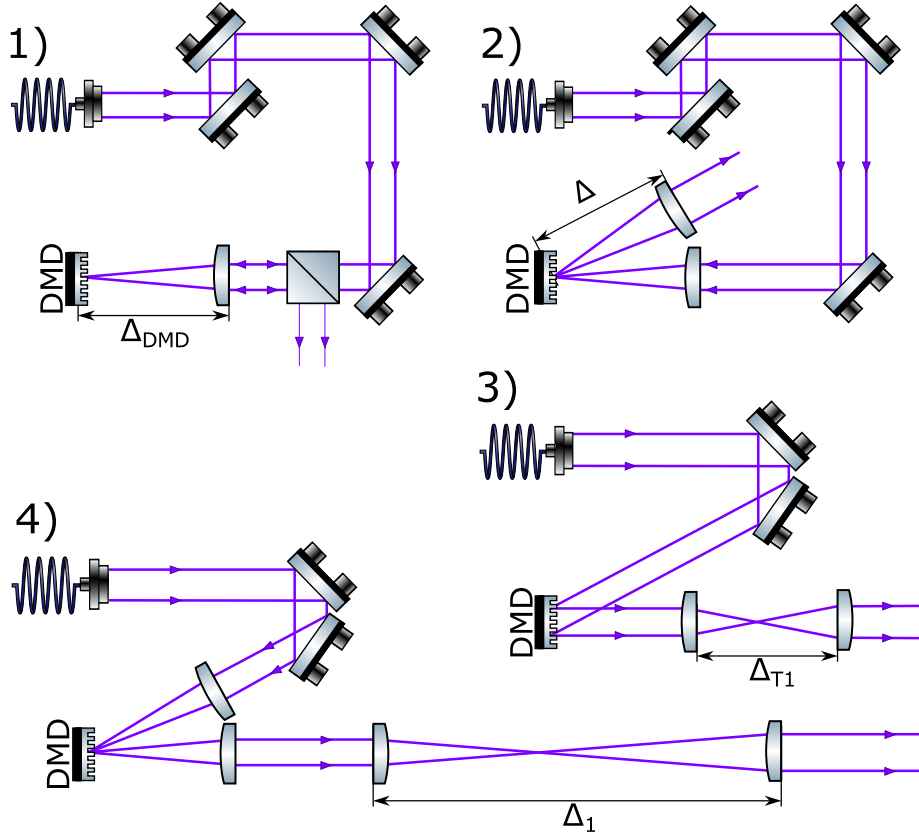between the objective and the last lens to be able to alter Δ_{T2}.

Figure 5.5.: Experimental setups used to align the two telescopes imaging the pattern displayed on the DMD onto the atoms.

5.4. Application

The planned optical setup can be used to create a variable blue-detuned potential, which can provide both in-plane confinement and can be used to create vortices. The versatility of the DMD allows the creation of vortices via both the rotating-bucket and the optical-spoon approach (see Section 3.5). The DMD is used to selectively 'cut-out' part of the incoming blue detuned Gaussian beam, by setting the mirrors within a circle to the OFF position, setting the intensity in this region to zero, hence resulting in a flat bottom potential. This process is illustrated in Fig. 5.6. The intensity profiles were calculated using the code in Appendix A.3. The image displayed on the DMD is shown in Fig. 5.6a. Here all mirrors within a circle with a radius of 1.5 mm at the centre of the DMD are turned to the OFF position. The intensity profile of the incoming Gaussian beam is shown in Fig. 5.6b. The DMD removes the central part of the Gaussian beam (see Fig. 5.6c), significantly reducing the maximum intensity. Projecting this beam onto the atomic plane with the described

optical setup leads to a potential with a trap depth of 165 nK on the atoms (see Fig. 5.6d) . A radius of 1.5 mm on the DMD was chosen for illustrative purposes.
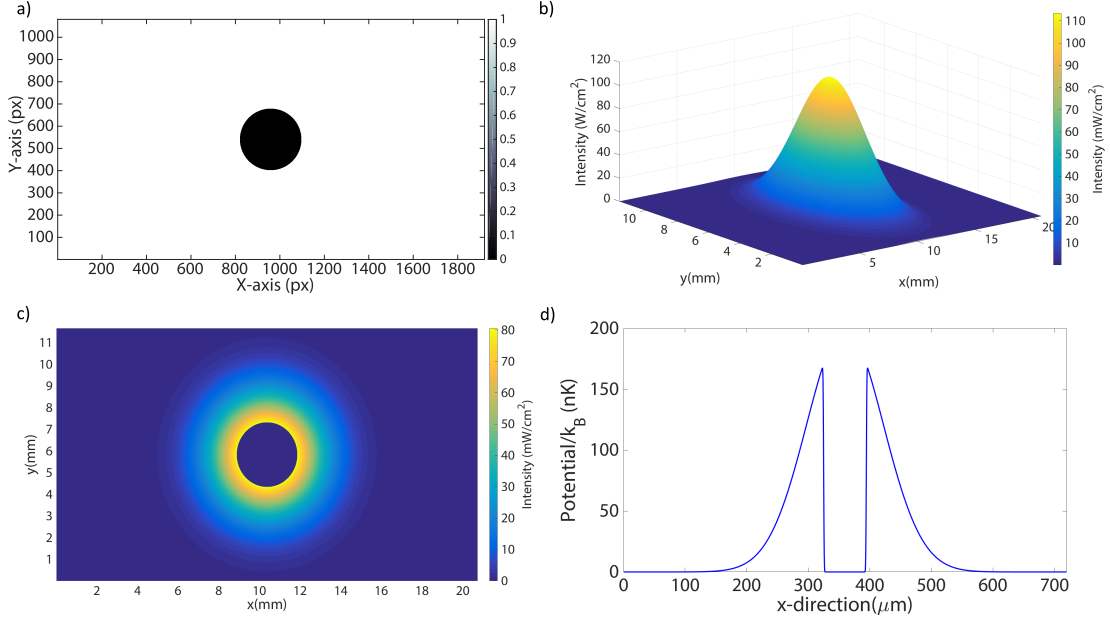

Figure 5.6.: Illustration of the simulation of the creation of a flat bottom trap using a DMD. Subfigure a) shows the image displayed on the DMD, where the mirrors in the ON (OFF) position are shown in white(black). The intensity profile of the incoming gaussian beam is shown in Subfigure b). The central part of the beam is removed by the DMD, with the resulting intensity profile shown in c). Subfigure d) shows a central cut of the calculated potential on the atoms.

As discussed in Section 4.1, the radial confinement of the accordion lattice ($\approx 2\pi \cdot 5\,\mathrm{Hz}$) is not high enough to trap the BEC. Thus the confinement has to be provided by an additional potential. The proposed experimental sequence is to first evaporate in a crossed beam optical dipole trap [24]. After evaporative cooling, the accordion lattice is turned on at the maximum lattice spacing, while the dipole trap remains on to provide the in-plane confinement, resulting in trapping frequencies of $(\omega_x, \omega_y, \omega_z) = 2\pi \cdot (50, 30, 422)\mathrm{Hz}$. The variable blue detuned potential is turned on while the power of the dipole trap is decreased, loading the atoms in the blue detuned potential with trap frequencies $(\omega_x, \omega_y, \omega_z) = 2\pi \cdot (0.5, 5.56, 422)\mathrm{Hz}$. Afterwards the accordion lattice is compressed, resulting in the final trap with trapping frequencies $(\omega_x, \omega_y, \omega_z) = 2\pi \cdot (5.56, 5.56, 3898)\mathrm{Hz}$. We have written a code, allowing us to calculate the potential created using the optical setup, for different parameters (see Appendix A.3), considering all of the aforementioned losses.

The trap depth of the blue detuned potential is strongly dependent on the size of the area removed by the DMD (i.e. the trap size). This is shown in Figure 5.7. To estimate the required size of the trap, we calculate the Thomas Fermi radius of the BEC in the crossed beam optical dipole trap after evaporation. The trap frequencies
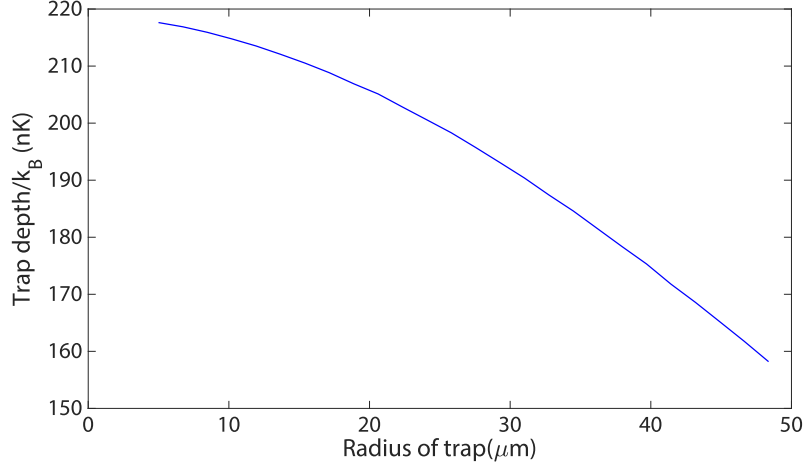
Figure 5.7.: Calculated trap depth in dependence of the radius of the circular area removed by the DMD.

in this trap are equal to $(\omega_x, \omega_y, \omega_z) = 2\pi \cdot (50, 30, 144)$Hz [24]. The Thomas-Fermi radius r_{TF}^i in direction $i = x, y, z$ is given by [70]

$$r_{TF}^i = \frac{2\mu}{m\omega_i} \quad \text{with} \quad \mu = \frac{\hbar\tilde{\omega}}{2}\left(\frac{15Na_s}{l_i}\right)^{\frac{2}{5}}, \tag{5.5}$$

where μ is the chemical potential, l_i gives the harmonic oscillator length (see Eq. (4.2)) and $\tilde{\omega} = \sqrt[3]{\omega_x\omega_y\omega_z}$. For this estimate we do not take the dipole-dipole interaction into account. In the crossed beam optical dipole trap the condensate has a Thomas-Fermi radius of $(r_{TF}^x, r_{TF}^y, r_{TF}^z) \approx (12, 7, 2.5)$µm. Consequently we plan to use a trap radius of 15 µm.

A trap with a radius of 15 µm on the atomic plane has a trap depth $U_{\text{trap}} = k_B 210$ nK. A gas with a temperature T

$$T = \frac{U_{\text{trap}}}{k_B\eta} \quad \text{with} \quad \eta \approx 8 \tag{5.6}$$

can be trapped in a trap with a trap depth U_{trap} [71]. Consequently a gas with a temperature of up to ≈ 26.25 nK can be trapped in the blue detuned potential. The critical temperature T_C in an harmonic potential is given by

$$T_C = 0.94\frac{\hbar\tilde{\omega}}{k_B}\sqrt[3]{N} \tag{5.7}$$

where N is the number of particles. Thus, the critical temperature in the accordion lattice at maximum lattice spacing ($(\omega_x, \omega_y, \omega_z) = 2\pi \cdot (0.5, 5.56, 422)$Hz)) at a typical value of $N \approx 10^5$, is equal to $T_C \approx 23$ nK. Thus, a gas with a temperature below the critical temperature, can be trapped in the blue detuned potential. For a gas with a temperature larger than the critical temperature, the gas will evaporatively cool,

resulting in a decrease in temperature, as well as in atom number. Consequently, one should aim for an adiabatic transition between the crossed beam optical dipole trap and the blue detuned potential, such that the phase space density is not altered significantly and the atoms are still condensed after the transfer.

The DMD can also be used to introduce rotation into the system. The concept is similar to that shown in Fig. 5.6, but instead of a fixed potential, we use the DMD to create a variable potential. The DMD can be used for both the rotating bucket and the optical spoon approach (see Section 3.5). For the rotating bucket approach the pattern displayed on the DMD has to be slightly elliptical. The BEC is trapped in this elliptical potential and vortices are created by rotating the ellipse around its centre.

An alternative approach is to use optical spoons (or stirring potentials), i.e. small repulsive barriers moving through the BEC. The size of the optical spoon is limited by the resolution limit of the optical setup, leading to a minimal radius of 1.457 µm, predicted by our simulations. Here the proposed sequence would be to trap the BEC in a circular trap. Subsequently, small repulsive potentials are swept through the BEC, creating rotational excitations. Experimentally, this can be achieved by switching a few mirrors within the circular trap to the ON state and moving the regions of high intensity through the trap. Grey scaling allows us to vary the depth of the stirring potentials.

6. Conclusion and Outlook

The goal of my master thesis was to built an experimental setup for the creation of vortices in a dipolar Bose-Einstein condensate. It consists of an optical accordion setup to create the appropriate trapping geometry as well as a variable blue detuned potential used to create the vortex excitations in the BEC. Both setups were designed to be used for both Erbium and Dysprosium, the two atomic species used in the RARE experiment at the Institute of Quantum Optics and Quantum Information (IQOQI) in Innsbruck.

The optical accordion lattice is based on the interference of two Gaussian beams under a shallow angle. The trap frequencies can be altered by changing the angle of interference. After a literature study of vortices in a BEC, we programmed a numerical simulation of the interference of two Gaussian beams. This simulation was used to determine the parameters for the optical accordion such that the trapping potential is appropriate for the creation of vortices.

We built an optical setup according to the determined specifications. The optical setup divides the incoming laser beam into two parallel beams, whose separation is governed by the height of the incoming beam. We control the height of the incoming beam using two parallel mirrors mounted on a rotation stage. Finally, the two parallel beams interfere in the focal point of an aspherical lens, creating the desired interference pattern. We characterized the temporal and dynamic stability of this system as well as the change in lattice spacing when altering the separation of the beams. Furthermore we have implemented a Piezo Stack in the optical setup which allows us to alter the phase difference of the beams. This enables us to control the phase of the resulting lattice.

We designed the optical setup used to create a variable blue detuned potential using a DMD and simulate the resulting potential. The optical setup consists of two telescopes to project the image displayed on the DMD onto the atomic plane. The first telescope is formed by two standard lenses, while the second one consists of a lens and the existing vertical imaging objective. This combination allows us to have a high demagnification without using a lens with large focal length. We optimized this optical setup using Zemax OpticStudion and discuss a strategy to align it. As the image of a single mirror on the atomic plane is smaller than the theoretical resolution of the system, more than one mirror contributes to the image in a single point. This allows grey scaling of the potential by turning on or off mirrors contributing to the potential in one point. This setup can be used for both the rotating bucket and the optical spoon scheme to create vortices as well as to provide in-plane confinement. The next step is to built and characterize the experimental setup.

The setup presented in this thesis can be used to study both single and multiple

vortices in a dBEC, opening the door to experimentally unexplored physics. We can study the change in the density profile of the vortex for different trap geometries as well as the emergence of density ripples near the roton instability. Moreover the modulation of the interaction of two vortices by the DDI can be studied. If the axial confinement is decreased we can, given that the horizontal imaging system is good enough, also study the effect of the DDI on the deformation of the vortex line. Increasing the radial confinement would give us the possibility to study the influence of the DDI on the precision of a vortex in an inhomogeneous trap. Moreover, by removing the cylindrical lens in the accordion lattice setup, we can increase the axial confinement such that the motion of the BEC in this direction is frozen out leading to a quasi-2D dBEC.

A. Matlab code

A.1. Numerical simulation of the accordion lattice

```matlab
clear all
close all

% Elementary constant
c = 299792458;              %Speed of light
h = 6.626070040e-34;        %Planck constant
hbar = h/2/pi;              %reduced Planck constant
u0 = 4*pi*1e-7;             %Vacuum permeability
e0 = 1/u0/(c^2);            %Vacuum permittivity
qe = 1.6021766208e-19;      %Elementary charge
G = 6.67408e-11;            %Gravitational constant
kB = 1.38064852e-23;        %Boltzmann constant
me = 9.10938356e-31;        %Electron mass
mp = 1.672621898e-27;       %Proton mass
uB = qe*hbar/2/me;          %Bohr magneton
uN = qe*hbar/2/mp;          %Nuclear magneton
alpha = u0*qe^2*c/(2*h);    %Finestructure constant
u = 1.660539040e-27;        %Atomic mass unit
a0 = 4*pi*e0*hbar^2/me/qe^2; %Bohr Radii
Ry = 13.605693009;          %Rydberg energy in eV
alpha = 1/137;              %Finestructure constant
mEr = 166*u;                %Mass Erbium


%Polarizability
Cfaktor1064 = (186/1.06)*c*u0*1.65e-41/2; %5e-   37
Cfaktor532 = 350*c*u0*1.65e-41/2; %350 for Dy, 317 for Er
Cfaktor1570 = 150*c*u0*1.65e-41/2;
Cfaktor370 = -1200*c*u0*1.65e-41/2;
Cfaktor373 = -1558*c*u0*1.65e-41/2;

% System parameters
f = 20; %Focal length (cm)
d = 2; % Beam seperation (cm)
```

```
35
36  %Definition Coordinate System
37  x = [-150:0.2:150]*1e-6;
38  y = [-1:0.5:1]*1e-6;
39  z = [-150:0.2:150]*1e-6;
40  [X,Y,Z] = ndgrid(x,y,z);
41
42  %Definition of Beams
43  lambda = 532e-9; %Wavelength (m)
44  k = 2*pi/lambda;    %Wavenumber k (1/m)
45  Cfaktor = Cfaktor532; %Polarizability
46  P0 = 5; %Laser Power (W)
47
48
49  w1a = 90e-6; %Waist x Beam 1 (m)
50  w1b = 90e-6; %Waist y Beam 1 (m)
51  w2a = w1a; %Waist x Beam 2 (m)
52  w2b = w1b;  %Waist y Beam 2 (m)
53
54  theta = atan(d/f);  %Half-angle between beams 1 & 2
55  E10 = sqrt(2*P0/(pi*w1a*w1b*c*e0)); %electric field
        amplitude of beam 1 at origin at time 0
56  E20 = E10; %electric field amplitude of beam 2 at origin
        at time 0
57
58  %Rotation of Beam 1 around y axis in an angle of theta
59  Xn = X.*cos(theta)+Z.*sin(theta);
60  Yn = Y;
61  Zn = -X.*sin(theta)+Z.*cos(theta);
62
63  %Electric field of Beam 1
64  w10 = sqrt(w1a*w1b); %minimum of waist radius (m)
65  z1 = pi*w10^2/lambda; %Rayleigh length (m)
66  z1a = pi*w1a^2/lambda; %Rayleigh length in x-direction (m
        )
67  z1b = pi*w1b^2/lambda; %Rayleigh length in y-direction (m
        )
68  w1z = w10*sqrt(1+(Xn/z1).^2); %Beam waist for all z
        values
69  w1az = w1a*sqrt(1+(Xn/z1a).^2); %Beam waist in x-
        direction for all z values
70  w1bz = w1b*sqrt(1+(Xn/z1b).^2); %Beam waist in y-
        direction for all z values
71  R1 = Xn.*(1+(z1./Xn).^2); %Radius of curvature of the
```

```matlab
        beam's wavefronts
72  R1a = Xn.*(1+(z1a./Xn).^2); %Radius of curvature of the
        beam's wavefronts in x-direction
73  R1b = Xn.*(1+(z1b./Xn).^2); %Radius of curvature of the
        beam's wavefronts in y-direction
74  R1(isnan(R1)) = inf; %Sets R1 to infinity in case of Xn=0
75  R1a(isnan(R1a)) = inf;
76  R1b(isnan(R1b)) = inf;
77  xsi = atan(Xn./z1); %Gouy-Phase
78
79
80  E1 = E10*w10./w1z.*exp(-(Zn.^2./(w1az.^2)+Yn.^2./(w1bz
        .^2))).*exp(-1i*k*(Zn.^2./(2*R1a)+Yn.^2./(2*R1b))).*
        exp(-1i*(k*Xn-xsi)); %E-field beam 1
81
82  %Rotation of Beam 2 around y axis in an angle of -theta
83  theta = -theta;
84  Xn = X.*cos(theta)+Z.*sin(theta);
85  Yn = Y;
86  Zn = -X.*sin(theta)+Z.*cos(theta);
87
88  %Electric field of Beam 2
89  w20 = sqrt(w2a*w2b); %minimum of waist radius (m)
90  z2 = pi*w20^2/lambda; %Rayleigh length (m)
91  z2a = pi*w2a^2/lambda; %Rayleigh length in x-direction (m
        )
92  z2b = pi*w2b^2/lambda; %Rayleigh length in y-direction (m
        )
93  w2z = w20*sqrt(1+(Xn/z2).^2); %Beam waist for all z
        values
94  w2az = w2a*sqrt(1+(Xn/z2a).^2); %Beam waist in x-
        direction for all z values
95  w2bz = w2b*sqrt(1+(Xn/z2b).^2); %Beam waist in y-
        direction for all z values
96  R2 = Xn.*(1+(z2./Xn).^2);  %Radius of curvature of the
        beam's wavefronts
97  R2a = Xn.*(1+(z2a./Xn).^2);  %Radius of curvature of the
        beam's wavefronts in x-direction
98  R2b = Xn.*(1+(z2b./Xn).^2);  %Radius of curvature of the
        beam's wavefronts in y-direction
99  R2(isnan(R2)) = inf;    %Sets R1 to infinity in case of
        Xn=0
100 R2a(isnan(R2a)) = inf;
101 R2b(isnan(R2b)) = inf;
```

```matlab
102 xsi = atan(Xn./z2); %Gouy-Phase
103
104
105 E2 = E20*w20./w2z.*exp(-(Zn.^2./(w2az.^2)+Yn.^2./(w2bz
      .^2))).*exp(-1i*k*(Zn.^2./(2*R2a)+Yn.^2)./(2*R2b)).*
      exp(-1i*(k*Xn-xsi)); %E-field beam 2
106
107 %Intensity of the two beams
108 I =(c*e0*abs(E1+E2).^2)/2; %Combined intensity of the two
       intersecting Gaussian beams
109
110 Ix = Cfaktor*squeeze(I(:,floor(size(I,2)/2)+1,floor(size(
      I,3)/2)+1)); %Intensity in x direction
111 Iy = Cfaktor*squeeze(I(floor(size(I,1)/2)+1,:,floor(size(
      I,3)/2)+1)); %Intensity in y direction
112 Iz = Cfaktor*squeeze(I(floor(size(I,1)/2)+1,floor(size(I
      ,2)/2)+1,:)); %Intensity in z direction
113
114 Idx = diff(Ix)/mean(diff(x)); %Numerical first derivative
       of the intensity in x direction
115 kx=diff(Idx)/mean(diff(x));   %Numerical second
      derivative of the intensity in x direction
116 wx = sqrt(-kx(z==0)/mEr)/(2*pi); %Trap frequency in x-
      direction
117
118 Idy = diff(Iy)/mean(diff(y)); %Numerical first derivative
       of the intensity in y direction
119 ky=diff(Idy)/mean(diff(y));   %Numerical second
      derivative of the intensity in y direction
120 wy = sqrt(-ky(y==0)/mEr)/(2*pi); %Trap frequency in y-
      direction
121
122 Idz = diff(Iz)/mean(diff(z)); %Numerical first derivative
       of the intensity in z direction
123 kz=diff(Idz)/mean(diff(z));   %Numerical second
      derivative of the intensity in z direction
124 wz = sqrt(-kz(x==0)/mEr)/(2*pi); %Trap frequency in z-
      direction
```

A.2. Calculation of beam displacement by two rotating parallel mirrors

```
1  clear all
2  close all
3  iter1=1;
4
5  d = 3.5; %distance of mirrors M1 and M2
6  l1 = 2.54; %length of mirror 1
7  l2 = 3.5;  %length of mirror 2
8  p1=[-10;-2.5]; %starting point of vector describing the
      beam
9  p2=[10;-2.5];  %end point of vector describing the beam
10
11 % Define start- and end-points of M1 and M2:
12 S1a = [-l1/2-1.25; -d/2]; %startpoint M1
13 S1e = [l1/2-1.25; -d/2];  %endpoint M1
14 S2a = [-l2/2+1.25; d/2];  %startpoint M2
15 S2e = [l2/2+1.25; d/2];   %endpoint M2
16
17 for theta = [40 60];
18
19 rot = [cosd(theta) -sind(theta); sind(theta) cosd(theta)
      ]; %define rotation matrix
20
21 %rotating Mirrors around origin by theta
22 S1ar = rot*S1a;
23 S2ar = rot*S2a;
24 S1er = rot*S1e;
25 S2er = rot*S2e;
26
27 %Define vectors describing the mirrors
28 t1l = linspace(-0.5,0.5,1000);
29 b1 = 0.5*(S1ar+S1er);
30 a1 = (S1ar-S1er);
31 S1=@(t1l) b1 + t1l.* a1;
32 Mirror1 =S1(t1l);
33
34
35 t2l = linspace(-0.5,0.5,1000);
36 b2 = 0.5*(S2ar+S2er);
37 a2 = (S2ar-S2er);
38 S2=@(t1l) b2 + t2l.* a2;
```

```matlab
39  Mirror2 =S2(t21);
40
41
42  % Define vector describing the beam:
43  xL=linspace(-20,20,1000);
44  bL= 0.5*(p1+p2);
45  aL = (p1-p2);
46  g=@(xL) bL + xL.*aL;
47
48
49  % Angle between laser beam and mirror 1 (=angle between x
       -axis and Mirror 1)
50  CosTheta1 = dot((p2-p1),(S1er-S1ar))/(norm((p2-p1))*norm
       ((S1er-S1ar)));
51  theta1 = acosd(CosTheta1);
52
53  % Angle between laser beam and mirror 2 (=angle between x
       -axis and Mirror 2)
54
55  CosTheta2 = dot((p2-p1),(S2er-S2ar))/(norm((p2-p1))*norm
       ((S2er-S2ar)));
56  theta2 = acosd(CosTheta2);
57
58  xL1=linspace(0,20,1000);
59
60  % Find intersection point of mirror 1 and beam
61  [xp,yp]=findintersection([S1ar(1),S1ar(2);S1er(1),S1er(2)
       ],[p1(1),p1(2); p2(1),p2(2)]);
62
63  % Check if the beam hits mirror 1
64     if    S1ar(1) < xp && xp < S1er(1) && S1ar(2) < yp &&
          yp < S1er(2)
65         disp('Laser beam hits mirror 1');
66     else
67         disp('Laser beam misses mirror 1');
68     end
69  % Find intersection point of mirror 2 and beam reflected
       by mirror 1
70  [xp1,yp1]=findintersection([S2ar(1),S2ar(2);S2er(1),S2er
       (2)],[xp,yp; xp+cosd(theta1+theta1),yp+sind(theta1+
       theta1)]);
71
72  % Check if the beam hits mirror 2
73     if  S2ar(1) < xp1 && xp1 < S2er(1) && S2ar(2) < yp1
```

```matlab
            && yp1 < S2er(2)
74              disp('Laser beam hits mirror 2');
75          else
76              disp('Laser beam misses mirror 2');
77          end
78  % Save height of beam and theta to A
79  A(iter1,:) = [theta, yp1];
80  iter1 = iter1+1;
81  end
82
83  % Calculate distance between the beams for the two angles
       .
84  distance = A(1,2)-A(2,2);
```

A.3. Calculation of trapdepth created by DMD

```
1  close all
2  clear all
3
4  % Constants
5  c = 299792458; % Lichtgeschwindigkeit
6  u = 1.660538921e-27;    % Atomic mass unit
7  m = 166*u;
8  uB = 9.27400915e-24; % Bohr Magneton
9  hbar = 1.05457e-34;
10 kb = 1.3806503e-23; % kBoltzmann
11 g = 9.80553; % gravitation
12 a0 = 0.5291772083e-10;% Bohr's radius in [m]
13 mu0 = 4*pi*1e-7;        % magnetic constant
14 Cfaktor370= 1200*c*mu0*1.65e-41/2; %polarizability of Er
       at 370nm
15 Cfaktor401 = 1696*c*mu0*1.65e-41/2; %polarizability of DY
       at 401nm
16
17 % Variables
18 P = 30e-3;              % Input power in W
19 magnificationfactor = 0.0347;
20 wmm = 3.6;              % Waist of gaussian beam on DMD
       in mm
21 innerradiusdmd = 1.5;   % Radius of circle cut with DMD
       in mm
22 Cfaktor = Cfaktor370;   % Polarizability
23
24
25 % DMD specifications
26 height = 1080;          % Height of the micromirror array
       in pixel
27 width = 1920;           % Length of the micromirror array
       in pixel
28 lengthpixel = 20.736/width;
29
30 % Beam on DMD
31 Z = zeros(width,height);
32 [X,Y] = meshgrid(1:width,1:height);
33 w = wmm/lengthpixel;                      % Waist of
       Gaussian beam in pixels
34 Imax = 2*P/(pi*wmm^2)*10^2;               % Maximum
```

```matlab
       intensity of the Gaussian beam in W/cm^2
35 R = sqrt((X-width/2).^2+(Y-height/2).^2);    % Radius in
      pixel
36 Z = Imax.*exp(-(2*R.^2./(w.^2)));            % Spatial
      intensity distribution of gaussian beam
37
38
39 % Beam on atoms
40 R1 = sqrt((X-width/2).^2+(Y-height/2).^2)*
      magnificationfactor*lengthpixel;  % Radius of the
      circle cut out by the DMD in px reduced by
      magnificationfactor
41 w1 = wmm*magnificationfactor;
                                               % Waist
      of gaussian beam in mm reduced by magnificationfactor
42 Iatom_max= 2*P*0.82*0.7/(pi*w1^2);
                                            % Maximum
      intensity of Beam considering losses due to viewport
      and DMD (W/mm^2)
43 Trapdepth = Cfaktor*2*Iatom_max*1e15/kb;
                                         % Trapdepth
      corresponding to the maximum intensity in nK
44 innerradius= innerradiusdmd*magnificationfactor;
                                   % Radius of the circle cut
      out by the DMD on the atoms
45
46 Zmean = Trapdepth.*exp(-(2*R1.^2./(w1.^2)));
                                       % Potential on the
      atoms due to Gaussian beam
47 Zmean(R1<innerradius) = 0;
                                                         %
      Setting the intensity of the area cut out by the DMD
      to zero
48
49 % Smoothing the potential
50 [xf,yf] = ndgrid([-150:150],[-150:150]);
51 radblur = 1e-6/((lengthpixel*magnificationfactor)*1e-3);
52 filtmat = exp(-(xf/radblur).^2-(yf/radblur).^2);
53 filtmat = filtmat/(sum(sum(filtmat)));
54 Zmean2 = filter2(filtmat,Zmean,'same');
55
56 figure(2)
57 ellipse = surf(X*lengthpixel*magnificationfactor*1000,Y*
      lengthpixel*magnificationfactor*1000,Zmean,'Edgecolor'
```

```matlab
        ,'none');

hcb = colorbar;
hcb.Label.String = 'Potential/kB (nK)';
set(hcb,'fontsize',12)
xlim([min(min(X*lengthpixel*magnificationfactor*1000))
    max(max(X*lengthpixel*magnificationfactor*1000))]);
ylim([min(min(Y*lengthpixel*magnificationfactor*1000))
    max(max(Y*lengthpixel*magnificationfactor*1000))]);
xlabl = xlabel('x(\mum)');
ylabl = ylabel('y(\mum)');
zlabl = zlabel('Potential/k_B (nK)');
ylabl.FontName = 'Myriad Pro';
xlabl.FontName = 'Myriad Pro';
zlabl.FontName = 'Myriad Pro';
set(xlabl,'fontsize',30)
set(ylabl,'fontsize',30)
set(zlabl,'fontsize',30)
ax = gca;
ax.FontName = 'Myriad Pro';
set(ax,'fontsize',26)

figure(3)

cut = Zmean2(height/2,:);
k = plot(X*lengthpixel*magnificationfactor*1000,cut , 'b
    -', 'LineWidth', 3 );

xlabl = xlabel('x(\mum)');
ylabl = ylabel('Potential/k_B (nK)');
ax = gca;
set(ax,'fontsize',26)
set(xlabl,'fontsize',30)
set(ylabl,'fontsize',30)
xlim = ([0 90]);


disp(['Input power: ', num2str(P*1000),' mW']);
disp(['Maximum intensity on DMD: ' num2str(Imax*1000), '
    mW/cm^2']);
disp(['Beam Waist on Atoms: ', num2str(w1*1000), ' um']);
disp(['Radius of circle cut by DMD: ', num2str(
    innerradius*1000), ' um']);
disp(['Trapdepth: ',num2str(max(max(Zmean2))),' nK']);
```

Bibliography

[1] Satyendra Bose. Plancks Gesetz und Lichtquantenhypothese. *Zeitschrift für Physik*, 26(1):178–181, 1924.

[2] M. H. Anderson, J. R. Ensher, M. R. Matthews, C. E. Wieman, and E. A. Cornell. Observation of Bose-Einstein Condensation in a Dilute Atomic Vapor. *Science*, 269(5221):198–201, 1995.

[3] K. B. Davis, M. O. Mewes, M. R. Andrews, N. J. van Druten, D. S. Durfee, D. M. Kurn, and W. Ketterle. Bose-Einstein Condensation in a Gas of Sodium Atoms. *Phys. Rev. Lett.*, 75:3969–3973, 1995.

[4] S. Jochim. *Bose-Einstein Condensation of Molecules*. PhD thesis, University of Innsbruck, 2004.

[5] J. Klaers, J. Schmitt, F. Vewinger, and M. Weitz. Bose–Einstein condensation of photons in an optical microcavity. *Nature*, 468, 2010.

[6] C. C. Bradley, C. A. Sackett, J. J. Tollett, and R. G. Hulet. Evidence of Bose-Einstein Condensation in an Atomic Gas with Attractive Interactions. *Phys. Rev. Lett.*, 75:1687–1690, 1995.

[7] G. Modugno, G. Ferrari, G. Roati, R. J. Brecha, A. Simoni, and M. Inguscio. Bose-Einstein Condensation of Potassium Atoms by Sympathetic Cooling. *Science*, 294(5545):1320–1322, 2001.

[8] T. Weber, J. Herbig, M. Mark, H.-C. Nägerl, and R. Grimm. Bose-Einstein Condensation of Cesium. *Science*, 299(5604):232–235, 2003.

[9] S. Kraft, F. Vogt, O. Appel, F. Riehle, and U. Sterr. Bose-Einstein Condensation of Alkaline Earth Atoms: ^{40}Ca. *Phys. Rev. Lett.*, 103:130401, 2009.

[10] S. Stellmer, M. K. Tey, B. Huang, R. Grimm, and F. Schreck. Bose-Einstein Condensation of Strontium. *Phys. Rev. Lett.*, 103:200401, 2009.

[11] M. Lu, N. Q. Burdick, S. H. Youn, and B. L. Lev. Strongly Dipolar Bose-Einstein Condensate of Dysprosium. *Phys. Rev. Lett.*, 107:190401, 2011.

[12] K. Aikawa, A. Frisch, M. Mark, S. Baier, A. Rietzler, R. Grimm, and F. Ferlaino. Bose-Einstein Condensation of Erbium. *Phys. Rev. Lett.*, 108:210401, 2012.

[13] Y. Takasu, K. Maki, K. Komori, T. Takano, K. Honda, M. Kumakura, T. Yabuzaki, and Y. Takahashi. Spin-Singlet Bose-Einstein Condensation of Two-Electron Atoms. *Phys. Rev. Lett.*, 91:040404, 2003.

[14] A. Griesmaier, J. Werner, S. Hensler, J. Stuhler, and T. Pfau. Bose-Einstein Condensation of Chromium. *Phys. Rev. Lett.*, 94:160401, 2005.

[15] A. Robert, O. Sirjean, A. Browaeys, J. Poupard, S. Nowak, D. Boiron, C. I. Westbrook, and A. Aspect. A Bose-Einstein Condensate of Metastable Atoms. *Science*, 292(5516):461–464, 2001.

[16] D. G. Fried, T. C. Killian, L. Willmann, D. Landhuis, S. C. Moss, D. Kleppner, and T. J. Greytak. Bose-Einstein Condensation of Atomic Hydrogen. *Phys. Rev. Lett.*, 81:3811–3814, 1998.

[17] K.-K. Ni, S. Ospelkaus, M. H. G. de Miranda, A. Pe'er, B. Neyenhuis, J. J. Zirbel, S. Kotochigova, P. S. Julienne, D. S. Jin, and J. Ye. A High Phase-Space-Density Gas of Polar Molecules. *Science*, 322(5899):231–235, 2008.

[18] W. R. Anderson, J. R. Veale, and T. F. Gallagher. Resonant Dipole-Dipole Energy Transfer in a Nearly Frozen Rydberg Gas. *Phys. Rev. Lett.*, 80:249–252, 1998.

[19] Pyotr Kapitsa. Viscosity of Liquid Helium below the λ-Point. *Nature*, 1938.

[20] John F Allen. Flow of Liquid Helium II . *Nature*, 1938.

[21] M. R. Matthews, B. P. Anderson, P. C. Haljan, D. S. Hall, C. E. Wieman, and E. A. Cornell. Vortices in a Bose-Einstein Condensate. *Phys. Rev. Lett.*, 83:2498–2501, 1999.

[22] M. W. Zwierlein, J. R. Abo-Shaeer, A. Schirotzek, C. H. Schunck, and W. Ketterle. Vortices and superfluidity in a strongly interacting Fermi gas. *Nature*, 435:1047 – 1051, 2005.

[23] Z. Hadzibabic, P. Krüger, M. Cheneau, B. Battelier, and Dalibard J. Berezinskii–kosterlitz–thouless crossover in a trapped atomic gas. *Nature*, 441:1118–1121, 2006.

[24] A. Trautmann, P. Ilzhöfer, G. Durastante, C. Politi, M. Sohmen, M. J. Mark, and F. Ferlaino. Dipolar Quantum Mixtures of Erbium and Dysprosium Atoms. *Phys. Rev. Lett.*, 121:213601, 2018.

[25] C. Chin, R. Grimm, P. Julienne, and E. Tiesinga. Feshbach resonances in ultracold gases. *Rev. Mod. Phys.*, 82:1225–1286, 2010.

[26] B. R. Judd and I. Lindgren. Theory of zeeman effect in the ground multiplets of rare-earth atoms. *Phys. Rev.*, 122:1802–1812, 1961.

[27] J. G. Conway and B. G. Wybourne. Low-lying energy levels of lanthanide atoms and intermediate coupling. *Phys. Rev.*, 130:2325–2332, 1963.

[28] Albert Frisch. *Dipolar Quantum Gases of Erbium.* PhD thesis, University of Innsbruck, 2014.

[29] T. Lahaye, C. Menotti, L. Santos, M. Lewenstein, and T. Pfau. The physics of dipolar bosonic quantum gases. *Rep. Prog. Phys.*, 72(12):126401, 2009.

[30] E. P. Gross. Structure of a quantized vortex in boson systems. *Il Nuovo Cimento (1955-1965)*, 20(3):454–477, 1961.

[31] L. P. Pitaevskii. Vortex lines in an imperfect Bose gas. *Soviet Physics Jetp*, 1961.

[32] T. Langen and M. J. Mark. Ultrakalt magnetisiert. *Physik Journal*, 2018.

[33] R. Grimm, M. Weidemüller, and Y. B. Ovchinnikov. Optical Dipole traps for Neutral Atoms. *Adv. At., Mol., Opt. Phys.*, 42:95–170, 1999.

[34] H. Li, J.-F. Wyart, O. Dulieu, and M. Lepers. Anisotropic optical trapping as a manifestation of the complex electronic structure of ultracold lanthanide atoms: The example of holmium. *Phys. Rev. A*, 95:062508, 2017.

[35] J. H. Becher, S. Baier, K. Aikawa, M. Lepers, J.-F. Wyart, O. Dulieu, and F. Ferlaino. Anisotropic polarizability of Erbium atoms. *Phys. Rev. A*, 97:012509, 2018.

[36] M. Lepers, J.-F. Wyart, and O. Dulieu. Anisotropic optical trapping of ultracold erbium atoms. *Phys. Rev. A*, 89:022505, 2014.

[37] H. Li, J.-F. Wyart, O. Dulieu, and M. Lepers. Optical trapping of ultracold dysprosium atoms: transition probabilities, dynamic dipole polarizabilities and van der Waals C 6 coefficients. *J. Phys. B: At. Mol. Opt. Phys*, 50:014005, 2017.

[38] L. Landau. Theory of the Superfluidity of Helium II. *Phys. Rev.*, 60:356–358, 1941.

[39] Pitaevskii L. and Stringari S. *Bose Einstein Condensation and Superfluidity.* Oxford University Press, 2016.

[40] N. Bogolubov. On the theory of Superfluidity. *Journal of Physics*, 1947.

[41] D. G. Henshaw and A. D. B. Woods. Modes of atomic motions in liquid helium by inelastic scattering of neutrons. *Phys. Rev.*, 121:1266–1274, Mar 1961.

[42] L. Chomaz, van Bijnen R. M. W., D. Petter, G. Faraoni, S. Baier, J. H. Becher, M. J. Mark, F. Wächtler, L. Santos, and F. Ferlaino. Observation of roton mode population in a dipolar quantum gas. *Nature Physics*, 14:442–446, 2018.

[43] Ryan M. Wilson, Shai Ronen, and John L. Bohn. Critical superfluid velocity in a trapped dipolar gas. *Phys. Rev. Lett.*, 104:094501, Mar 2010.

[44] N. Verhelst and J. Tempère. Vortex Structures in Ultra-Cold Atomic Gases. 2017.

[45] E. Lundh, C. J. Pethick, and H. Smith. Zero-temperature properties of a trapped Bose-condensed gas: Beyond the Thomas-Fermi approximation. *Phys. Rev. A*, 55:2126–2131, 1997.

[46] D. H. J. O'Dell and C. Eberlein. Vortex in a trapped Bose-Einstein condensate with dipole-dipole interactions. *Phys. Rev. A*, 75:013604, 2007.

[47] Yoshihisa Yamamoto. *Bose-Einstein Condensation and Matter-Wave Lasers.* Japan Science and Technology Agency, 2018.

[48] Martin A., Marchant N.G., O'Dell D. H.J., and Parker N. G. Vortices and Vortex lattices in quantum ferrofluids. *J. Phys.: Condens. Matter*, 2017.

[49] B. C. Mulkerin, D. H. J. O'Dell, A. M. Martin, and N. G. Parker. Vortices in the two-dimensional dipolar Bose gas. *J. Phys. Conf. Ser.*, 497:012025, 2014.

[50] R. M. Wilson, S. Ronen, J. L. Bohn, and H. Pu. Manifestations of the Roton Mode in Dipolar Bose-Einstein Condensates. *Phys. Rev. Lett.*, 100:245302, 2008.

[51] L. Chomaz, D. Petter, P. Ilzhöfer, G. Natale, A. Trautmann, C. Politi, G. Durastante, R. M. W. van Bijnen, A. Patscheider, M. Sohmen, M. J. Mark, and F. Ferlaino. Long-lived and transient supersolid behaviors in dipolar quantum gases. *Phys. Rev. X*, 9:021012, Apr 2019.

[52] L. Tanzi, E. Lucioni, F. Famà, J. Catani, A. Fioretti, C. Gabbanini, R. N. Bisset, L. Santos, and G. Modugno. Observation of a dipolar quantum gas with metastable supersolid properties. *Phys. Rev. Lett.*, 122:130405, Apr 2019.

[53] F. Böttcher, J.-N. Schmidt, M. Wenzel, J. Hertkorn, M. Guo, T. Langen, and T. Pfau. Transient supersolid properties in an array of dipolar quantum droplets. *Phys. Rev. X*, 9:011051, Mar 2019.

[54] B. C. Mulkerin, R. M. W. van Bijnen, D. H. J. O'Dell, A. M. Martin, and N. G. Parker. Anisotropic and long-range vortex interactions in two-dimensional dipolar bose gases. *Phys. Rev. Lett.*, 111:170402, 2013.

[55] K. W. Madison, F. Chevy, W. Wohlleben, and J. Dalibard. Vortex Formation in a Stirred Bose-Einstein Condensate. *Phys. Rev. Lett.*, 84:806–809, 2000.

[56] G. Gauthier, M. T. Reeves, X. Yu, A. S. Bradley, M. A. Baker, T. A. Bell, H. Rubinsztein-Dunlop, M. J. Davis, and T. W. Neely. Giant vortex clusters in a two-dimensional quantum fluid. *Science*, 364(6447):1264–1267, 2019.

[57] S. J. Rooney, P. B. Blakie, B. P. Anderson, and A. S. Bradley. Suppression of Kelvon-induced decay of quantized vortices in oblate Bose-Einstein condensates. *Phys. Rev. A*, 84:023637, 2011.

[58] M. Klawunn, R. Nath, P. Pedri, and L. Santos. Transverse Instability of Straight Vortex Lines in Dipolar Bose-Einstein Condensates. *Phys. Rev. Lett.*, 100, 2008.

[59] B. P. Anderson, P. C. Haljan, C. E. Wieman, and E. A. Cornell. Vortex precession in bose-einstein condensates: Observations with filled and empty cores. *Phys. Rev. Lett.*, 85:2857–2860, Oct 2000.

[60] D. V. Freilich, D. M. Bianchi, A. M. Kaufman, T. K. Langin, and D. S. Hall. Real-Time Dynamics of Single Vortex Lines and Vortex Dipoles in a Bose-Einstein Condensate. *Science*, 329(5996):1182–1185, 2010.

[61] A. L. Fetter and A. A. Svidzinsky. Vortices in a trapped dilute bose-einstein condensate. *J.Phys.: Condens. Matter*, 2001.

[62] D. Rychtarik, B. Engeser, H.-C. Nägerl, and R. Grimm. Two-Dimensional Bose-Einstein Condensate in an Optical Surface Trap. *Phys. Rev. Lett.*, 92:173003, 2004.

[63] P. Cladé, C. Ryu, A. Ramanathan, K. Helmerson, and W. D. Phillips. Observation of a 2D Bose Gas: From Thermal to Quasicondensate to Superfluid. *Phys. Rev. Lett.*, 102:170401, 2009.

[64] T. C. Li and H. Kelkar and D. Medellin and M. G. Raizen. Real-time control of the periodicity of a standing wave: an optical accordion. *Opt. Express*, 16(8):5465–5470, 2008.

[65] J. L. Ville, T. Bienaimé, R. Saint-Jalm, L. Corman, M. Aidelsburger, L. Chomaz, K. Kleinlein, D. Perconte, S. Nascimbène, J. Dalibard, and J. Beugnon. Loading and compression of a single two-dimensional Bose gas in an optical accordion. *Phys. Rev. A*, 95:013632, 2017.

[66] C. Ravensbergen, V. Corre, E. Soave, M. Kreyer, S. Tzanova, E. Kirilov, and R. Grimm. Accurate Determination of the Dynamical Polarizability of Dysprosium. *Phys. Rev. Lett.*, 120:223001, 2018.

[67] X. Zhang, Y. Chen, J. Fang, T. Wang, J. Li, and L. Luo. Beam pointing stabilization of an acousto-optic modulator with thermal control. *Opt. Express*, 27(8):11503–11509, 2019.

[68] C. Palmer and Loewen E. *Diffraction Grating Handbook*. Newport Cooperation, 2005.

[69] G. Gauthier, I. Lenton, N. McKay Parry, M. Baker, M. J. Davis, H. Rubinsztein-Dunlop, and T. W. Neely. Direct imaging of a digital-micromirror device for configurable microscopic optical potentials. *Optica*, 3(10):1136–1143, 2016.

[70] Franco Dalfovo, Stefano Giorgini, Lev P. Pitaevskii, and Sandro Stringari. Theory of bose-einstein condensation in trapped gases. *Rev. Mod. Phys.*, 71:463–512, Apr 1999.

[71] O. J. Luiten, M. W. Reynolds, and J. T. M. Walraven. Kinetic theory of the evaporative cooling of a trapped gas. *Phys. Rev. A*, 53:381–389, Jan 1996.